SOLIDIFICATION AND HEAT TRANSFER IN THE CONTINUOUS CASTING OF STEEL

by

JAMES E. LAIT

A THESIS SUBMITTED IN PARTIAL FULFILMENT OF
THE REQUIREMENTS FOR THE DEGREE OF
MASTER OF APPLIED SCIENCE

in the Department
of
METALLURGY

We accept this thesis as conforming to the
standard required from candidates for the
degree of MASTER OF APPLIED SCIENCE

THE UNIVERSITY OF BRITISH COLUMBIA

March, 1973

In presenting this thesis in partial fulfilment of the requirements for an advanced degree at the University of British Columbia, I agree that the Library shall make it freely available for reference and study. I further agree that permission for extensive copying of this thesis for scholarly purposes may be granted by the Head of my Department or by his representatives. It is understood that copying or publication of this thesis for financial gain shall not be allowed without my written permission.

Department of Metallurgy

The University of British Columbia
Vancouver 8, Canada

Date April 30, 1973

ABSTRACT

Radioactive gold has been added to the liquid pool during the continuous casting of mild steel billets, blooms and beam blanks and of a stainless steel slab. The tests were conducted on low-head, curved mold and straight mold, vertical bend type casting machines. From autoradiographs of the sections of the steel, observations were made of the flow pattern in the liquid pool, of the uniformity and thickness of the solid shell in the mold and sub-mold regions and of the cast structure of the strand. Pool depths were estimated from the position of tungsten pellets containing radioactive cobalt, dropped into the pool with the gold.

One and two-dimensional finite difference heat transfer models were developed to calculate the pool profiles in strands being continuously cast. The predicted pool profiles and pool depths have been compared to profiles measured from autoradiographs and pool depths measured with tungsten pellets. The model-predicted surface temperatures of low carbon steel billets at the mold bottom have been compared to measured values reported in the literature. The pool and surface temperature profiles calculated with the finite difference model have been compared to profiles predicted by an integral profile model.

TABLE OF CONTENTS

	Page
ABSTRACT	ii
TABLE OF CONTENTS	iii
LIST OF FIGURES	vii
LIST OF TABLES	xi
LIST OF SYMBOLS	xii
ACKNOWLEDGEMENT	xv
1. INTRODUCTION	1
1.1. General Comments	1
1.2. Previous Work	4
1.2.1. Fluid Flow and Liquid Pool	4
1.2.2. Structure	8
1.2.3. Mathematical Models	10
1.2.4. Objectives of Present Work	14
2. MATHEMATICAL MODEL	15
2.1. Heat Flow Equations	15
2.2. Initial and Boundary Conditions	18
2.3. Method of Solution	24
3. METHOD	27
3.1. Continuous Casting Operations	27
3.1.1. General Description	27
3.1.2. Western Canada Steel	27
3.1.3. Manitoba Rolling Mills	30

page

3.1.4. Atlas Steel 30
3.1.5. Algoma Steel 31
3.1.6. U.S. Steel 32
3.2. Procedure 33

4. RESULTS 36
4.1. Liquid Mixing, Solid Shell and Cast Structure . . . 36
4.1.1. General Observations of the Test Results . . 36
4.1.2. Specific Observations; Manitoba Rolling Mills. 42
4.1.3. Atlas Steel 46
4.1.4. Algoma Steel 51
4.1.4.1. Beam Blanks 51
4.1.4.2. Blooms 58
4.1.5. U.S. Steel 65
4.2. Calculated and Measured Pool Profiles and Pool Depths. 68
4.2.1. General Comments 68
4.2.2. Calculated and Measured Pool Profiles in the mold 69
4.2.3. Calculated and Measured Pool Depths 69

5. DISCUSSION 79
5.1. Liquid Mixing, Solid Shell and Cast Structures . . . 79
5.1.1. Liquid Mixing 79
5.1.1.1. General Comments 79
5.1.1.2. Open Pour 79
5.1.1.3. Submerged Shroud 81
5.1.2. Solid Shell 83

Page

5.1.2.1. Near the Meniscus 83

5.1.2.2. Mold Region 85

5.1.2.3. Submold Region 86

5.1.3. Cast Structure 87

5.1.3.1. Stainless Steel 87

5.1.3.2. Effect of Tundish Teeming 89

5.1.3.3. Columnar Structure 90

5.1.3.4. Equiaxed Structure 91

5.1.3.5. Solute Rich Pipes in Equiaxed Zone . 93

5.1.3.6. Radial Cracking 94

5.1.3.7. Sulphide Inclusions 95

5.2. Calculated and Measured Pool Profiles and Pool Depths . 96

5.2.1. Validity of Assumptions in Mathematical Models. . 96

5.2.2. Calculated and Measured Pool Profiles in the mold 99

5.2.2.1. Low Carbon Steel 99

5.2.2.2. Stainless Steel Slab 102

5.2.3. Calculated and Measured Pool Depths 103

5.2.3.1. Calculated Pool Depths using One-Dimensional Model 103

5.2.3.2. Calculated Pool Depths using Two-Dimensional Model 104

5.2.3.3. Comparison of Calculated and Measured Pool Depths 105

5.2.4. Calculated and Measured Surface Temperatures . 106

SUMMARY 110

CONCLUSIONS 114

Page

SUGGESTED FUTURE WORK 116

APPENDIX 117

REFERENCES 123

PUBLICATIONS 126

LIST OF FIGURES

Figure		Page
1	Heat transfer zones in continuous casting	16
2	Dependence of enthalpy on temperature for the stainless steel slab	16
3	Average flux of heat extracted by the mold as a function of dwell time	22
4	Average, overall heat transfer coefficient for the mold as a function of dwell time.	22
5	Estimated spray heat transfer coefficient as a function of spray water flux per unit area	26
6	(a) Schematic of straight mold, vertical type casting machine with bending. (b) Schematic of low-head, curved mold casting machine .	28
7	Autoradiographs of longitudinal sections of test strands M1 to M4, cast at Manitoba Rolling Mills..	43
8	(a) Section 2C of Figure 7, showing thin regions of the shell and associated depressions in the outer billet surface. (b) Section 1A of Figure 7, showing solid shell segment above meniscus. (c) Section 2E of Figure 7, showing gold rich central region with periodic bridging across the centreline by large dendrites	44
9	Autoradiographs of transverse sections of strands at positions indicated below meniscus. (a) strand M2, (b) strand M4	45
10	Autoradiographs of longitudinal and transverse sections of stainless steel slab, Test At1. The positions of the transverse sections with respect to the meniscus are indicated	47
11	Section 2C of Figure 10, showing discontinuity in shell thickness. Top of autoradiograph 15.7 cm. below meniscus.	49
12	Distribution of radioactive gold in the stainless steel slab prior to sectioning	49
13	Composite of autoradiographs of beam blank A, Test A&1 showing the pool profile down the web (C) and perpendicular to the longitudinal axis (B and R).	50

Figure		Page
14	(a) Autoradiograph B6 of Figure 13. (b) Sulphur print of same surface as in (a)	52
15	(a) Autoradiograph of central portion of C1, Figure 13. (b) Sulphur print of same surface as in (a). Note that the circle is an artifact and is not significant. . . .	53
16	Composite of autoradiographs of beam blank E showing the pool profile down the web (E) and perpendicular to the longitudinal axis (F)..	55
17	Distribution of radioactive gold in E beam blank and Test Aℓ4 bloom.	53
18	Sulphur print of section F4, Figure 16 showing clumps of sulphide inclusions and centreline cracking	56
19	Autoradiograph (a) and sulphur print (b) of adjacent areas of E2, Figure 16 showing clumps of sulphide inclusions and solute enriched centreline cracks . . .	57
20	Composite of autoradiographs of bloom, Test Aℓ3, showing the pool profile down the strand (G) and perpendicular to the strand axis (H,K).	59
21	Shell corner and average shell thickness as a function of distance below meniscus.	57
22	(a) Autoradiograph G25 in Figure 20. (b) Sulphur print of same area as (a)	60
23	Composite of autoradiographs of bloom, Test Aℓ4, showing the pool profile down the strand (L) and perpendicular to the strand axis (M,N)	61
24	Autoradiograph (a) and sulphur print (b) of section N1, Figure 23 showing corner crack filled with gold and sulphur rich material at A.	63
25	Sulphur print of part of section L1, Figure 23 showing V segregate pattern.	64
26	Sulphur print of section M5, Figure 23 showing centreline intergranular cracks filled with sulphur rich residual liquid	63
27	Composite of autoradiographs of billet, Test U1, showing the pool profile down the Strand (A) and perpendicular to the strand axis (B)	66
28	Section B2 of Figure 27, showing shell separation at the corner	64

Figure		Page
29	Measured average dendrite spacing as a function of distance from the billet surface for Test U1	67
30	Section B5 of Figure 27, showing radial cracking in transverse section	67
31	Liquid pool and surface temperature profiles in the mold region for the stainless steel slab O, measured inside radius; ●, measured outside radius. A, calculated finite difference with equation (7). B, calculated finite difference with equation (6). C, calculated integral profile with equation (7). D, calculated integral profile with equation (6).	71
32	Liquid pool and surface temperature profile in the mold region for (a) Test M1, (b) Test M2, (c) Test M3, (d) Test M4. O measured, average shell thickness of inside and outside radius surface. Caption as for Figure 31 . .	72
33	Shell thickness for inside and outside radius faces from Test M3.	71
34	Liquid pool and surface temperature profiles in the mold region for (a) Test Aℓ1, (b) Test Aℓ2, (c) Test Aℓ3, (d) Test Aℓ4. Caption as for Figure 32	73
35	Liquid pool and surface temperature profiles in the mold region for Test U1. Caption as for Figure 32	74
36	Liquid pool and surface temperature profiles for the stainless steel slab. Caption as for Figure 32	75
37	Liquid pool and surface temperature profiles for (a) Tests M1, M2, (b) Tests M3, M4. Caption as for Figure 32 .	76
38	Position of horizontal slices in web area, 1, and in flange area, 2, of A and E beam blanks used in calculating pool profiles with the one-dimensional models. S, positions of input streams	74
39	Liquid pool and surface temperature profiles for (a) web (A) and flange (B) areas of A beam blank, Test A 1. Curves A and B calculated with finite difference using equation (7), curve C with integral profile using equation (7). (b) web (A) and flange (B) areas of E beam blank Test A 2. Caption as for Figure 39(a). (c) A, Test A 3. B, Test A 4. Curves calculated with finite difference model using equation (7). S, Temperature of blooms at straightener, 900°C.	77

Figure		Page
40	Liquid pool and surface temperature profiles for Test W2a and Test W2c.	78
41	(a) Schematic drawing of distorted shell without flange rollers. (b) Shell contour after deformation by flange rollers .	88
42	Temperature distribution in A beam blank web, Test A 1, 2.5 m. below meniscus. Estimated region of low ductility[14] is indicated as well as the observed region of radial cracking	88
43	Effects of method of latent heat evolution and use of k_{eff} on calculated shell thickness for the stainless steel slab. k_{eff} used for T > 1460°C, % latent heat released at solidus: 25, 50, 75%,—— ; 100%,— — ; k_{eff} used for T > 1399°C, 100% latent heat released at solidus —·—·—, Integral profile model,------- . . .	97
44	Effects of method of latent heat evolution and use of k_{eff} on calculated shell thickness for low carbon steel. k_{eff} used for T > 1525°C, 5-100% latent heat released at solidus,———; k_{eff} used for T > 1492°C, 100% latent heat released at solidus, —·——·—. Integral Profile model,-----.	97
45	Autoradiograph of transverse section near tungsten pellet position taken after tests on a 17.5 cm. billet at Laclede Steel.	107
46	Arrangement of nodes in horizontal slice for one-dimensional finite difference model.	118
47	Flow chart of computer program for finite difference model	118
48	Arrangement of nodes in horizontal section of billet for two-dimensional finite difference model	121

LIST OF TABLES

Table		Page
I	Thermophysical Properties of Steel	21
II	Parameter Used in Integral Profile and Finite Difference Calculations.	21
III	Characteristics of Heat Transfer Zones	25
IV	Casting Machine Details	29
V	Experiment, Casting Parameters and Pool Depths	34
VI	Steel Compositions.	37
VII	Casting Characteristics from Autoradiographs	41
VIII	Measurement of Dendrite Spacing	91
IX	Measured and Predicted Average Mold Heat Flux.	101
X	Predicted and Measured[6] Surface Temperatures (°C) . . .	109

LIST OF SYMBOLS

a,b	constants in equation (4)
C	specific heat, kcal $kg.^{-1}$ $°C^{-1}$
f	view factor for radiation
h	heat transfer coefficient, kcal $m.^{-2}$ $sec.^{-1}$ °C
h_o, h_M	mold heat transfer coefficients (between the casting surface and the mold water) at and below the meniscus respectively
$\bar{h}_M, \bar{h}_S$	average heat transfer coefficients for the mold and sprays respectively
H	enthalpy, kcal $kg.^{-1}$
H_i, H'_i	enthalpy of the i th node at time t and $t + \Delta t$ respectively
H_n, H'_n	enthalpy of the surface node at time t and $t + \Delta t$ respectively
$H_{i,j}, H'_{i,j}$	enthalpy of node (i,j) at time t and time $t + \Delta t$ respectively
$H_{n,j}, H_{i,n}$	enthalpy of surface nodes at $y = 0$ and at $z = 0$ respectively
k	thermal conductivity, kcal $m.^{-1}$ $sec.^{-1}$ $°C^{-1}$
k_{eff}	effective thermal conductivity for the liquid pool
L	latent heat, kcal $kg.^{-1}$
P	mold perimeter, m
q_{o_y}, q_{o_z}	heat flux from the surface of the casting in the y and z directions, kcal $m.^{-2}$ $sec.^{-1}$
$\bar{q}_o$	average surface heat flux
Q_o	measured rate of heat removal by the mold, kcal $sec.^{-1}$
t	time, sec.

t_M	dwell time, sec.
T	temperature, °C
T_M, T_o	pouring temperature and temperature at the surface of the casting respectively
T_S	solidus temperature
T_{WM}, T_{WS}	temperature of the mold water, sprays water and surroundings respectively
u	casting speed, m. $sec.^{-1}$
w	width of casting, m.
x	withdrawal direction, m.
X	effective mold length, m.
y	direction perpendicular to casting face
y_t	thickness of solid shell, cm.
z	direction perpendicular to x and y
γ_S	fraction of metal solidified
η	constant determining rate of decrease of h_M with x, $m.^{-1}$
ρ	density, kg. $m.^{-3}$
σ	Stephan-Boltzman constant, 1.356 (10^{-11}) kcal $m.^{-2}$ $sec.^{-1}$ $(°k)^{-4}$

Dimensionless Groups

Q^*	heat removal per unit length of mold perimeter $\left(= \frac{Q_o/_P}{\sqrt{u\rho Ck}\ T_S}\right)$

X^* effective mold length

$$(= \frac{X \bar{h}_M^2}{u\rho Ck})$$

λ effective latent heat of solidification

$$(= \frac{L + C(T_M - T_S)}{CT_S})$$

ACKNOWLEDGEMENT

I would like to thank my research directors, Dr. Fred Weinberg and Dr. Keith Brimacombe, for their assistance and guidance throughout the course of this research project. I would also like to thank W.A. Rachuk, the Radiation Protection Officer at U.B.C., for his assistance during the experiments.

The interest and cooperation of the management and staff of Western Canada Steel, Manitoba Rolling Mills, Atlas Steel, Algoma Steel and U.S. Steel is gratefully acknowledged.

1. INTRODUCTION

1.1. General Comments

The first commercial facility for the continuous casting of steel in North America was installed at the Atlas Steel Company plant in Welland, Ontario, in 1954. Large scale production in North America of mild steel by continuous casting started in about 1960. Since that time there has been a rapidly accelerating increase in steel production, using continuous casting, throughout the world, reaching a capacity of 75 million tons in 1971. A wide variety of products are produced including billets, blooms, slabs and beam blanks, with a range of compositions varying from mild steel to stainless steel.

The acceptance of continuous casting over normal conventional ingot teeming is due to a number of different factors: 1. Current steel production practices, in which the BOF is replacing the open hearth, results in an effectively continuous supply of liquid metal. This continuous supply is therefore directly compatable with continuous casting. 2. Lower initial capitol costs, e.g., large blooming mills and soaking pits are not required. 3. Lower operating costs, e.g., molds and mold shops are eliminated. 4. Higher yield. 5. Improved quality of the cast

product. 6. More efficient handling of the cast product in subsequent operations.

The change in casting practice on going from ingot teeming to continuous casting requires significant changes in the steelmaking operation. In general the control of melt temperature, homogeneity of the melt and deoxidation practices are more critical in continuous casting. Higher or lower melt temperatures can cause breakouts or plugged nozzles respectively, stopping the casting operation. In addition the casting undergoes much less reduction in subsequent operations. As a result cracks, imperfections and segregation in the casting are more pronounced in the rolled product.

The continuous casting operation is most efficient, economically, when large heats are cast (200 tons). The heat must be cast within about an hour since neither the ladle nor the tundish are heated during casting. In order to cast the large heat in the time available multiple strand casting machines are employed. In addition the casting rate per strand is being increased by suitable design of the machine and operating conditions.

Both multiple strands and higher casting rates impose more stringent conditions on the casting operation. Tundish design, nozzle geometry, mold design, cooling water spray configurations and alignment among other factors must be considered. For example, the United States Steel Company, South Works, is using computer controlled water sprays for submold cooling. With this control 19 cm. square billets can be cast at speeds up to 6 cm./sec.

The continuously cast steel quality is a function of the defects and segregation in the steel. The defects which are commonly found include: 1. non-metallic inclusions, which are also obtained in normal castings, the size and distribution being directly related to the steel-making and casting practice, 2. corner and radial cracking associated with the mold design and water spray cooling practice during solidification, 3. centreline or star-like cracks due to improper cooling of the solid strand, 4. centreline porosity, 5. transverse and longitudinal surface cracks due to stresses introduced in the solid strand by bending and straightening operations, 6. distortion of the strand (rhomboidity) due to uneven cooling or misalignment of the withdrawal and retaining rolls, 7. V segregates and central area porosity associated with the solidification process, 8. high inclusion concentration at the surface of the strand due to segregation and entrapment of the inclusions at the meniscus and the mold wall.

Considerable research has been carried out to increase the efficiency of the continuous casting operation and to control within acceptable limits, the defects in the cast steel. This work has included: 1. tundish and nozzle design to determine and control the fluid flow during casting and therefore, the reoxidation and inclusion distribution in the cast steel, 2. attempts to relate cast structure to the casting parameters, 3. a study of corner cracking as a function of corner radius in the mold, 4. use of heat transfer calculations to predict the pool profile and depth during casting as a means of establishing more efficient operating conditions, and for machine design. The results of some of this

research and development activity are reported below.

1.2. Previous Work

1.2.1. Fluid Flow and Liquid Pool

A theoretical model of the fluid flow in the liquid pool during casting has been proposed by Szekely and Stanek[1]. In the analysis of the model system, they examined, theoretically, the steady state and transient dispersion of radioactive tracers added to the pool for three different flow conditions. These conditions included eddy diffusion, potential flow and complete mixing. The analysis indicated that discernably different flow patterns would be obtained for the three conditions specified. However, no experimental evidence was presented to establish the validity of the analysis under real conditions.

Mills and Barnhardt[2] considered the problem of high density inclusions on the surface of cast slabs. They constructed a water model of the nozzle and mold systems and examined the fluid flow characteristics as a function of the manner in which the input stream entered the liquid pool. They clearly demonstrated that the fluid flow associated with bifurcated immersed nozzles tended to keep inclusions away from the mold walls, whereas open pouring did not. The fluid flow with immersed nozzles or bifurcated nozzles produced controlled turbulence and stirring in the upper part of the mold preventing any second phase material from concentrating at the freezing steel interface around the mold periphery. Also the tendency for subsurface entrapment of inclusions was alleviated. The results were applied to a full scale continuous casting slab machine, and by introducing bifurcated immersed nozzles with a suitable lubricant, slabs

were cast with little inclusion concentration at the outside face. These were then suitable for subsequent rolling into sheet whereas open poured cast slabs were unacceptable.

Water model studies were also undertaken by Szekely and Yadoya[3]. In this study they measured the velocity contours in the mold region for "straight" and radial flow nozzles. For straight nozzles they found the penetration of the input stream to be from 4 to 6 mold diameters. A radial flow nozzle produced a relatively flat velocity profile within ½ to 1 mold diameter. This investigation also confirmed the earlier findings of Mills and Barnhardt that radial flow nozzles produced flow patterns more conducive to the floatation of inclusions than conventional straight nozzles. The investigation was not extended experimentally beyond the water model.

A number of workers[4-10] have tried to predict the pool profile, pool depth and fluid flow during continuous casting through the addition of radioactive tracers during casting and subsequent autoradiography. Varga and Fodor[4] reported results on the distribution of radioactive phosphorus (P^{32}), and tungsten pellets containing a small Co^{60} wire, in the liquid pool of continuous cast billets. Using the tungsten pellets they obtained pool depths of from 3.6 to 3.7 m.

Similar experiments have been reported by Kohn et al.[5], using W^{184} pellets to measure the pool depth and Au^{198} instead of P^{32} to outline the pool profile. Using the tungsten pellets they found the pool depth increased with increasing casting speed. For a 10.5 cm. billet the pool depth increased from 4.7 to 5.37 m. as the casting speed increased from 1.83 to 2.28 m./min.. The position of the tungsten

pellets also coincided with the bottom of the pool outlined by the radioactive gold indicating that the gold mixed throughout the liquid pool. Gautier et al.[6] in similar experiments on 10.5 cm. billets found that the tracers did not penetrate to the pool bottom. From the autoradiographs Kohn speculated that the flow pattern in the liquid pool consisted of two cells. In the upper cell in the mold, flow occurs down the centre of the strand and up the side walls. In the lower cell this pattern is reversed, the flow occurring down the outside surface and up the centre.

Morton and Weinberg[7] added radioactive gold and tungsten pellets during the continuous casting of billets in a Weybridge type mold. From autoradiographs of the cast strand they found that in the mold region the solid-liquid interface was sharply delineated by the gold and in the sub-mold region, partial mixing of the gold in the liquid pool occurred. The amount of mixing was related to the input stream penetration. The depth of the pool delineated by the gold was found to be less than the pool depth determined by the tungsten pellets. The fluid flow in the pool could not be considered quantitatively in terms of Szekely and Stanek's[1] analysis since the gold was introduced below the metal surface and was released over a period of several seconds. However, on a qualitative basis the results suggested that the eddy diffusion model of Szekely and Stanek was most applicable. The flow pattern proposed by Kohn[5] was not observed in any of the tests. Similar to earlier findings, the pool depth was found to increase with increasing casting speed.

Gomer and Andrews[8] added P^{32} and tungsten pellets to the mold on an experimental continuous casting machine to estimate solidification

rates and pool depths. They found that the pool depths indicated by the pellets were greater than that predicted by a linear extrapolation of the shell thickness in the mold (obtained from autoradiographs of the P^{32} distribution in the mold) but was less than that predicted by assuming a parabolic solidification rate below the mold. From autoradiographs in the mold they observed an uneven or wavy solidification front. The fluctuations were usually found to be periodic corresponding to the mold oscillation.

Using a radioactive tungsten pellet and scintillation counters positioned down the strand, Nagaoka et al.[9] estimated the pool depth for a slab, cast with a low-head curved mold machine. They found that for a slab 20 x 160 $cm.^2$ cast at 10.8 mm./sec., a pool depth of 7.5 m. was obtained. Also with the scintillation counters they estimated that the average rate of descent of the pellet was 84.2 mm./sec.

Zeder and Hestrom[10] added Au^{198} and Ag^{110} to a slab cast with a low-head curved mold machine to define the shell profile in the transverse sections in the mold and submold regions. In these tests an immersed, bifurcated shroud and a slag powder lubricant were utilized. They observed: 1. a thinning of the strand at the corners, 2. poor definition of the shell towards the centre of the pool along the wide faces of the slab, 3. incomplete mixing of the gold near the pool bottom, 4. a thin shell along one face when the support rollers were improperly aligned with the mold.

1.2.2. Structure

The structure of continuously cast steel has been examined using radioactive tracers, sulphur prints and macroetching techniques and has been related to different casting variables.[7,8,10-12] Radioactive tracers such as gold[7,10,11] and phosphurus[8] have been found to segregate in a similar fashion to sulphur, outlining the cast structure. Using these techniques it was possible to determine the length of the columnar zone, segregation and centreline porosity in the equiaxed zone and the presence of radial or centreline cracking.

Both Mori et al.[11] and Gomer and Andrews[8] found that with increasing casting superheat the length of the columnar zone in the casting increased and the centreline porosity and segregation became worse. A similar effect was observed by Morton and Weinberg[7] in which the cast structure of billets cast in a Weybridge type mold (3 billets per strand) was compared to the structure of a single strand cast billet. They observed that with the Weybridge mold, the cast structure consisted mainly of small equiaxed grains, whereas the single strand billet, cast at a slightly lower superheat had a coarse dendritic structure with bridging across the centreline and extensive centreline porosity. Thus, the size of the central equiaxed zone is dependent on the extent of mixing in the liquid pool and the casting superheat. The nuclei associated with the central equiaxed grains are believed to be generated[7] in the upper part of the liquid pool by remelting of secondary dendrite branches.

A V shaped segregation pattern has been observed on the longitudinal sections of billets in many different investigations.[7,8,11]

It has been suggested that the pattern results from the settling of free dendrites in the liquid pool and subsequent fluid flow by interdendritic liquid due to solidification shrinkage.

In tests on a slab[10] using Au^{198} a heavily segregated narrow central zone as well as local segregation between columnar dendrites was observed.

Cracks which formed during solidification and which were subsequently filled with interdendritic liquid, are often found in the cast structure of the strand.[7,8,12-14] Ushijima[12], in tests on a vertical casting machine, noted that the incidence of longitudinal surface cracks and internal cracks depended in a complex fashion on such parameters as the casting superheat, casting speed, primary cooling in the mold and secondary cooling in the spray and radiant zones. By careful control of the cooling and solidification conditions he found that the incidence of surface and internal cracks could be reduced. For instance, by choosing a mold corner radius that minimized the shell separation due to bulging and solidification shrinkage at the corner, longitudinal corner cracking was eliminated. The incidence of internal cracking was reduced by maintaining even cooling around the strand in the mold and submold regions, decreasing the intensity of cooling, reducing the stress due to the pinch rolls and prevention of local solute enrichment, i.e., fine grained structure over coarse grained structure.

In order to try to further explain internal and external cracking in the billet, Adams[13] measured the hot ductility and strength

of strand-cast steel to near its melting point. When the strand cast specimens were heated from room temperature and pulled, the ductility dropped drastically at temperatures greater than 1250°C. This was attributed to incipient liquid-film formation at grain boundaries.

Lankford[14] also studied this problem. Instead of re-heating as-cast specimens, he remelted specimens and under controlled conditions cooled them to the test temperature. Both tensile and bending tests were performed studying the effect of composition and prior thermal history. In general he found that:

1. Specimens that were rapidly cooled from the solidification temperature exhibited a low ductility between 800 and 1200°C. This is attributed to the precipitation of liquid FeS droplets in planar arrays at austenite grain boundaries, producing paths of easy crack propogation. A recovery of ductility in this temperature range was observed when a slower cooling rate or isothermal heat treatment was applied. The recovery results from the coalescence and growth of precipitates and the formation of the more stable MnS.

2. With increasing Mn/S ratios the loss of ductility becomes less severe because of the low solubility of MnS in the iron; also the precipitation of MnS is more favorable than FeS.

3. Under sufficiently high tensile stress hot tears can occur in portions of the casting which are in the low ductility temperature range.

1.2.3. Mathematical Models

There have been a number of mathematical models[6,15-22]

formulated to calculate the heat flow and temperature distribution in the strand during the continuous casting of steel. These models involve the solution of the unsteady state conduction equation using either analytical (Pehlke[15], Hills[16], Fahidy[20], Savage[22]) or numerical (Gautier et al.[6], Donaldson and Hess[17], Mizikar[18], Kung and Pollock[21]) methods. The mathematical models differ in the treatment of the method of removal of superheat from the liquid pool and in the surface boundary condition used to describe the heat flux from the casting to the mold.

Regarding the removal of superheat, Mizikar[18] and Kung and Pollock[21] accounted for convection and conduction in the liquid pool by using an effective thermal conductivity which was approximately seven times the normal liquid conductivity. Donaldson and Hess[17] and Gautier et al.[6] assumed a stagnant liquid pool and used the normal value of the thermal conductivity at that temperature. On the other hand Hills[16] assumed the pool was completely mixed, neglected conduction in the pool, and released the superheat at the same time as the latent heat. Szekely and Stanek[1], using the mathematical model proposed by Mizikar, varied the method of superheat removal from the pool. They found that there was no observable difference in the computed solidus and liquidus lines when the flow conditions or the method of superheat removal were altered. This is understandable because the superheat is only a small fraction of the latent heat; therefore it will not have a large effect on the calculated solidification rate.

Many different approaches have been taken to account for the surface boundary condition in the mold. Donaldson and Hess[17] and Gautier et al.[6] used a two zone heat transfer model, incorporating a zone

of good contact between the casting and the mold and a zone of poor contact. The length of the zone of good contact was calculated by Donaldson and Hess by applying a method proposed by Savage[22]. In this calculation the length of contact depended upon the elastic modulus of the steel at elevated temperatures, the width of the shell and the casting speed. Gautier et al.[6] calculated the zone of good contact by employing a heat balance on the mold. The total heat flux in each zone was calculated and the results were compared to the measured mold heat flux. The length of the zone of good contact was then varied until the measured and the calculated heat flux values coincided.

Kung and Pollock[21], in their two-dimensional finite difference model, compared the effect of using an average overall heat transfer coefficient in the mold and using three different coefficients along the length of the mold to account for partial contact. From the predicted temperature profiles at the mold bottom they found a 2 to 6% increase in surface temperature when using three mold coefficients. This temperature difference had virtually no effect on the calculated pool profile or pool depth.

Both Mizikar[18] and Hills[16] took simpler approaches in defining the surface boundary condition in the mold. Mizikar employed the heat flux relationship found experimentally by Savage and Pritchard[23]. This relationship was determined from experiments on a static water-cooled copper mold by measuring the rate of heat removal by the mold cooling water as a function of time. The results from these experiments were found to compare favourably with data presented by Krainer and Tarmann[24]. Hills[16] calculated an average overall heat transfer coefficient from an integral heat balance

on the mold. Later Hills[19] modified this approach by assuming a linearly decreasing heat transfer coefficient down the mold. Brimacombe and Weinberg[25] calculated pool profiles with Hills model using either an average overall or linearly decreasing mold heat transfer coefficient. These were compared to profiles experimentally measured by Morton and Weinberg[7]. They found that for low carbon steel the predicted profiles using the Hills model with either heat transfer coefficient agreed closely with the measured profiles. Predictions using Mizikar's model were also found to compare favourably to the values measured at the mold bottom.

Another area in which the models differed was in their treatment of the thermophysical properties of steel. Hills in solving the heat flow equations using the integral profile method, assumed the thermophysical properties were constant. Mizikar, Kung and Pollock and Gautier et al. allowed the specific heat and thermal conductivity to vary with temperature while keeping the density constant. Kung and Pollock found that by keeping the thermal conductivity constant, the pool depth changed from 6-11%. In the finite difference models Mizikar and Kung and Pollock differ from Gautier et al. in their treatment of the addition of the latent heat of fusion. Both Mizikar and Kung and Pollock assume that the latent heat can be accounted for by adjusting the specific heat over the range of solidification. Gautier et al. assume the steel can be characterized by an enthalpy-temperature curve which includes the latent heat of fusion.

In several of the mathematical models[6,17,18,21] calculations of the heat flow have been extended into the submold region. This requires the estimation of spray heat transfer coefficients for the secondary cooling zone. Since little information is available regarding water spray

cooling, the procedure adopted in most models was to allow the program to generate a spray heat transfer coefficient which could be used without dropping the surface temperature of the strand below the austenite-ferrite transformation temperature.

Recently an investigation of water spray cooling was undertaken by Mizikar[26]. In this investigation he determined the spray heat transfer coefficients as a function of water flux for three different nozzle sizes and different spray pressures. An important result from this work was that the heat extraction efficiency per drop (water drop from spray) increases greatly with droplet size and the corresponding increase in droplet momentum. Thus by determining the heat extraction for a certain droplet size and droplet momentum (supplied for all nozzles by the vendor), heat transfer coefficients for different nozzle sizes and spray configurations could be estimated.

1.2.4. Objectives of Present Work

The purpose of the present investigation is: 1. to determine, through the use of radioactive tracers, the liquid pool profiles, pool depths, fluid flow and cast structure of continuously cast steel as a function of different casting conditions and casting sizes, 2. to develop a mathematical model to calculate the temperature distribution in steel being continuously cast; and to assess its reliability by comparison of predicted and measured pool profiles.

2. MATHEMATICAL MODEL

2.1. Heat Flow Equations

A thin horizontal section of the casting shown by the shaded area in Figure 1 is considered. The section is initially located at the meniscus and, at times greater than zero, moves downward at the same speed as the casting, successively passing through the mold, water sprays and radiant cooling zones.

Within the section heat conduction to the surface can be characterized by the unsteady state conduction equation (1),

$$\rho\frac{\partial H}{\partial t} = \nabla(k\nabla T) \tag{1}$$

Equation (1) may be simplified by assuming that heat conduction in the direction of withdrawal, x, is small and can be neglected, thus giving the two-dimensional unsteady state conduction equation (2),

$$\rho\frac{\partial H}{\partial t} = \frac{\partial}{\partial y}\left(k\frac{\partial T}{\partial y}\right) + \frac{\partial}{\partial z}\left(k\frac{\partial T}{\partial z}\right) \tag{2}$$

This assumption will apply for analysing heat removal from blooms or billets. In the case of slabs, (far from corners) conduction in the z direction can be ignored thus reducing equation (1) to its one-dimensional form,

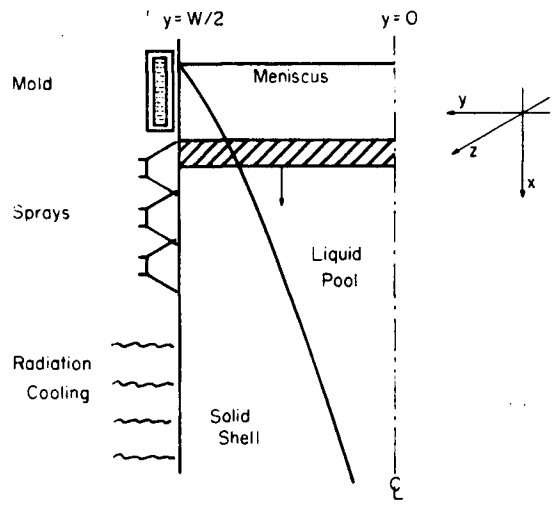

Figure 1. Heat transfer zones in continuous casting.

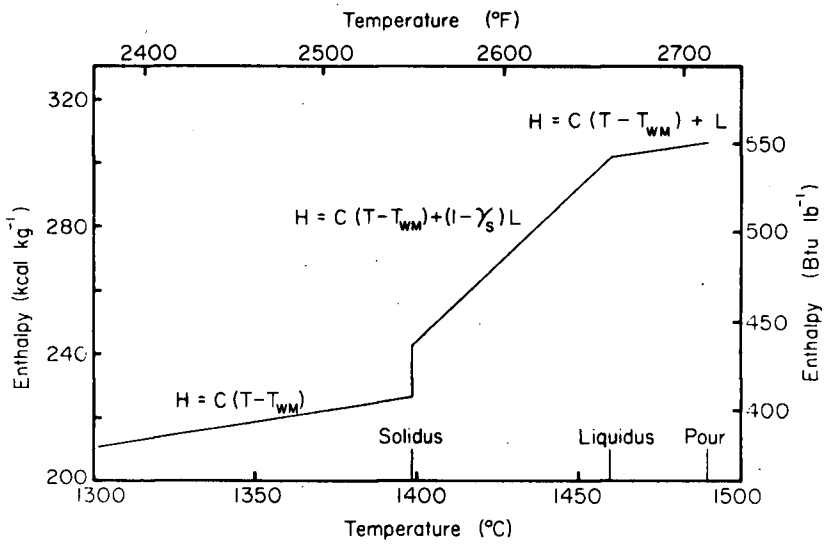

Figure 2. Dependence of enthalpy on temperature for the stainless steel slab.

$$\rho\frac{\partial H}{\partial t} = \frac{\partial}{\partial y}\left(k\frac{\partial T}{\partial y}\right) \tag{3}$$

The assumptions involved in applying equations (2) and (3) in the models are:

1. The density and specific heat are constant over the temperature range considered.
2. The thermal conductivity can be characterized as a linear function of temperature

$$k = a + bT \tag{4}$$

3. Conduction and convection of heat in the liquid can be accounted for by adjusting the thermal conductivity.

In the solutions to equations (2) and (3) the specific heat and density terms usually take the form of a product. Since these terms increase and decrease[27] respectively with increasing temperature, their product does not vary significantly over the temperature range of interest for both stainless and low carbon steels.

Conduction and convection of heat in the liquid can be described by

$$\rho\frac{\partial H}{\partial t} = k_{eff}\frac{\partial^2 T}{\partial y^2} + k_{eff}\frac{\partial^2 T}{\partial z^2} \tag{5}$$

where k_{eff} is an effective thermal conductivity which includes the effects of convective mixing. Mizikar[18] and Kung and Pollock[21] have previously used this approach and have reported an effective thermal conductivity roughly seven times greater than the liquid thermal conductivity. This value was used in the models over the region of the section where the

temperature was greater than the liquidus. The effect of varying the temperature range over which k_{eff} was used was determined and is discussed in a later section.

In the model a procedure must be adopted for incorporating the latent heat evolved in the solid-liquid region during solidification. Since the evolution occurs in a complex fashion, as a result of the complex configuration of the solid-liquid interface, a simplified process must be assumed.

Specifically, in the case of stainless steel, the fraction of metal solidified, γ_s, was arbitrarily given a value such that 75% of the latent heat was released in a linear fashion between the solidus and liquidus temperatures with the remaining 25% being given off at the solidus. This arbitrary choice of latent heat removal had a negligible effect on the calculated rate of solidification as will be shown later. The graph of enthalpy versus temperature for the stainless steel along with the equations for enthalpy over each region is given in Figure 2.

For the low carbon steels, equilibrium freezing has been assumed and γ_s has been calculated from the iron-carbon phase diagram. In this case depending on the carbon content roughly 5 to 25% of the latent heat was released at the solidus temperature which corresponded to the peritectic temperature.

2.2. Initial and Boundary Conditions

The initial and boundary conditions used in the solution of equation (2) are as follows:

(i) $t = 0$ $\quad 0 < y < \frac{W}{2}, \quad 0 < z < \frac{W}{2}, \quad T = T_M$

(ii) $t \geq 0$ $\quad y = \frac{W}{2} \quad -k\frac{\partial T}{\partial y} = 0$

$z = \frac{W}{2} \quad -k\frac{\partial T}{\partial z} = 0$

(iii) $t > 0$ $\quad y = 0 \quad -k\frac{\partial T}{\partial y} = q_{o_y}$

$z = 0 \quad -k\frac{\partial T}{\partial z} = q_{o_z}$

The initial condition states that the temperature of the section at the meniscus is equal to the temperature of the incoming metal stream, T_M. The centreline boundary condition (at y = W/2 and z = W/2) assumes that the heat flux about the centrelines of the casting is symmetrical; therefore, only one quarter section of the casting need be considered. To obtain the surface boundary condition, at y = 0 and z = 0, a heat balance was performed on the surface node, q_o representing the surface heat flux term. It should be noted that the heat flux around the perimeter of the bloom is assumed to be constant, so that q_{o_y} is equal to q_{o_z}. The surface heat flux term was characterized in each of the three cooling zones by the following expressions:

(i) Mold $\quad q_o = 640 - 80\sqrt{t}$ (6)

or

$q_o = \bar{h}_M (T_o - T_{WM})$ (7)

(ii) Sprays $\quad q_o = \bar{h}_S (T_o - T_{WS})$ (8)

(iii) Radiation $\quad q_o = \sigma F (T_o^4 - T_a^4)$ (9)

These equations of the initial and boundary conditions apply to the two-dimensional model and with suitable modification to the one-

dimensional finite difference and integral profile models.

Equation (6) is an expression experimentally obtained by Savage and Pritchard[23], which describes the time dependent heat flux from a water cooled, static mold. The time-averaged form of equation (6)

$$\bar{q}_o = 640 - 53\sqrt{t_M} \tag{10}$$

predicts average mold heat fluxes which agree well with measured fluxes under a variety of casting conditions. In Figure 3, the average mold heat flux is plotted against dwell time in the mold. The solid line, calculated from equation (10), can be seen to pass through the values obtained from commercial molds for dwell times less than 35 to 40 sec. The vertical bars indicate the range in which most of the heat fluxes for a given mold were found. Equation (6) has been previously used by Mizikar[18] for the surface boundary condition in the mold. For the purposes of design equation (6) may be used to predict with reasonable accuracy the shell thickness of the strand in the mold. From this data, given a certain shell thickness required to withstand the ferrostatic head on exit from the mold, the mold length and maximum casting speed for the strand may be estimated.

In equation (7), $\bar{h}_M$ is the average, overall heat transfer coefficient between the casting surface and the mold water. Hills[16] has outlined a method for determining $\bar{h}_M$ by using an integral heat balance on the mold. Tables I and II give the values used in calculating the heat balance on the mold and the values of $\bar{h}_M$ obtained for the tests.

For the purposes of design, since very few values of $\bar{h}_M$ have been available in the literature, $\bar{h}_M$ may be calculated from heat fluxes obtained in equation (10) giving

Table I. Thermophysical Properties of Steel

Property	Stainless	Low Carbon
Thermal Conductivity (kcal m^{-1} $sec.^{-1}$ $°C^{-1}$)	0.0038 +	$2.75(10^{-6})T$
Specific Heat (kcal kg^{-1} $°C^{-1}$)	0.16	0.16
Latent Heat of Solidification (kcal kg^{-1})	65	65
Density (kg m^{-3})	7400	7400
Solidus Temperature (°C)	1399	1492*
Liquidus Temperature (°C)	1460	1525

*For 0.1 to 0.2% C
For 0.3% C, Solidus Temperature 1470°C.

Table II. Parameters Used in Integral Profile and Finite Difference Calculations.

Test No.	Q_o (kcal $sec.^{-1}$)	λ	Q^*	x^*	$\bar{h}_M$ (kcal m^{-2} $sec.^{-1}$ $°C^{-1}$)
M1	131	0.3	0.372	0.189	0.283
M2	139	0.3	0.351	0.164	0.295
M3	142	0.3	0.459	0.325	0.427
M4	159	0.3	0.484	0.375	0.499
At1	482	0.3	0.532	0.488	0.370
Aℓ1	352	0.308	0.474	0.354	0.283
Aℓ2	353	0.298	0.426	0.267	0.242
Aℓ3	170	0.304	0.430	0.273	0.252
Aℓ4	145	0.315	0.358	0.173	0.208
U11	445	0.3	0.578	0.618	0.526

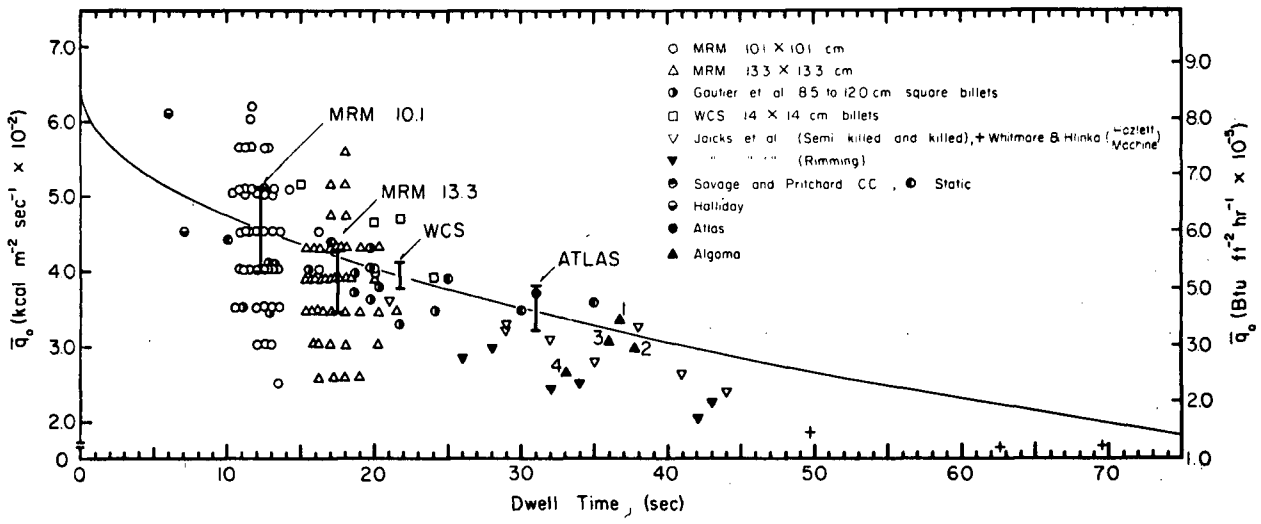

Figure 3. Average flux of heat extracted by the mold as a function of dwell time.

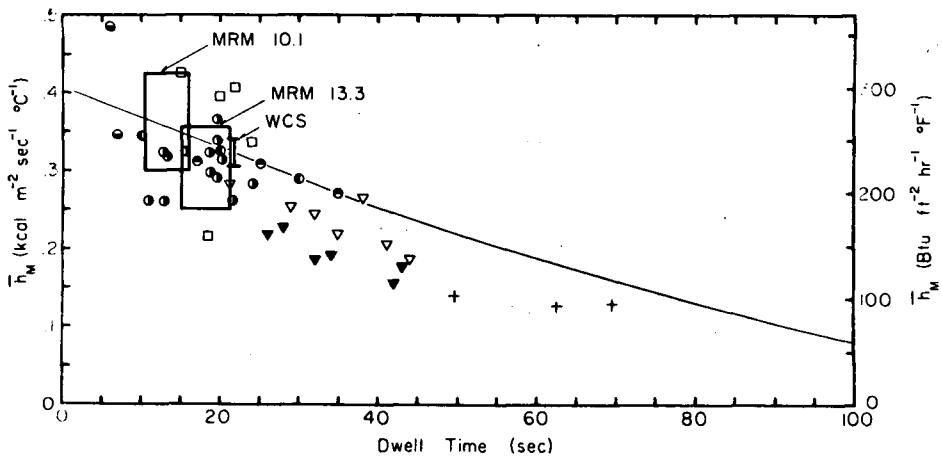

Figure 4. Average, overall heat transfer coefficient for the mold as a function of dwell time.

$$\bar{h}_M = .405 - 0.00386\ t_M \qquad (11)$$

This relation is shown in Figure 4[28], a plot of $\bar{h}_M$ against dwell time in the mold. Heat transfer coefficients for different molds and casting conditions are also plotted in Figure 4. From the graph it can be seen that equation (11) gives values of $\bar{h}_M$ which are obtained in practice under "average" casting conditions for dwell times less than about 35 sec.

Hills[19] also suggested using a linearly decreasing heat transfer coefficient in the mold, equation (12),

$$h_M = h_o(1 - \eta x) \qquad (12)$$

to characterize the heat flux from the casting surface, h_o being equal to h_M at the meniscus. Brimacombe and Weinberg[25] have shown that even with h_M decreasing to half its initial value at mold bottom, the change in the calculated shell thickness compared to the constant $\bar{h}_M$ case is small. Also it is difficult to distinguish which of the two cases is most applicable when comparing calculated shell thicknesses to measured shell thicknesses.

Values of the spray heat transfer coefficients, $\bar{h}_S$ used in equation (8), are presented in Table III. These values were roughly estimated by obtaining the water flux per unit area in each spray zone of a casting machine from the spray nozzle size, spray configuration and spray pressure. Then using spray data obtained by Mizikar[26], presented in Figure 5, $\bar{h}_S$ for each spray zone was determined. These values were subsequently altered in the computer solution so that the calculated surface temperature of the strand did not fall below 850°C. Mizikar's

data could not be used directly to give $\bar{h}_s$ since the spray configurations in the continuous casting machines were different than the ones used in his investigation. Also support rolls pressing against the strand surface in the spray chambers would have an unknown effect on $\bar{h}_s$.

2.3. Method of Solution

The unsteady state conduction equations (2) and (3) with the appropriate boundary conditions were solved by the explicit method of finite differences. The details of the solution are given in the Appendix.

Table III. Characteristics of Heat Transfer Zones.

Heat Transfer Coefficients, $\bar{h}_S$ (kcal $m^{-2} sec.^{-1} °C^{-1}$)

Western Canada Steel			Manitoba Rolling Mills				Atlas Steel			U.S. Steel			Algoma Steel								
														Beam Blank					Bloom	
Zone	Length (m)	$\bar{h}_S$	Zone	Length (m)	$\bar{h}_S$ (10.1cm)	$\bar{h}_S$ (13.3cm)	Zone	Length (m)	$\bar{h}_S$	Zone	Length (m)	$\bar{h}_S$	Zone	Length (m)	'A' Profile 1	'A' Profile 2	'E' Profile 1	'E' Profile 2	Length (m)	Test AL3	Test AL4
1	0.31	0.49	1	0.3	0.45	0.41	1	0.91	0.42	1	0.38	0.6	Spray Ring	0.15	0.14	0.26	0.17	0.23	0.15	0.25	0.23
2	0.83	0.18	2	1.52	0.22	0.21	2	0.92	0.30	2A	0.49	0.31	1A Top	0.61	0.17	0.20	0.16	0.23	0.915	0.15	0.14
3	0.88	0.13	3	3.66	0.1	0.1	3	1.52	0.18	2B	0.73	0.175	1A Bottom	0.94	0.16	0.17	0.15	0.2	0.635	0.15	0.14
							4	2.14	0.15	3	2.13	0.15	1B	1.925	0.13	0.13	0.12	0.12	2.18	0.11	0.105
										4	2.15	0.11	2	1.925	0.10	0.10	0.10	0.10	2.18	0.08	0.08
										5	5.1	0.09	3	3.05	0.07	0.07	0.07	0.07	2.68	0.07	0.07
													4	3.05	0.07	0.07	0.07	0.07	2.68	0.06	0.06

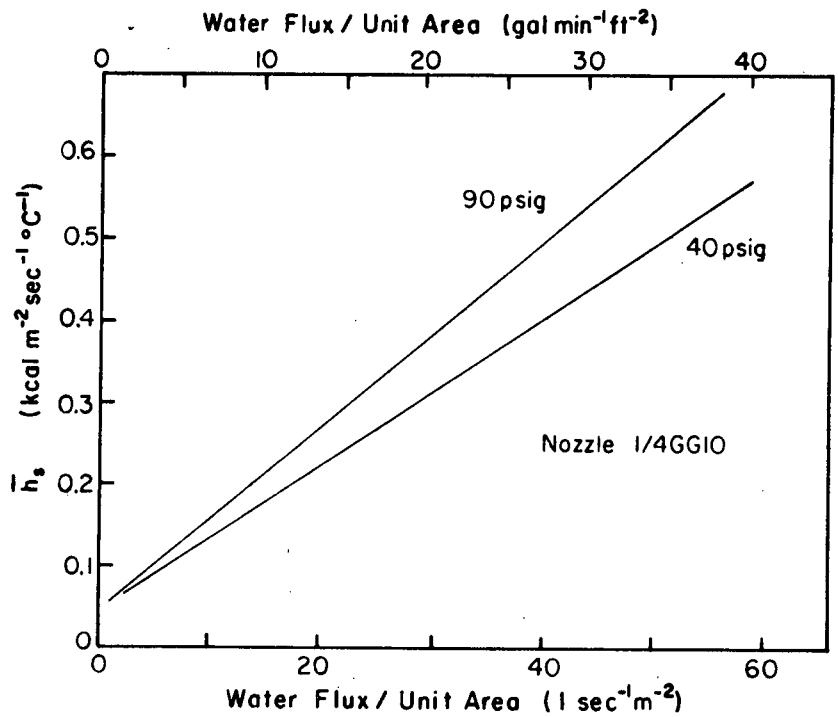

Figure 5. Estimated spray heat transfer coefficient as a function of spray water flux per unit area.

3. METHOD

3.1. Continuous Casting Operations

3.1.1. General Description

The experiments were conducted on straight mold, vertical bend and low-head curved mold continuous casting machines. A schematic diagram of the two different types of casting machines is given in Figure 6. In Table IV the type of machine used at each steel company where tests were conducted is listed, together with a description of the cast product, mold lubrication and mold dimensions. Also, in low-head curved mold machines, the radius of curvature of the casting is given. In each experiment the withdrawal rate, water flow rate in the mold and the water temperature drop in the mold were recorded and are listed in the results.

3.1.2. Western Canada Steel

At Western Canada Steel[29], three billets are cast simultaneously using a Weybridge type mold, the billets being joined across the diagonal by a thin web region. The mold consists of two sections, split along the diagonal and is made of a cast copper chromium alloy. Open teeming from

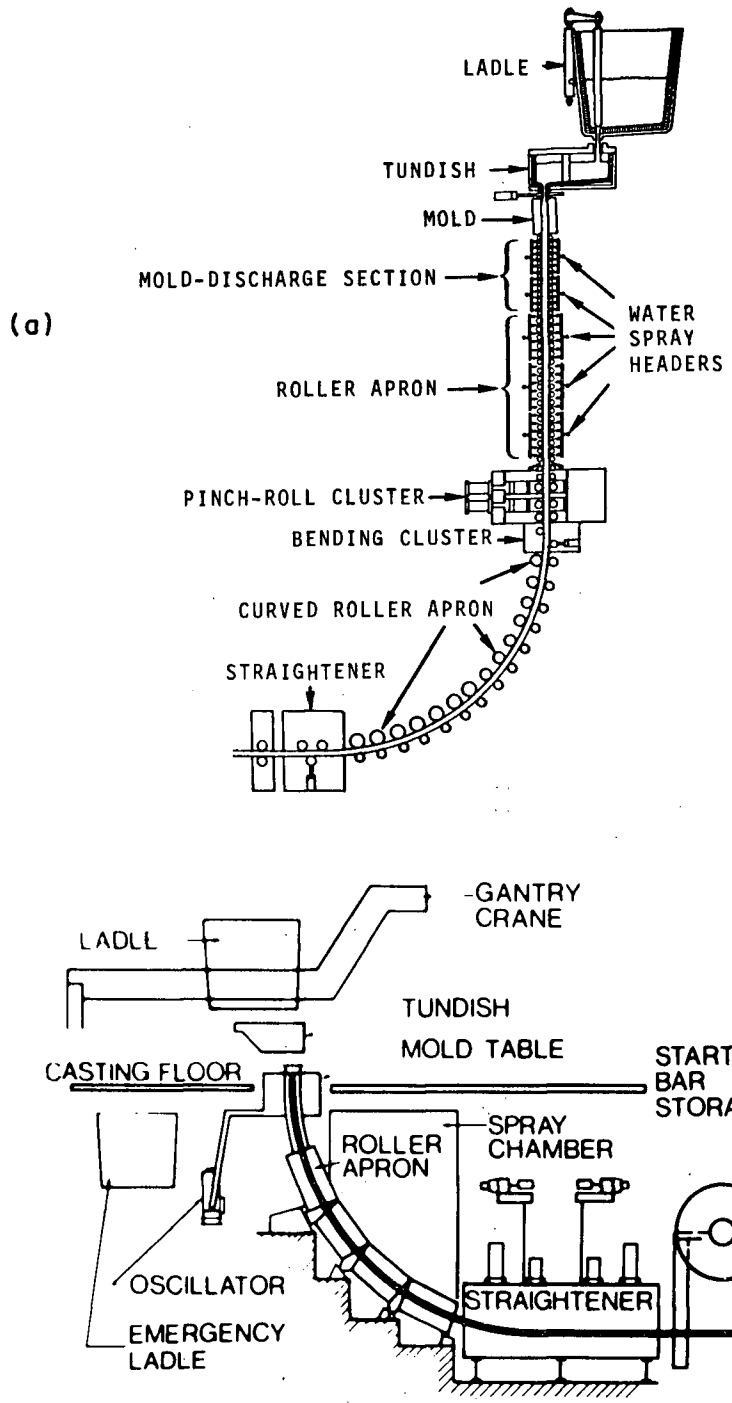

Figure 6. (a) Schematic of straight mold, vertical type casting machine with bending.
(b) Schematic of low-head, curved mold casting machine.

Table IV. Casting Machines Details.

Test No.	Steel Company	Machine Type	Steel	Lubrication	Size & Description of Castings (cm^2)	Hold Length (cm)	Dist. of Meniscus Below Moid Top (cm)	Radius of Curvature (m)
W1,W2	Western Canada Steel	Vertical bend straight, Weybridge mold	Low and medium carbon	Rapeseed Oil	14x14 Billets	62	11	-
M1,M2	Manitoba Rolling Mills	Low head, curved mold	Low and medium carbon	Rapeseed Oil	13.3x13.3 Billets	81.3	15	6.7
M3,M4					10.1x10.1 Billets	81.3	15	6.7
At1	Atlas Steel	Low head, curved mold	Stainless Steel	Mold* Powder	12.7x109 Slab	61	9	9.2
Aℓ1	Algoma Steel	Low head, curved mold	Low and medium carbon	Synthetic Oil†	843, A profile Beam Blank	71.2	15	10.7
Aℓ2				Mold Powder**	1015, E profile Beam Blank			
Aℓ3				Synthetic Oil†	22.9x26.7 Bloom			
Aℓ4				Mold Powder**	22.9x26.7 Bloom			
U1	U.S. Steel	Vertical Bend	Low and Medium Carbon	Rapeseed Oil	19x19 Billet	122	20	-

* Fusion Temperature 1150°C.
** Fusion Temperature 960°C.
† Proctor-Gamble Synthetic Oil.

the tundish into the centre section of the mold is used. The flow of metal is controlled manually using a stopper rod in the tundish, therefore, the flow of the input stream is intermittent. The mold is oscillated at approximately 1 cycle/sec. during normal casting and has a stroke length of 2.5 cm. Approximately 9.2 m. below the mold (see Figure 6(a)), the strand is bent through a 6.40 m. radius to a horizontal position. The billets are then separated by cutting the web with torches and mechanically sheared to the desired lengths.

3.1.3. Manitoba Rolling Mills

Manitoba Rolling Mills[30] has two low-head curved mold machines (Figure 6(b)), each machine casting two square sections from a single tundish. Open teeming from the tundish is used, with the liquid level in the mold being maintained at a constant position automatically. This is accomplished by using a radioactive source and detector device to determine the liquid level and varying the withdrawal rate to keep the level constant. During the tests, the liquid level was adjusted by the operator, since the radioactive tracer addition to the melt made the automatic instrument inoperative. Tubular chromium plated copper molds are used. The molds are oscillated at a rate proportional to the casting speed, having a stroke length of 3.8 cm. Each strand after passing through the casting machine is sheared into the required lengths.

3.1.4. Atlas Steel

One test was conducted at the Atlas Steel Company in Tracy, Quebec, on a low-head curved mold, Concast Inc. slab machine[31] . The

material cast was stainless steel of the composition given in Table V, with slab dimensions of 12.7 x 109 cm. The mold is formed with copper plates rigidly held in a steel enclosure and is reciprocated at 1 cycle/sec. with an amplitude of 1.3 cm. The liquid steel enters the pool from the tundish through an immersed bifurcated tube. The input stream from the tube is directed parallel to the long face of the steel slab and inclined upwards by 20°. The strand is flame cut into the required lengths after passing through the casting machine.

3.1.5. Algoma Steel

Algoma Steel Corporation has two low-head, curved mold, continuous casting machines consisting of a four-strand bloom machine, producing blooms up to 26.7 x 35.6 $cm.^2$, and a two-strand beam blank machine which casts five different blank sections ranging from 843 to 1435 $cm.^2$. These machines are presently being used for casting structural grades of steel, high-carbon steel for the grinding media, seamless tube grades and rails.

Each machine is fed from a single tundish. For the beam blank, two nozzles are required for each strand whereas for the bloom, a single nozzle per strand is used. For the casting of aluminum killed steels, the bloom tundish is fitted with a four-holed submerged entry shroud. The input streams from the shroud are directed perpendicular to the mold face and are inclined 15° above the horizontal. When using a shroud, a slag powder lubricant is used in the mold. The liquid metal level in the mold is controlled manually by varying the withdrawal rate (1.5 to 1.7 cm./sec.) of the strand. The total distance from the meniscus level in the mold to the tangent roll in the straightener is 16.7 m., with an additional 15.8 m.

to the torch cut-off units.

The molds are oscillated sinusoidally with a stroke length of 1.9 cm. The frequency of oscillation is matched to the casting speed. All molds are hard chrome plated to improve mold life and reduce maintenance. The bloom molds are of plate construction[32], comprised of 3.8 cm. copper plates, with a 0.317 cm. corner radius and a 0.152 cm. taper on the nonradial sides.

The first generation ('A' profile, Test Aℓ1) beam blank molds consist of a solid copper block split into two segments about the centreline of the flange faces. The mold halves are tightly clamped by jackbolts. Cooling of the mold is accomplished by means of 3.12 cm. diameter water-cooling channels drilled around the perimeter of the mold cavity. The second generation ('E' profile, Test Aℓ2) beam blank mold is different from the first-generation in that the flange face portion of the molds are identical to plate mold sections. The remainder of the mold is similar to the first-generation mold (i.e., solid block copper with cooling water passages).[33] The second-generation molds are considerably less expensive and are easier to machine than the first-generation molds.

3.1.6. U.S. Steel

The casting machine at the United States Steel plant at South Works, Chicago, is a four strand, straight mold, vertical type casting machine with bending (Figure 6(a)). It was designed for casting 19 cm. billets at speeds up to 8.5 cm./sec. During normal production the casting speed is usually 5.5 cm./sec. Automatic mold liquid-level control is used. This device uses thermocouples in the top portion of the mold to determine

the liquid level and automatically varies the withdrawal rolls to keep this level constant. On exit from the casting machine the billet passes through a system of in-line induction heating and in-line rolling, producing a semifinished product from 10 x 10 $cm.^2$ to 15 x 15 $cm.^2$.

3.2. Procedure

The tests were conducted during normal operations in the plant. Stable casting conditions were obtained by waiting until half of the heat had been poured before adding the radioactive materials. The amounts of radioactivity used in each test are given in Table V. In some tests the liquid temperature in the mold was measured prior to the addition of the radioactive gold. Measurements were made with a Pt-Pt 13% Rh thermocouple contained in a quartz sheath.

Radioactive gold (Au^{198}- $\beta + \gamma$, half-life 2.7 days), in the form of a small cylinder 0.32 cm. in diameter by 0.63 cm. long, was added to the liquid pool in the mold by inserting a 0.64 cm. diameter stainless steel rod containing the gold into the pool directly below the input stream. For tests conducted on the beam blanks and the slab, two gold additions (one to each input stream) were made to each strand, whereas in all other tests a single addition was made. The stainless steel rod, inserted into the liquid to a depth of approximately 15 cm. below the meniscus, melted within 5 sec. releasing the gold into the pool. In some tests a tungsten pellet, 1.25 cm. in diameter by 1.25 cm. long containing two millicuries of Co^{60}, was dropped into the pool directly below the input stream simultaneously with the gold addition. The position of the pellet in the steel was located with a geiger counter subsequent to casting and related to the determined position of the

Table V. Experiment, Casting Parameters and Pool Depth.

Test No.	Experiment	Total Activity Au^{198} used (mC)	Tundish Teeming	Temperature Tundish (°C)	Temperature Mold (°C)	Surface Temp. Straightener (°C)	Mold Water ΔT (°C)	Mold Water Flow Rate ($m^3 sec.^{-1} x10^2$)	Mold Heat Flux (kcal $m^{-2} sec.^{-1}$)	Casting Speed (cm $sec.^{-1}$)	Pool Depth Gold (m)	Pool Depth Tungsten (m)	Pool Depth Calc. (m)
W1a	W-pellet	-	Open pour	-	1493	-	5.3	8.2	505	2.54	-	3.07	8.23
W1b							4.2		400	1.69		2.54	4.40
W1c							3.5		335	1.48		1.80	3.71
W2a	W-pellet	-	Open pour	-	1499	-	4.0	8.2	419	2.37	-	3.53	7.41
W2b							3.5		335	1.78		2.26	4.76
W2c							3.3		315	1.56		1.85	4.00
M1	Gold	75	Open pour	1513	1500	1055	4.7	2.78	358	3.5	3.0	-	9.15
M2	Gold + W-pellet	75		1513	1500	1055	5.0	2.78	380	4.4	3.0	6.0	12.54
M3	Gold + W-pellet	75		1527	-	1010±11	5.6	2.54	510	4.65	2.5	3.25	7.35
M4	Gold + W-pellet	75		1544	-	-	6.1	2.61	572	5.5	2.5	3.7	9.52
At1	Gold + W-pellet	400	Immersed shroud	1480	-	-	8.5	5.68	324	1.65	2.3	2.65	3.72-5.36*
Aℓ1	Gold + W-pellet	500	Open pour	1546	1504	-	8.6	4.09	335	1.52	2.0	2.28	7.3**
Aℓ2	Gold	500	Open pour	1532	-	900	8.4	4.24	297	1.48	1.5	-	7.1**
Aℓ3	Gold + W-pellet	200	Open pour	1541	1507	900	5.0	3.41	308	1.56	3.3	1060†	12.9
Aℓ4	Gold	200	Immersed shroud	1525	-	900	4.2	3.49	262	1.69	1.8	-	14.9
U1	Gold	200	Open pour	1540	-	-	8.3	5.36	575	5.5	2.8	-	32.3

* One-dimensional Integral Profile and Finite difference estimate of pool depth.
** Pool depth beneath input stream.
† Estimated from position of pellet - 693 cm., below meniscus.

meniscus. The position of the pellet in relation to the central axis of the strand was found by flame cutting through the strand to expose the pellet.

After the strand had cooled, it was flame cut into sections, along planes both parallel and transverse to the longitudinal central axis. The cuts parallel to the central axis were perpendicular to the plane of curvature. After cutting, the exposed surfaces were milled and then autoradiographed by placing the milled surface on X-Ray film. Exposure times varied from 1 hour to 4 days, depending on the activity of the particular section. The outer edge of the section being autoradiographed was delineated on the film by exposing the film not covered by the section to light.

4. RESULTS

4.1. Liquid Mixing, Solid Shell and Cast Structures

4.1.1. General Observations of the Test Results

In Tables V and VI, the steel composition, type of experiment, casting parameters and pool depths are given for all of the tests. Composite photographs of the autoradiographs showing the distribution of gold in the liquid pool for the tests are presented in Figure 7 for Manitoba Rolling Mills, Figure 10 for Atlas Steel, Figures 13, 16, 20 and 23 for Algoma Steel and Figure 27 for U.S. Steel. In all cases the autoradiographs of the longitudinal and transverse sections from each strand have been positioned to conform with the curvature of the strand in and below the mold, and have been separated by a distance equivalent to the thickness of metal removed in the cutting process. All of the longitudinal sections have been sectioned perpendicular to the plane of curvature. The solid shell at the time radioactive gold was added to the liquid is clearly delineated in each strand as a white band on either side of each section. Between the two solid shells, the dark region results from the presence of radioactive gold in the billet. The dark regions surrounding each section are caused by exposing the film to light. The start of the solid shell in the longitudinal sections indicates the

Table VI. Steel Compositions

Test No.	Heat No.	Steel Composition										Ratio
		C	Mn	S	P	Si	Cu	Cr	Mo	Ni	Pb	Mn/S
W1	18084	0.31	1.11	0.05	0.04	0.15	0.35	0.17		0.21		22
W2	18140	0.35	0.67	0.025	0.02	0.10	0.24	0.13		0.17		27
M1,M2	62737	0.11-0.16	0.60-0.75	0.05	0.04	0.2-0.3	0.037					13
M3	52603	0.13-0.18	0.60-0.75	0.05	0.04	0.2-0.3	0.037					13
M4	52604	0.33-0.37	0.90-1.05	0.05	0.04	0.22-0.32	0.037					20
At1	26018	0.065	1.77	0.016	0.029	0.47	0.23	18.31	0.33	8.75	0.003	-
Aℓ1	8752A	0.21	1.17	0.032	0.018	0.24						37
Aℓ2	6257D	0.22	1.03	0.017	0.013	0.25						61
Aℓ3	8756A	0.20	0.92	0.028	0.013	0.34						33
Aℓ4	6256D	0.30	1.32	0.023	0.013	0.30						57
U1	KD3252	0.21-0.24	0.65-0.80	0.015	0.03	0.17-0.27	0.15	0.20	0.02	0.10		48

position of the meniscus when the gold was added to the liquid pool. Using this position as a reference, the top and the bottom of the mold are shown by horizontal lines. The inside radius of the strand is marked IR, the outside OR.

In the composite photographs the solid shell is observed to be sharply delineated at the solid-liquid interface in the mold indicating the mold liquid region is well mixed. Below the mold the shell becomes less distinct, accompanied by a marked increase in the apparent shell thickness due to incomplete mixing in the liquid pool.

In the upper part of the strands the middle of each section is depleted in gold. This is attributed to the dilution of the gold by the input stream, in agreement with previous observations [7]. The central depleted region usually extends to near the bottom of the mold. Also in the upper part of the strands in some tests, alternate light and dark bands (banding) indicating gold rich and gold depleted regions can be observed in the transverse section autoradiographs.

Below the mold the autoradiographs show the gold to be distributed in the form of an inverted cone. In most of the strands cast using a curved mold, more gold has deposited on the outside radius interface of the casting than on the inside radius interface (compare Test M3 in Figure 7 to test U1 in Figure 27). This behaviour is usually associated with buoyancy effects in the liquid, the high density gold falling further before being mixed in the liquid pool.

The depth of penetration of the radioactive gold is less than the pool depth indicated by the position of the tungsten pellet. The

depths of penetration of the pellet and the gold are given in Table V.

In some tests, fluctuations in shell thickness in the longitudinal sections in the upper mold region are observed (Figure 8(a) and (b)). A closer examination of the fluctuations reveals that usually there is a depression (or ripple mark) in the surface of the billet wherever there is a decrease in shell thickness. In addition a small amount of solid shell can be observed above the position of the meniscus in Figure 8(b). This indicates that a small segment of the shell has stuck to the mold wall and been torn from the shell when the mold moves upward. These fluctuations have been observed in tests using a flux lubricant and on tests using rapeseed oil lubricant in the mold. In general, the fluctuations are small and tend to disappear by the time the strand leaves the mold.

The autoradiographs of the transverse sections indicate that there is no significant difference in average shell thickness along the face centres in the molds in any of the tests. However, in several of the tests on the blooms and billets, appreciable thinning of the solid shell at the corners (re-entrant corners) was observed.

The average shell thickness in the mold has been measured for all the tests and compared to calculations of shell thickness based on heat transfer considerations. These results are reported in a later section.

The cast structure in most of the strands consists of columnar grains growing from the outside surface in a direction perpendicular to the outside faces and an equiaxed dendritic structure in the central

region of the casting. A displacement of the casting centreline from the geometric centre of the strand is observed in strands cast using curved molds. In these strands the equiaxed zone is displaced toward the outside radius, resulting in the zone adjacent to the inside radius being nearly entirely columnar and a shortened columnar zone adjacent to the outside radius. In strands cast using vertical molds no shift in the centreline of the casting was observed.

In equiaxed zones of the castings some dendritic bridging of the central region with solute rich liquid filling the cavities below the bridging points is observed. Macrosegregation, taking the form of V shaped segregation, is also evident in some cases.

Extensive interdendritic radial cracking is observed in strands which have a Mn/S ratio less than 50 (see Table VI). The cracks are filled with liquid enriched with gold and sulphur (since they appear as dark lines in the autoradiographs and sulphur prints), and are not observed on the machined surfaces. All the alloying elements which have a segregation coefficient less than unity in iron (sulphur, phosphorus, carbon, etc.) will also be enriched in the liquid filling the cracks, producing compositional inhomogenieties in the strand which can only be reduced by solid state diffusion. Intergranular centreline cracking, the cracks being filled with solute rich liquid, was also observed in some strands.

Small dark spots can be observed in a number of the autoradiographs; many of the spots can be directly related to sulphur rich spots in a sulphur print of the same surface. These spots have been found to be clumps of manganese sulphide inclusions, approximately 100 to 500μ in diameter, by electron probe microanalysis[34]. The small dark areas tend to

Table VII. Casting Characteristics from Autoradiographs.

Test No.	Depth of Penetration by Input Stream (cm)	Mn/S Ratio	Casting Size (cm^2)	Banding	Shell Tearing at Meniscus	Re-entrant Corners	Radial Cracking	Centreline Cracking
M1	90	13	13.3x13.3	X	X		X	
M2	90	13	13.3x13.3	X	X		X	
M3	70	13	10.1x10.1	X	X			
M4	70	20	10.1x10.1	X	X	X		
At1	100	-	12.7_x109	X		X		
Aℓ1	90	37	843	X	X		X	
Aℓ2	50	61	1015	X				X
Aℓ3	120	33	22.9x26.7	X		X		
Aℓ4	50	57	22.9x26.7	X	X	X		X
U1	110	48	19x19	X	X	X	X	

be concentrated in a band parallel to the inside radius surface in the curved castings.

Table VII gives a summary of the tests in which some of these defects in the casting were observed.

4.1.2. Specific Observations; Manitoba Rolling Mills

In all four tests the shell thickness in the longitudinal sections in the mold were observed to fluctuate appreciably. Note in section D of Test M2 (IR)(Figure 7) the shell is about half the average shell thickness just before the billet leaves the mold. The frequency of the fluctuations do not appear to be periodic and cannot be directly related to mold oscillations. In Figure 8(a) a depression at the surface of the billet is shown wherever there is a decrease in shell thickness. In addition in section 1A, Figure 8(b), a small segment of the solid shell can be observed above the meniscus.

Variations in shell thickness across the billet in Tests M2 and M4 are shown in Figures 9(a) and 9(b) respectively. Also in Figure 9(b), Test M4, an appreciable thinning of the lower corners is observed.

In Tests M1 and M2 the centrelines of the castings are displaced towards the lower radius surface by 0.3 cm. from the geometric centre. The columnar structure extends 4.4 cm. in from the inside radius and 2.5 cm. in from the outside radius surface.

Some centreline porosity was observed on the machined surface of the billets for Tests M1 and M2, and in the autoradiographs (see Figure 7, section 2G). Gold rich central regions with periodic bridging

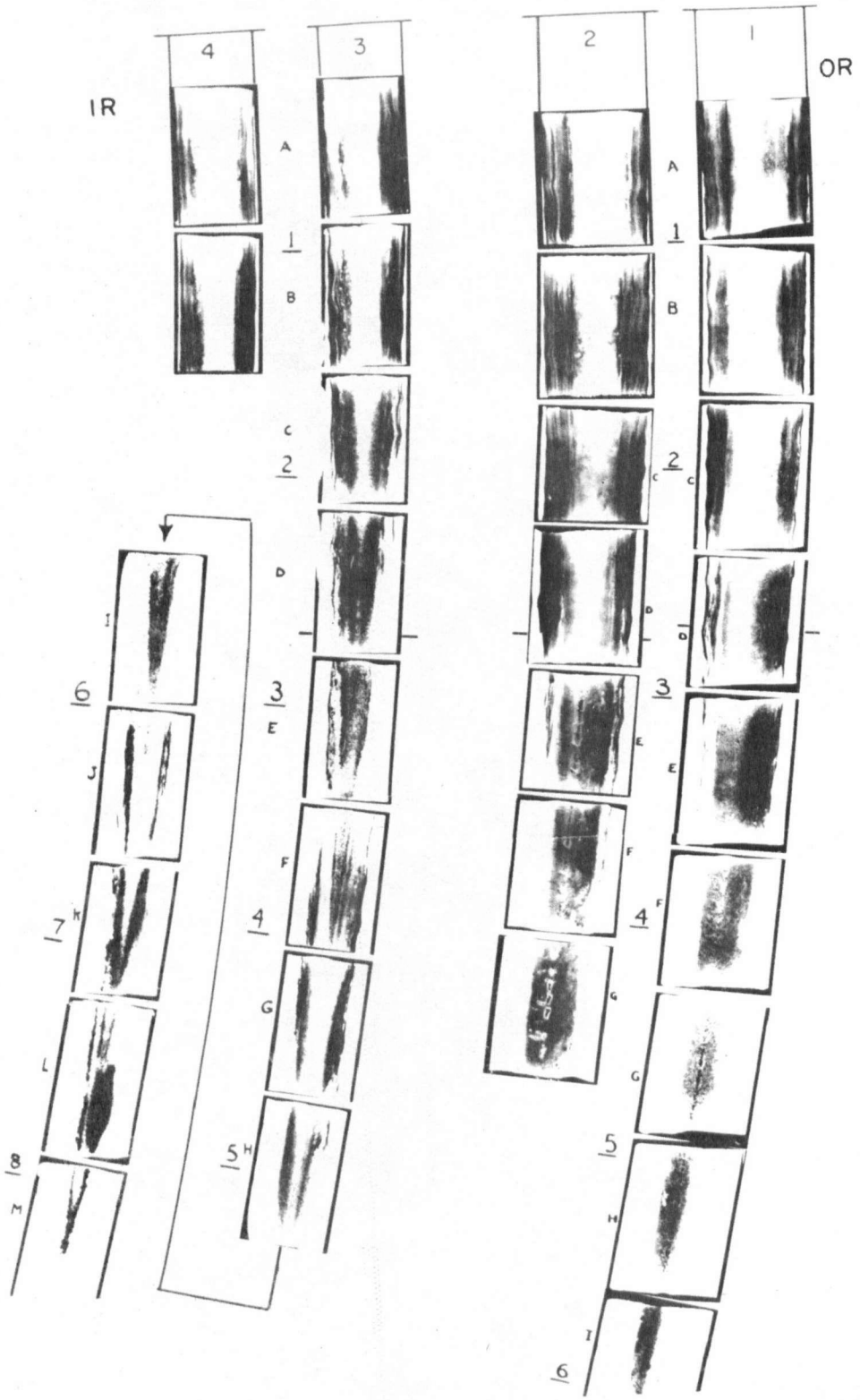

Figure 7. Autoradiographs of longitudinal sections of test strands M1 to M4, cast at Manitoba Rolling Mills.

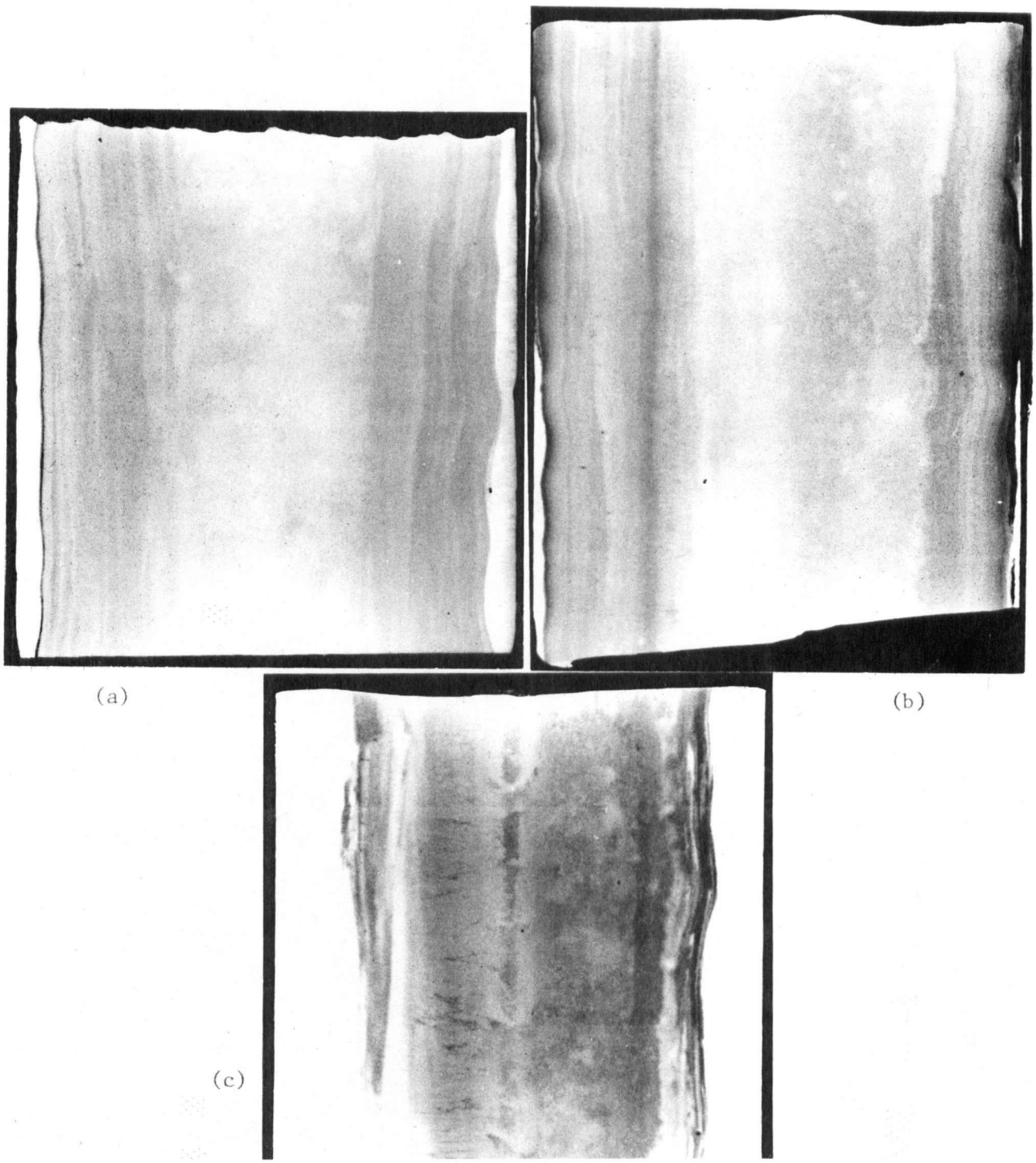

Figure 8. (a) Section 2C of Figure 7, showing thin regions of the shell and associated depressions in the outer billet surface.
(b) Section 1A of Figure 7, showing solid shell segment above meniscus.
(c) Section 2E of Figure 7, showing gold rich central region with periodic bridging across the centreline by large dendrites.

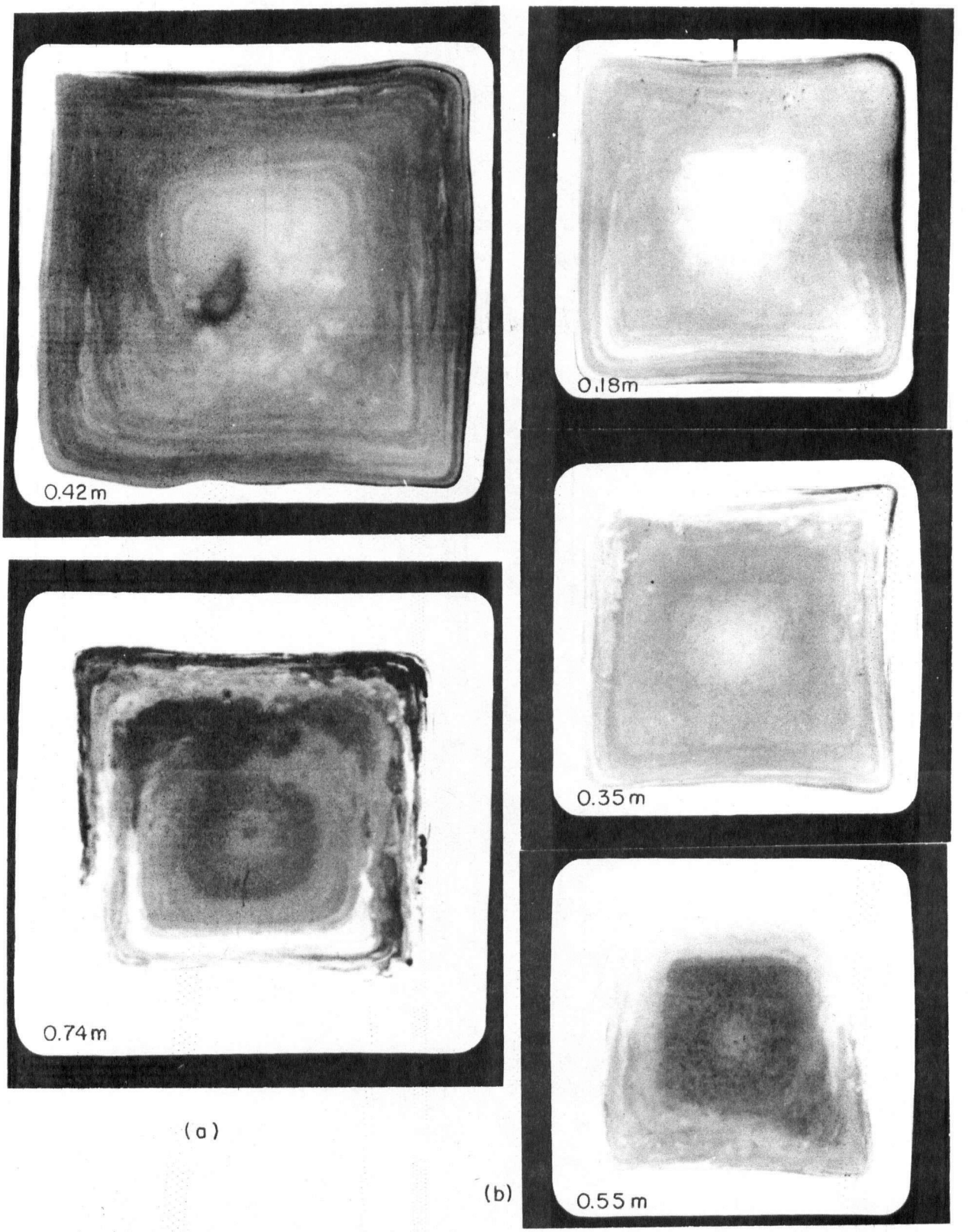

Figure 9. Autoradiographs of transverse sections of strands at positions indicated below meniscus. (a) strand M2, (b) strand M4.

across the centreline by large dendrites is shown in Figure 8(c).

In Tests M3 and M4 (10.1 cm. billets) the bulk of the cast structure consists of small dendritic grains. There is no apparent columnar region or centreline shift.

Extensive radial cracking was observed in the inside radius half of the billets in Tests M1 and M2 (see Figure 8(c)). Clumps of sulphide inclusions in the inside radius half were also observed.

4.1.3. Atlas Steel

The solid-liquid interface in the mold is smooth and regular with no significant thickness fluctuations. A closer examination of the shell in section C2, Figure 11, indicates the interface breaks down to a dark line separated from the general dark area by a thin gold free region. Moving down the slab, the dark line terminates, resulting in a local apparent increase in the shell thickness. This effect is attributed to the flow pattern in the liquid pool. Some thinning of the solid shell is observed near the outside corner of series L (Figure 10). The round clear region in the lower left corner of section 3L is the outline of the corner marker placed in this position when the gold was added to the liquid pool.

The fluid flow pattern in the liquid pool, based on the gold distribution shown in Figure 10 is complex. (a) A dark line is observed to be present around part or all of the periphery of the sections in series L and R, associated with the first stream of gold rich liquid which washes the solid-liquid interface and was frozen in. In series L, section 1, 2, and 3 have a dark band around the entire periphery of the section. Sections 4 to 7 have a dark line around the end of the slab and partly up

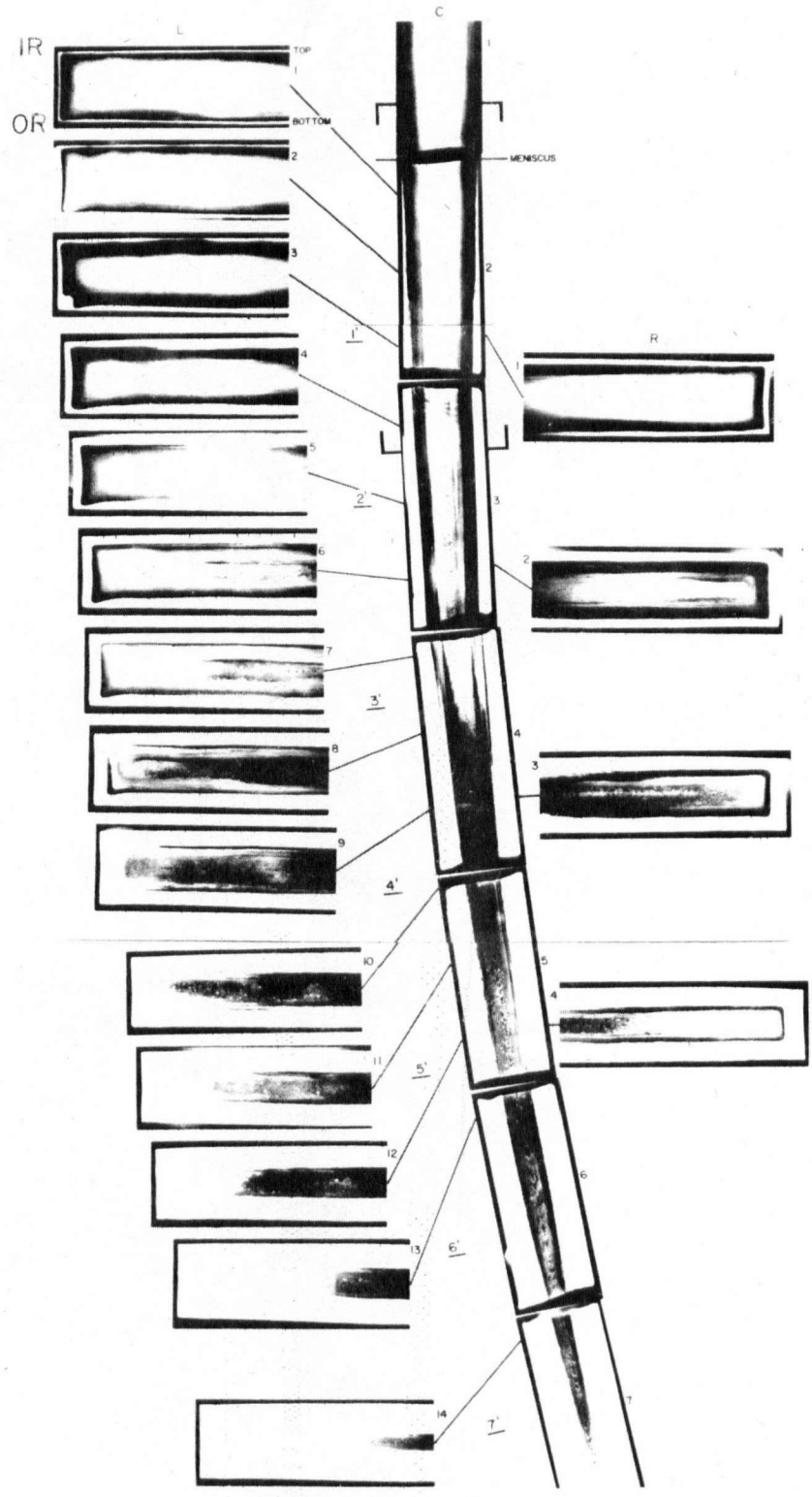

Figure 10. Autoradiographs of longitudinal and transverse sections of stainless steel slab, Test At1. The positions of the transverse sections with respect to the meniscus are indicated.

the side, extending further toward the middle on the top side. In section 9 and below, there is no dark line at the slab ends; dark lines are present in section 9 on the large faces in the central part of the slab. (b) Adjacent to the solid-liquid interface in the liquid pool, the gold is distributed in a series of bands, approximately 0.4 cm. wide. The edge of each band appears to correspond to the trace of the solid-liquid interface. The bands are most clearly delineated in sections L2 to L7, C2 and C3. (c) The activity in the slab, both above and below the meniscus at the time of addition of the gold, was measured with a geiger counter before the slab was sectioned. The results are shown in Figure 12, in which the activity relative to the activity at the meniscus at the edge, is plotted as a function of position along the slab for the edge, 15 cm. from the edge, and along the middle of the slab face. The figure shows that the distribution of gold above the meniscus is very similar to that below the meniscus, even though the mode of distribution of the gold must be markedly different in both regions. At the meniscus the activity is higher at the edge; below the meniscus the three sets of measurements essentially coincide; above the meniscus the activity is highest at the centre.

The cast structure in the slab consists of columnar grains with a relatively narrow band of equiaxed grains in the centre. In some sections (L8 to L10) small gold free spots with an apparent dendritic structure were observed in the central part of the slab. Relatively dark structureless spots were also observed.

The centerline of the strand consists of a coarse dendritic structure separated by gold rich regions. The dendritic structure along the centreline of the transverse sections becomes less distinct and then

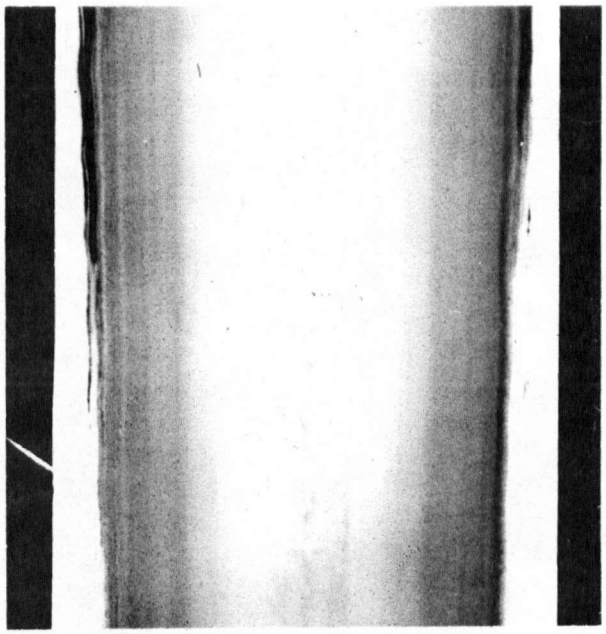

Figure 11. Section 2C of Figure 10, showing discontinuity in shell thickness. Top of autoradiograph 15.7 cm. below meniscus.

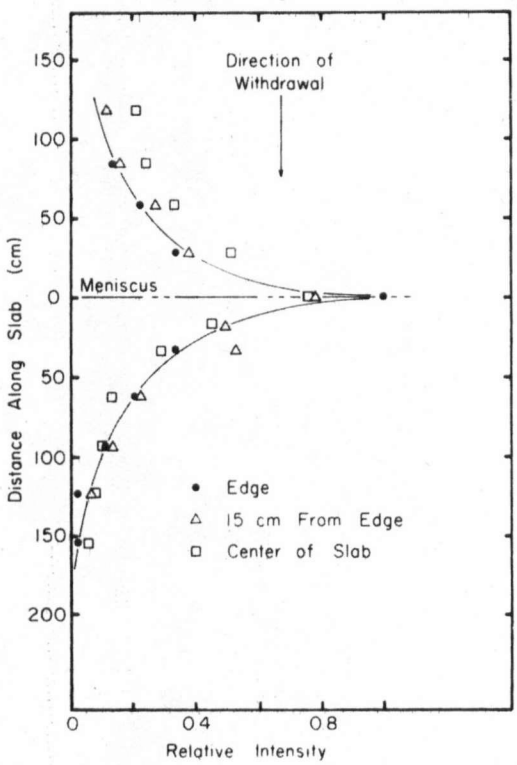

Figure 12. Distribution of radioactive gold in the stainless steel slab prior to sectioning.

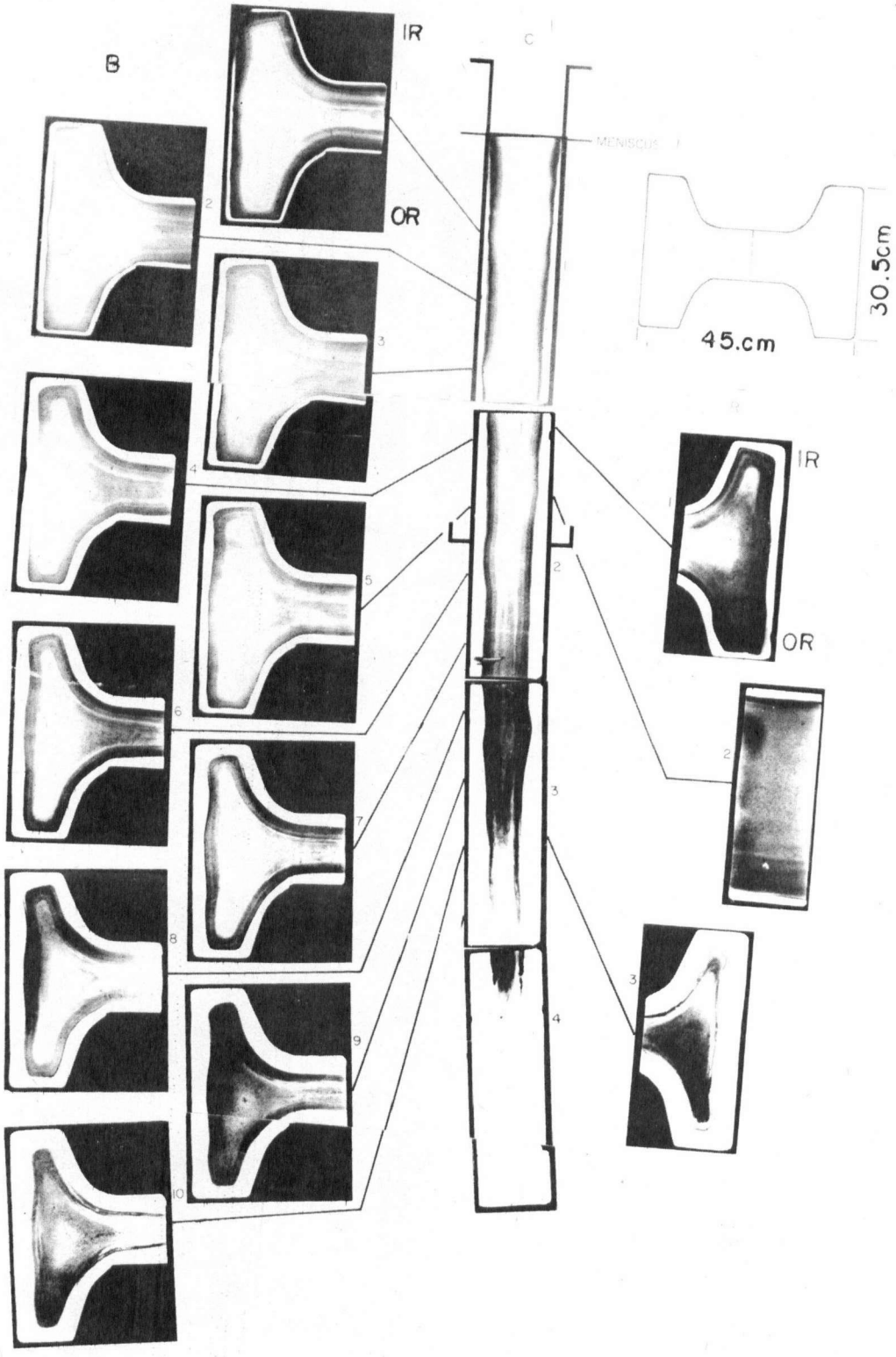

Figure 13. Composite of autoradiographs of beam blank A, Test A&1 showing the pool profile down the web (C) and perpendicular to the longitudinal axis (B and R).

disappears, moving from the middle to the end face of the slab.

4.1.4. Algoma Steel

4.1.4.1. Beam Blanks

The radioactive gold was well mixed in the liquid pool in the A profile beam blank, outlining the solid shell to about 107 cm. below the meniscus (Figure 13). At the meniscus in section C1, small sections of the shell were observed to be present 2.5 to 3.2 cm. above the continuous shell. Below the meniscus the shell thickness fluctuates periodically, the distance between fluctuations being 3.2 cm. Note that the break in the shell in section C2 is an artifact associated with the flame cutting operation. Further below the meniscus (C1, C2, C3) there are fluctuations in shell thickness of much greater magnitude than those associated with tearing. These fluctuations correspond to a thinning of the shell in the web area of the transverse sections B3, B6, and B8.

In sections B1 to B5, localized thinning of the shell can be observed near the centre of the flange face. This is attributed to a 1.5 cm. spacer placed between the two mold halves resulting in poor thermal contact between the strand and the mold. Note the dark area in the corner of B1 is an artifact due to local overexposure of the film to light.

Deformation of the solid shell in the web fillet area, flange face and flange tip of the beam blank is seen in Figure 14(a).

The central line of the cast structure is observed to be displaced 0.2 cm. from the geometric centre of the beam blank to the outside radius, the columnar zone extending in the web 3.3.cm. in from

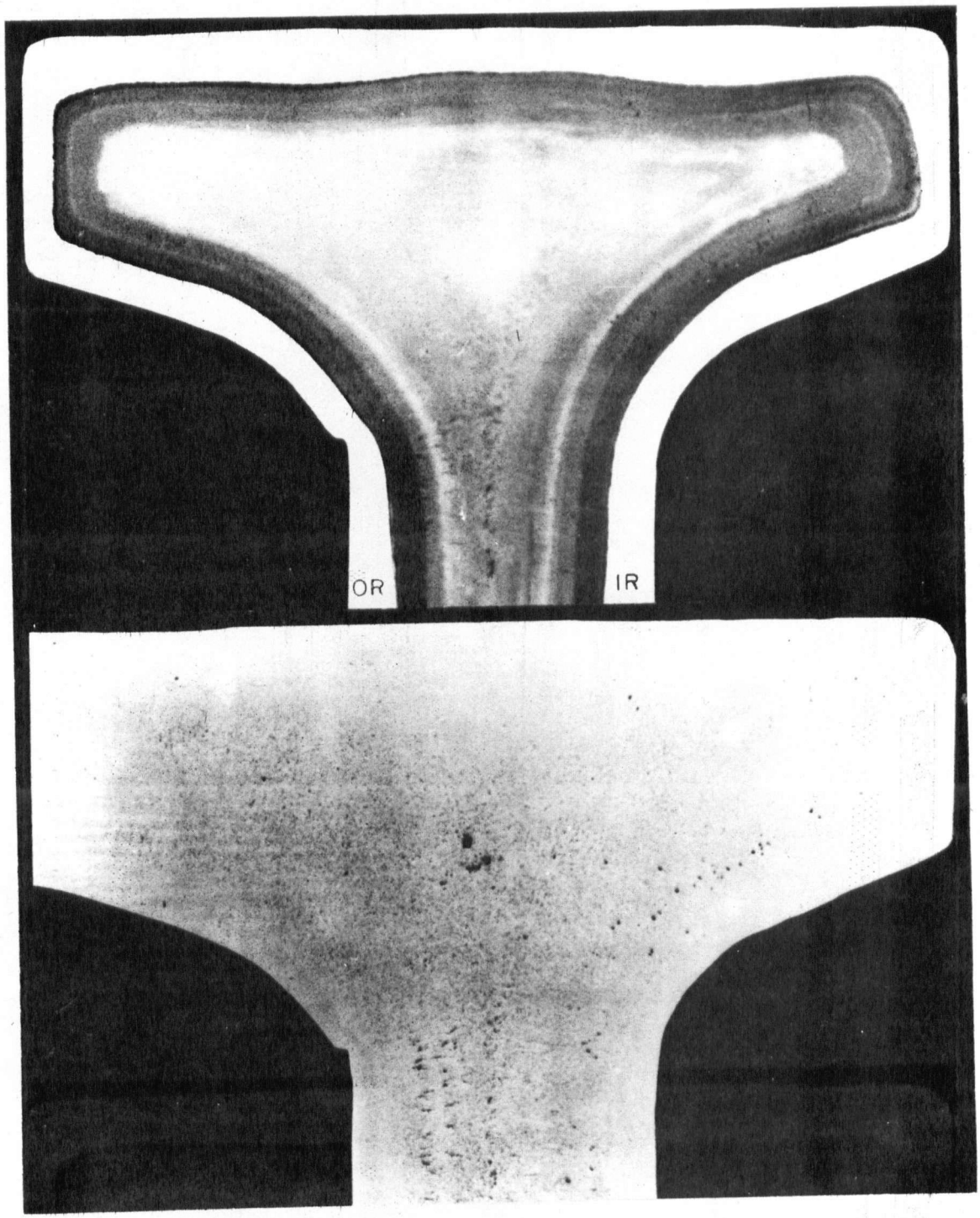

Figure 14. (a) Autoradiograph B6 of Figure 13.
(b) Sulphur print of same surface as in (a).

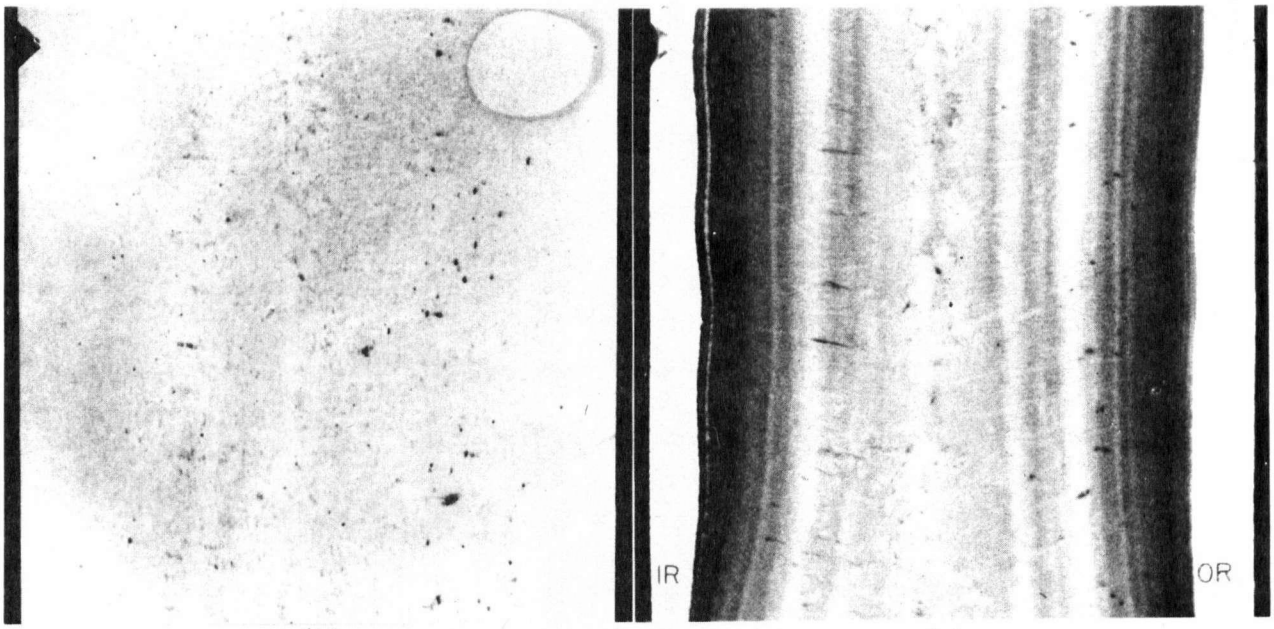

Figure 15. (a) Autoradiograph of central portion of C1, Figure 13. (b) Sulphur print of same surface as in (a).. Note that the circle is an artifact and is not significant.

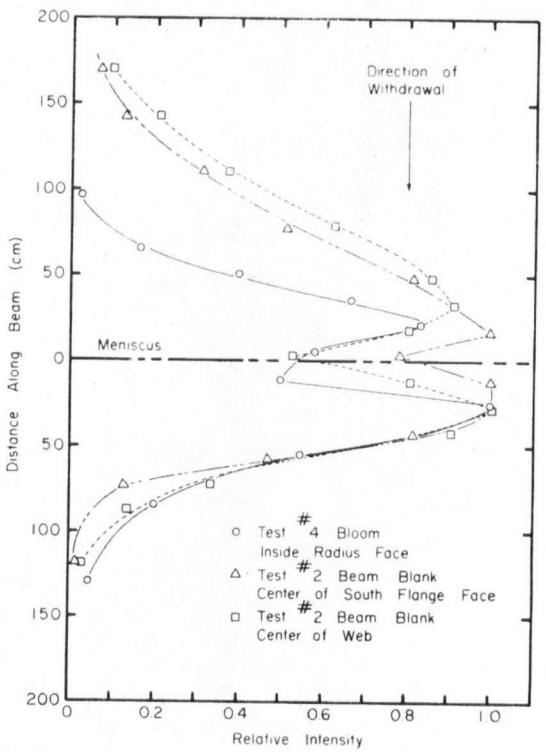

Figure 17. Distribution of radioactive gold in E beam blank and Test A&4 bloom.

the outside radius and 4.8 cm. in from the inside radius.

Small radial cracks (Figures 14 and 15) were observed in all the specimens autoradiographed. They tended to be in a region (a) 2.6 to 3.6 cm. from the outside radius surface in the web (b) 1.7 to 3.6 cm. in from the outside radius surface in the web fillet and (c) 1.9 to 3.3 cm. in from the flange surface near the inside radius of the flange tip. No centreline porosity or cracking was observed in the strand.

Clumps of inclusions forming a band parallel to the inside radius surface can be seen in Figure 14(a) and (b). Also inclusions are evident throughout the web (Figures 15(a) and (b)), some at positions relatively close to the outer surface where little solute segregation between the fine columnar dendrites would occur.

In the E profile beam blank (Figure 16) the solid shell is sharply delineated to about 65 cm. below the meniscus. Less mixing of the gold in the liquid pool occurred in this test than in the A beam blank.

Prior to sectioning, the distribution of gold in the casting was measured with a geiger counter along the web and flange faces. The results of which are shown in Figure 17.

Shell thickness variations accompanied by surface ripple marks and tearing at the meniscus were observed in the longitudinal sections in series E, Figure 16. The fluctuations and ripple marks were spaced at approximately 3.1 cm. intervals.

In the transverse sections of the strand, it is evident that

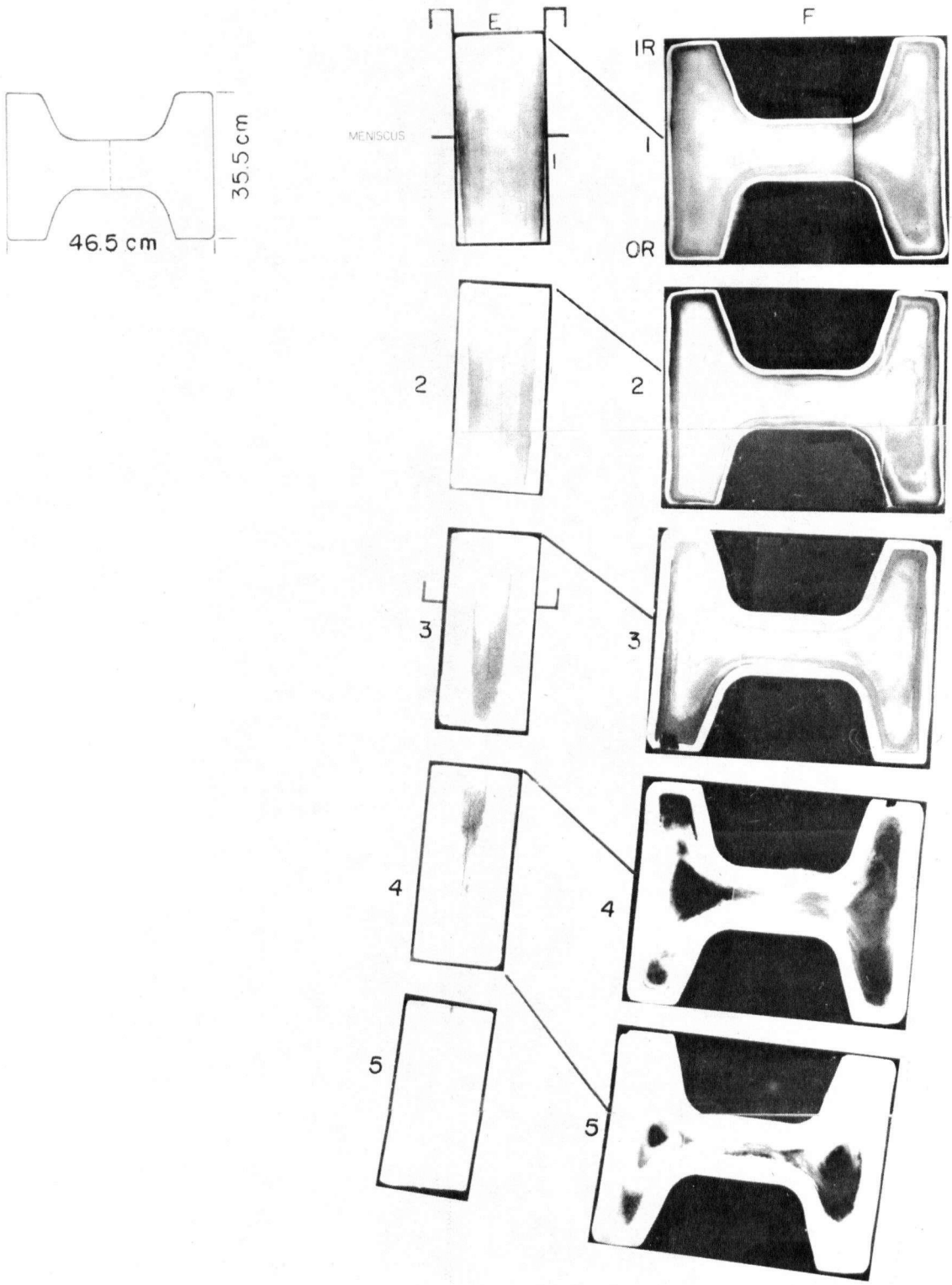

Figure 16. Composite of autoradiographs of beam blank E showing the pool profile down the web (E) and perpendicular to the longitudinal axis (F).

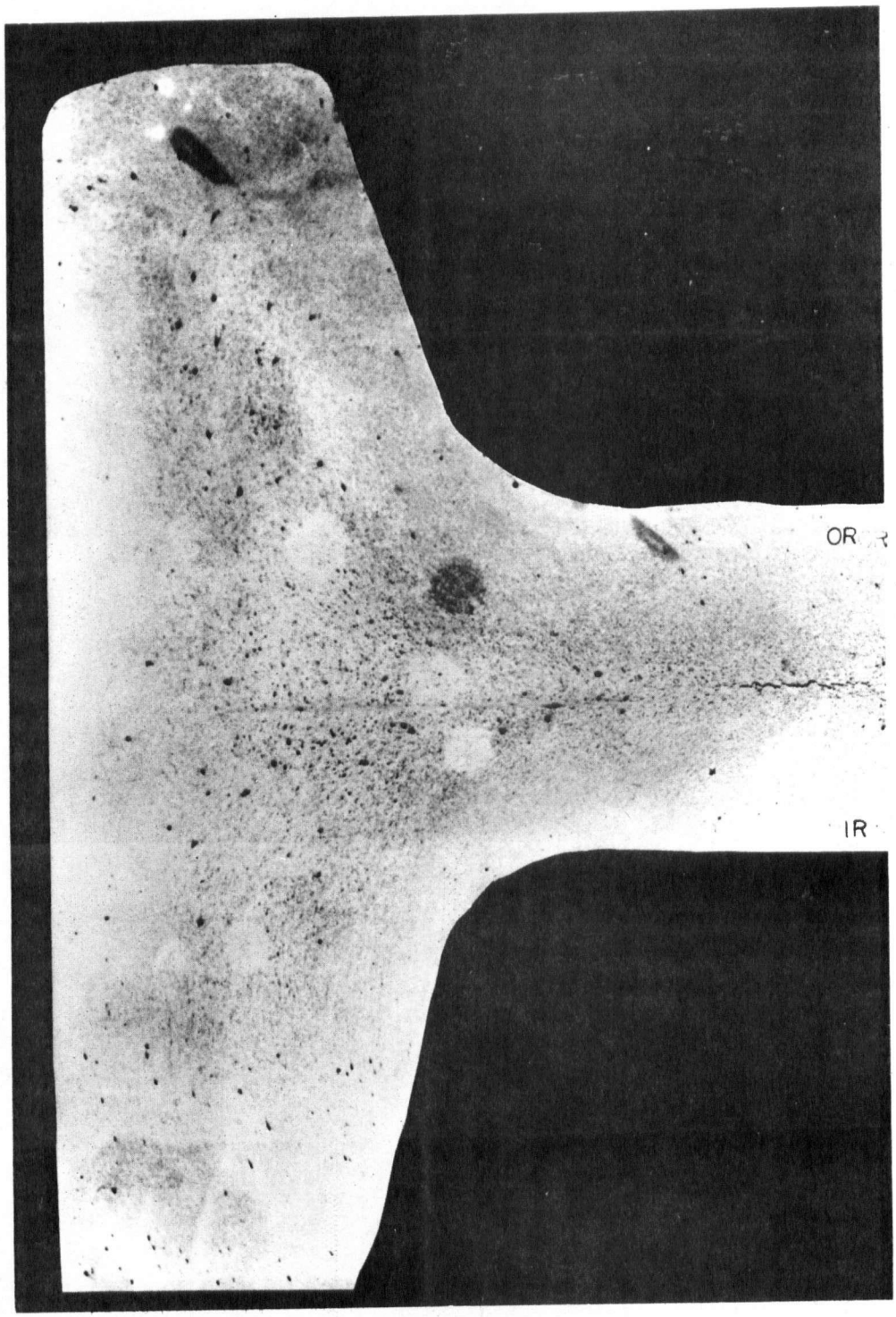

Figure 18. Sulphur print of section F4, Figure 16 showing clumps of sulphide inclusions and centreline cracking.

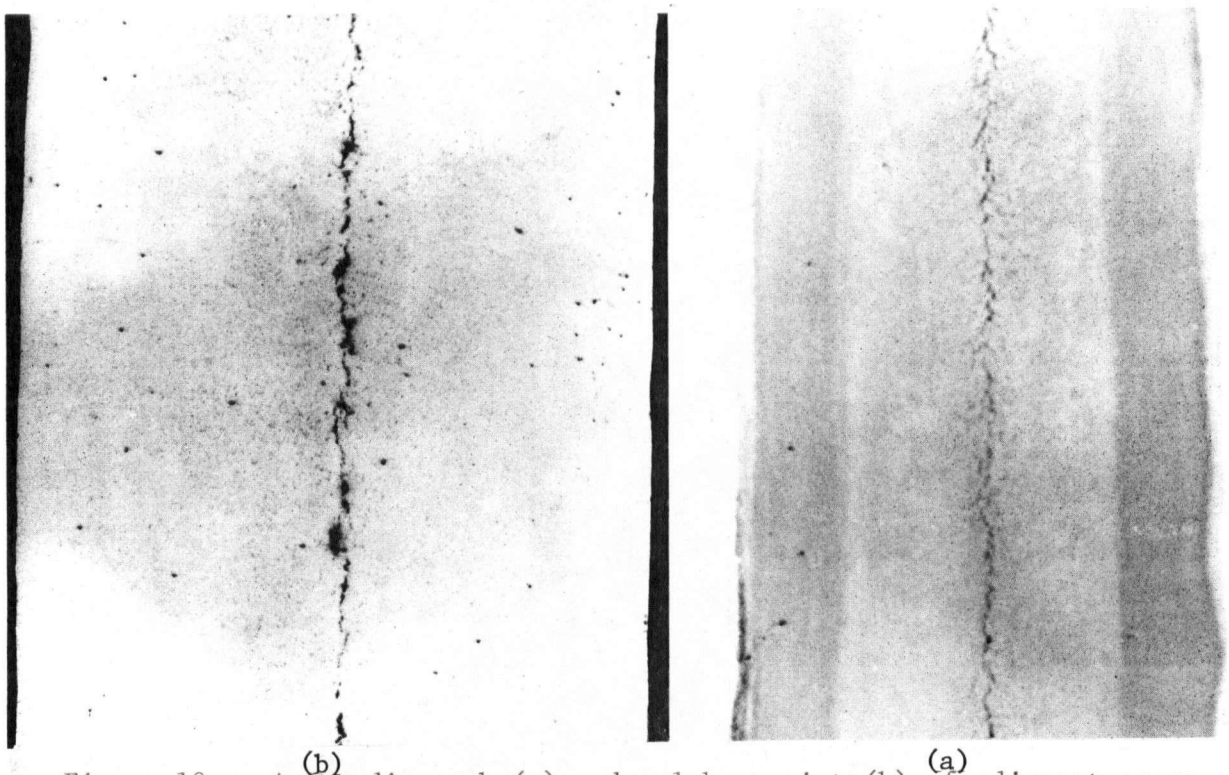

Figure 19. Autoradiograph (a) and sulphur print (b) of adjacent areas of E2, Figure 16 showing clumps of sulphide inclusions and solute enriched centreline cracks.

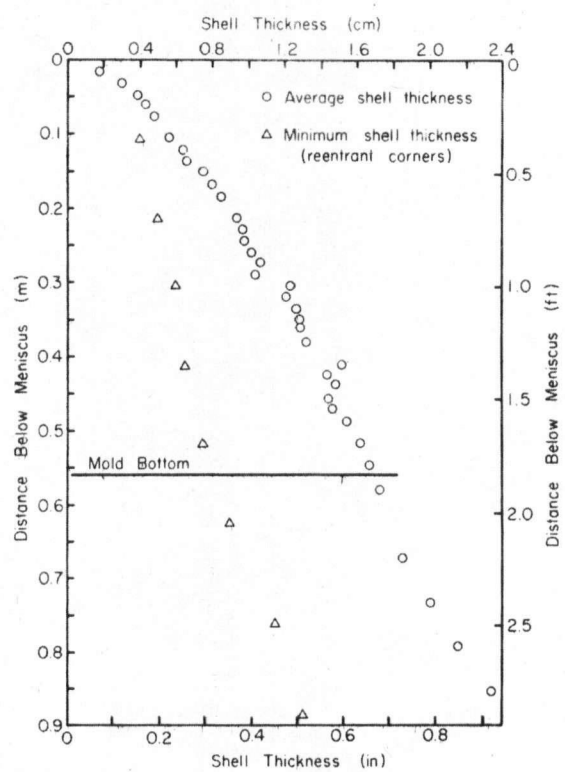

Figure 21. Shell corner and average shell thickness as a function of distance below meniscus.

the shell thickness is highly uniform around the periphery of the beam. Note that the shell sections missing in the flange of F3 and F4 are artifacts due to cutting.

Although there was no evidence of radial cracking in the beam blank, extensive intergranular cracking occurred along the central plane of the web in all of the sections examined. The cracking is evident in the web in Figure 18 and in the autoradiograph and sulphur print in Figure 19.

In Figure 18 the sulphur print of the transverse section shows a much higher density of inclusions than observed previously, most of which are uniformly distributed throughout the beam.

4.1.4.2. Blooms

The extent of mixing of the radioactive gold in the two tests done on the blooms is markedly different. In the first test, Aℓ3 (Figure 20), open teeming was used between the tundish and the mold resulting in a sharply outlined interface for a distance of 180 and 135 cm. below the meniscus for the outside radius and the inside radius interfaces respectively. In the second test, Aℓ4 (Figure 23), a submerged entry shroud was used in the tundish resulting in a penetration of gold in the liquid pool half that in Test Aℓ3. The graph in Figure 17 shows that with the shroud, there was an equal distribution of gold above and below the meniscus, with a decrease in intensity at the meniscus. Also very little mixing of the gold occurred in the lower parts of the pool. Preferential flow down the outside radius is evident in sections L5, 6, and 7.

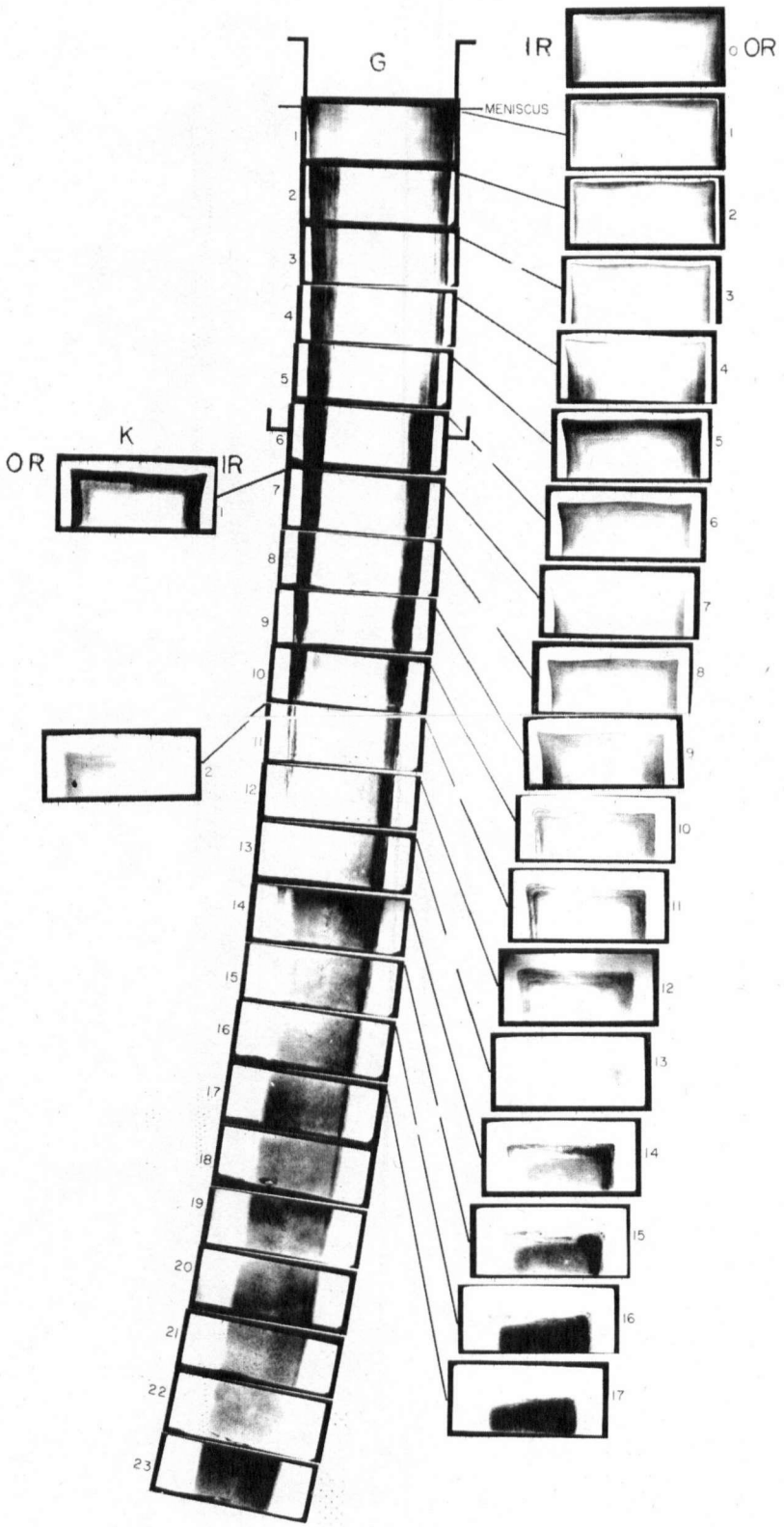

Figure 20. Composite of autoradiographs of bloom, Test Aℓ3, showing the pool profile down the strand (G) and perpendicular to the strand axis (H,K).

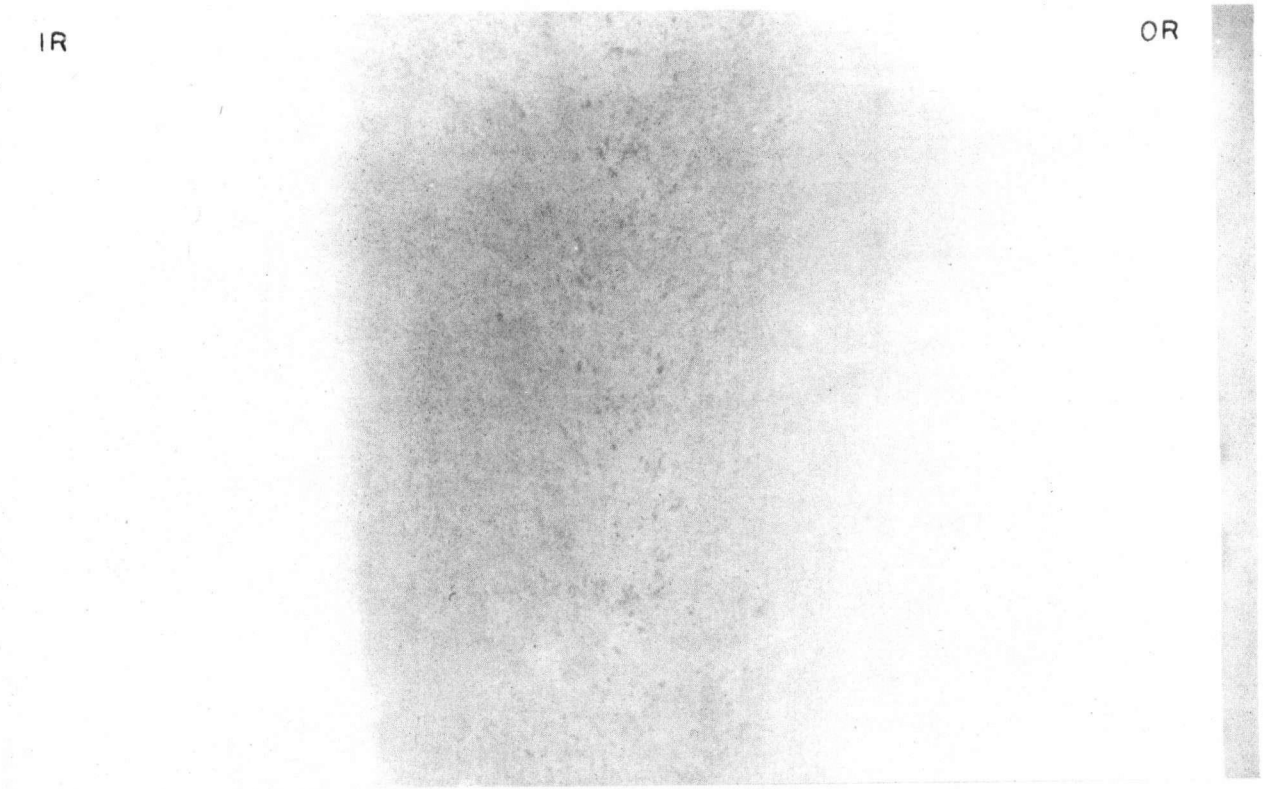

(a)

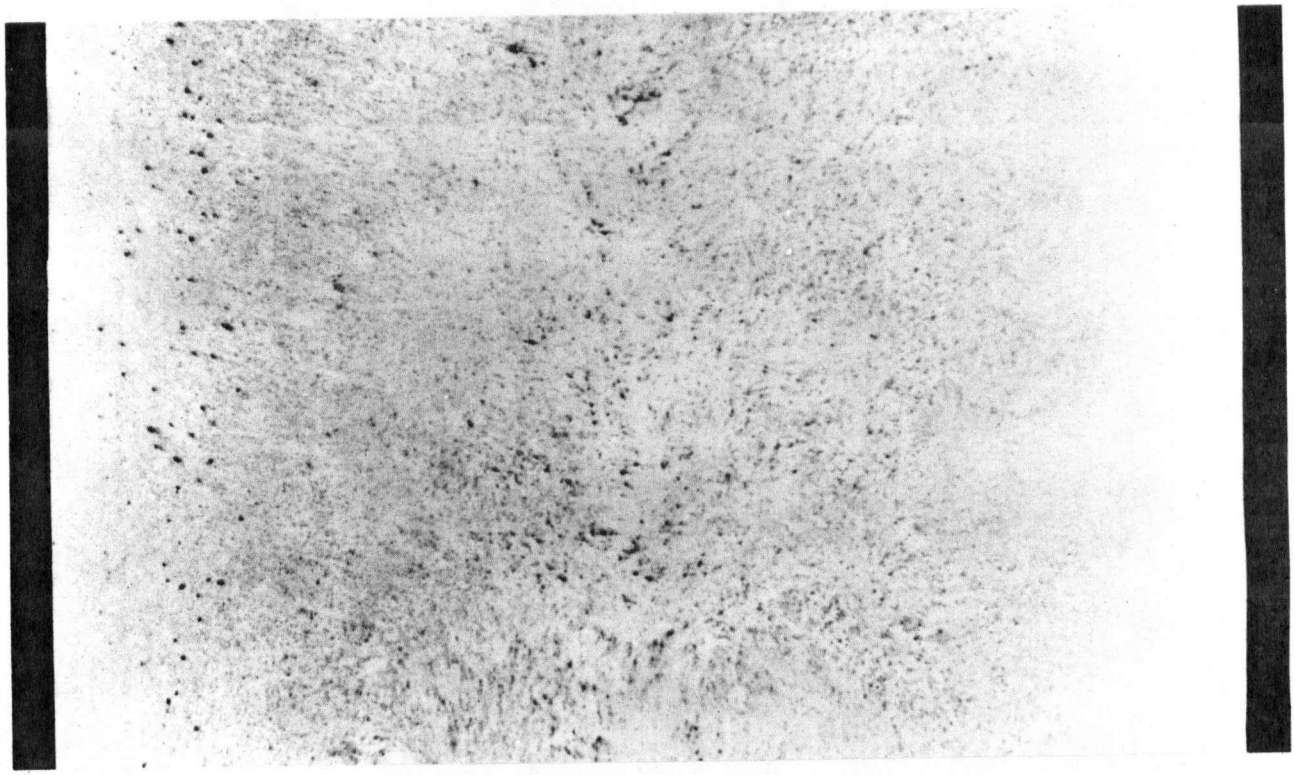

(b)

Figure 22. (a) Autoradiograph G25 in Figure 20.
(b) Sulphur print of same area as (a).

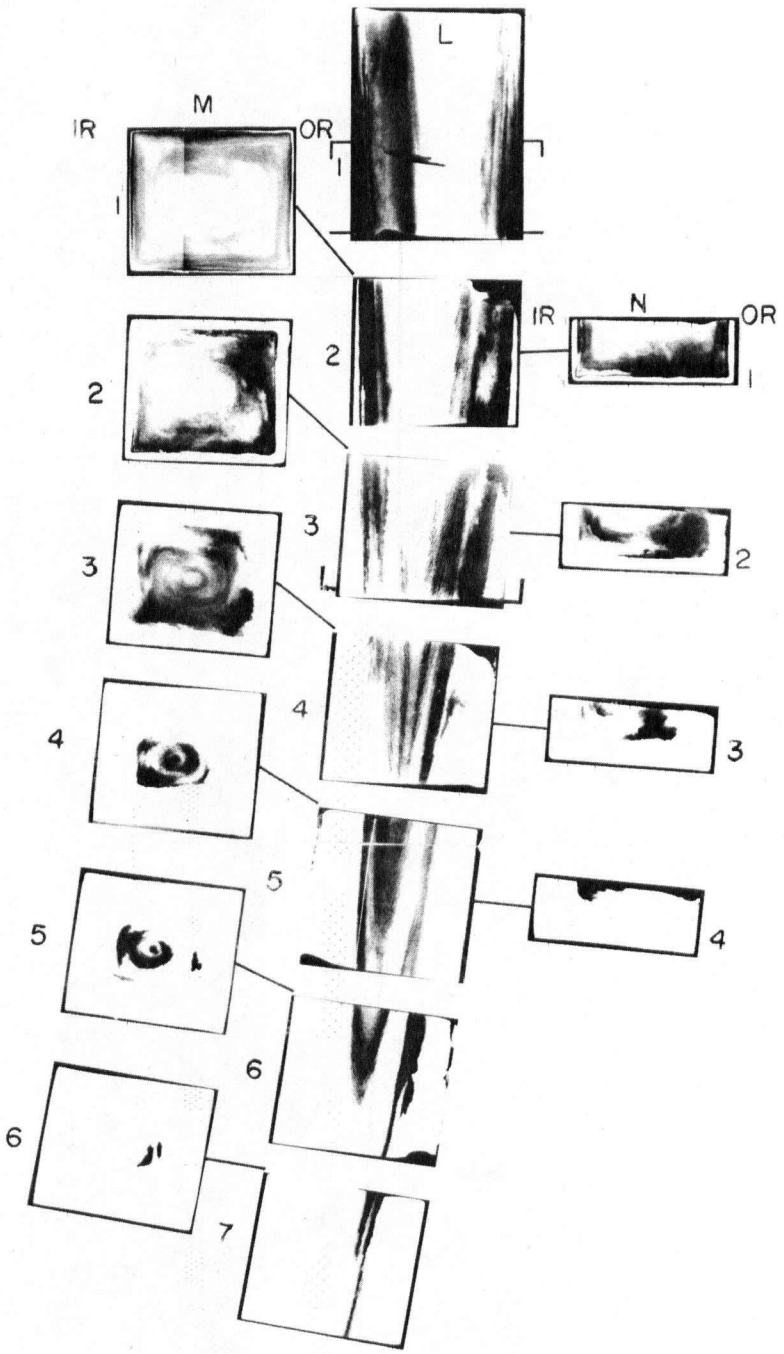

Figure 23. Composite of autoradiographs of bloom, Test Aℓ4, showing the pool profile down the strand (L) and perpendicular to the strand axis (M,N).

In Test Aℓ3, the solid shell in the vertical sections appear to be even and regular with no significant fluctuations in thickness. In the transverse sections re-entrant corners can be observed on the inside radius, the corners remaining thin at about half the shell thickness at the centre (Figure 21).

In Test Aℓ4, there is evidence of tearing occurring at the meniscus (section L1). Surface ripple marks at 3.5 cm. intervals correspond to shell fluctuations in longitudinal sections. In the mold region the shell is reasonably uniform in thickness (irregular shape in L3 and L4 due to incomplete mixing of gold in the liquid pool). In this test it was noted that the submerged shroud was off centre, tending to point to the south-outside radius corner. The misalignment of the shroud had no observable effect on the shell thickness around the periphery of the bloom. Re-entrant corners with corresponding corner cracking were observed on the inside radius corners, the corner crack being filled with gold and sulphur rich material (Figure 24(a) and (b)).

In the open pour bloom the columnar structure extended 10 cm. and 6.3 cm. in from the inside and outside radius surface respectfully. Macrosegregation, taking the form of V shaped segregation, is evident, but not marked. No radial or centreline cracking was observed in any of the sections, nor was there any centreline porosity. Large clumps of sulphide inclusions are concentrated in a band 2.3 cm. from the inside radius surface as shown in Figure 22(b). Sulphur rich areas are also present in the centre of the bloom which can be directly related to gold rich areas in Figure 22(a).

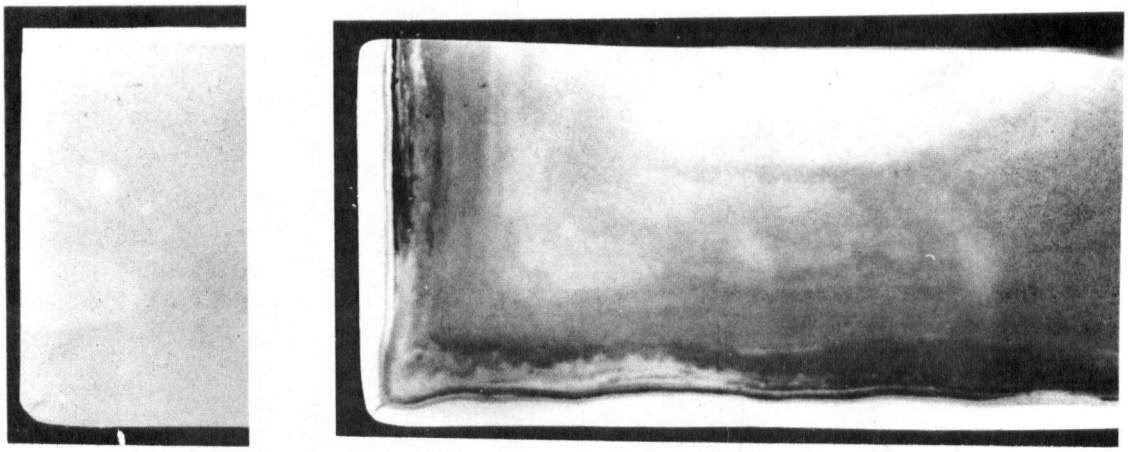

Figure 24. Autoradiograph (a) and sulphur print (b) of section N1, Figure 23 showing corner crack filled with gold and sulphur rich material at A.

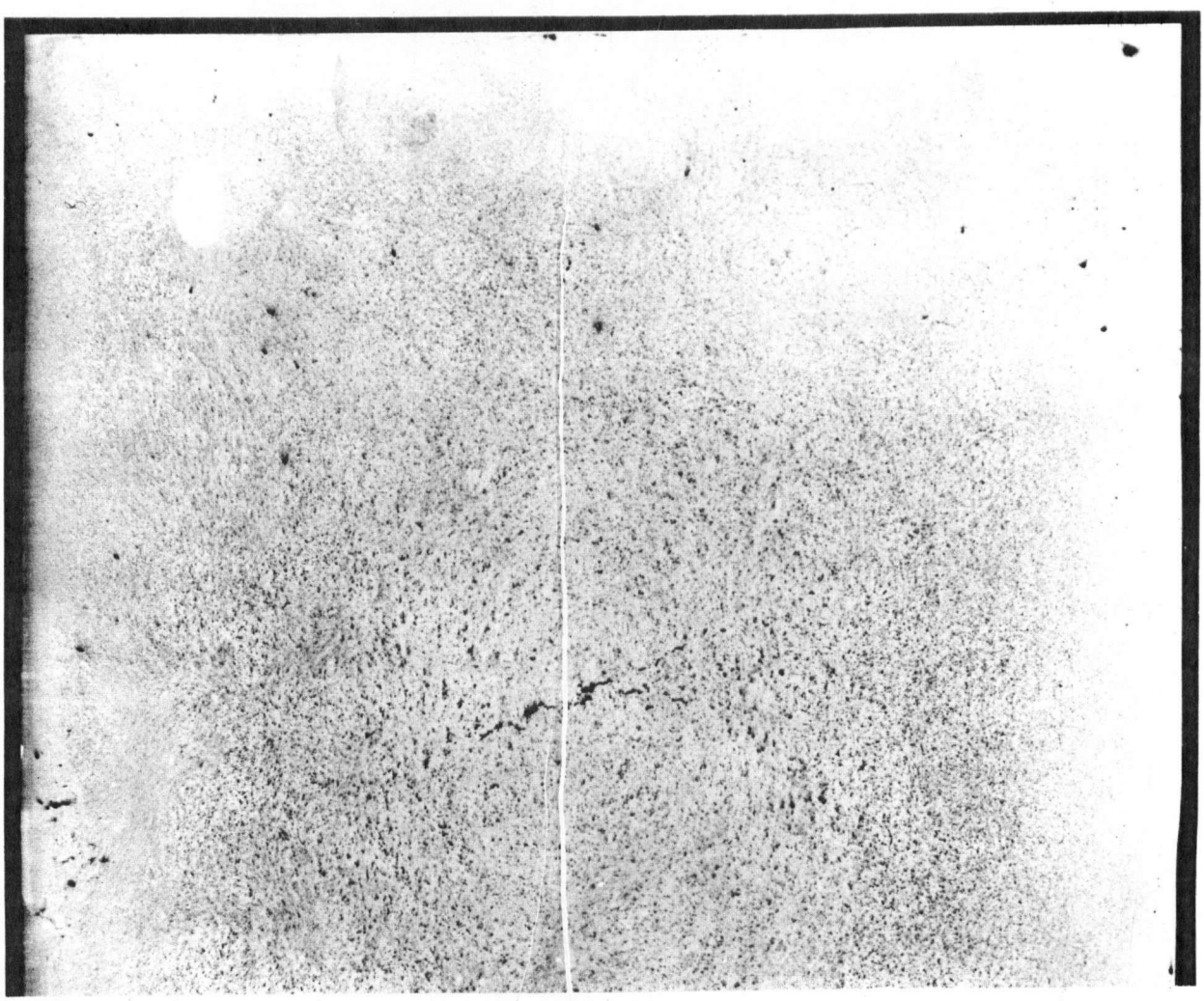

Figure 26. Sulphur print of section M5, Figure 23 showing centreline intergranular cracks filled with sulphur rich residual liquid.

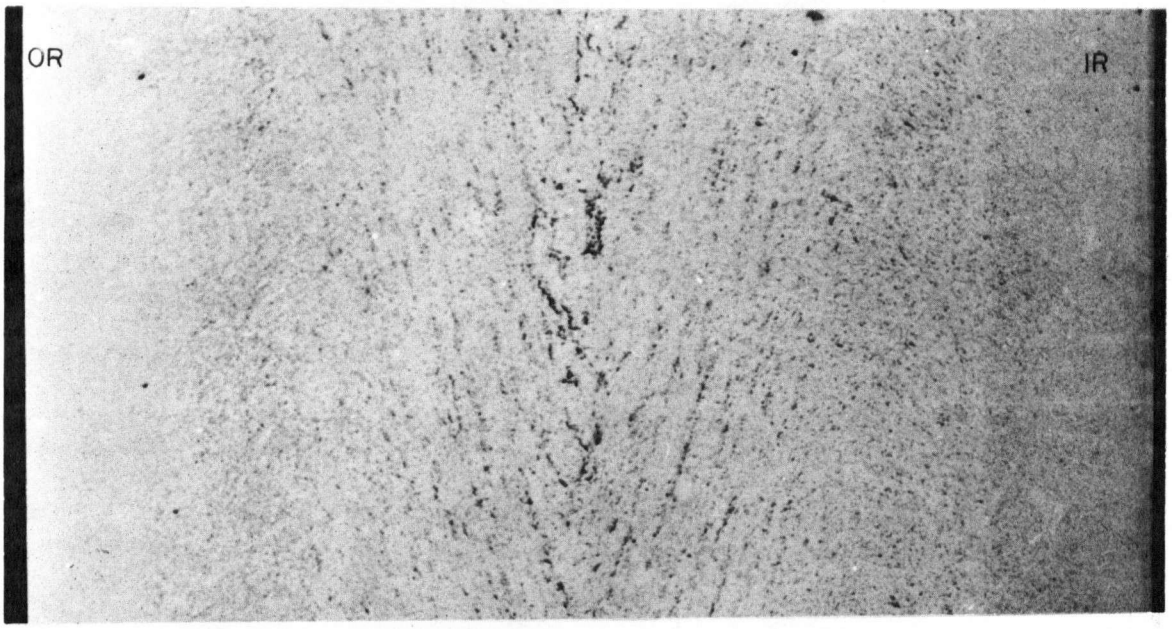

Figure 25. Sulphur print of part of section L1, Figure 23 showing V segregate pattern.

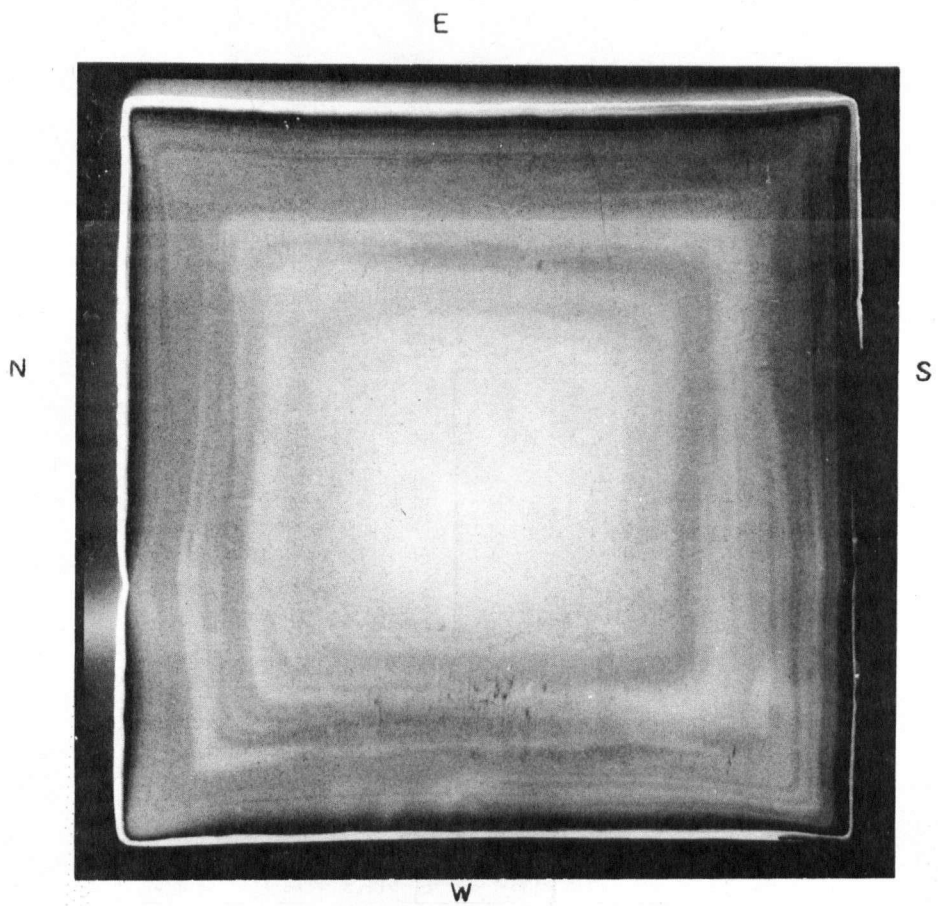

Figure 28. Section B2 of Figure 27, showing shell separation at the corner.

In the test using the submerged shroud the major part of the bloom consisted of cored, dendritic, equiaxed grains with no resolvable columnar zone. Macrosegregation of the gold and sulphur were observed, particularly in sections L1 (Figure 25) and M5 (Figure 26), in the form of V shaped pipes. Again no evidence of radial cracking was observed but some centreline cracking did occur, as shown in the sulphur print of M5. The centreline cracks are intergranular and intermittent, occurring in some sections and not others. No significant numbers of large sulphide inclusions were observed.

4.1.5. U.S. Steel

In section A2, Figure 27, it is evident that the solid shell starts much lower on the South side than on the North side. The transverse section, B2, also shows a solid shell on the North side and a partial shell on the South. Note that in the Southwest corner of B2, Figure 28, some radioactive gold has entered behind the solid shell for about 2 cm. from the corner suggesting shell separation at the corner has already occurred.

Variations in shell thickness in the longitudinal sections A2 and A3 and re-entrant corners in the transverse sections B3 to B6 were observed. The fluctuations in the longitudinal sections are small and are comparable to those that occur in Test Aℓ4.

The cast structure consists of a highly regular columnar zone, to about 5.5 cm. from the outside surface, and a cored dendritic equiaxed zone. In the columnar zone the primary dendrite spacing was measured as a function of distance from the outside surface. The results of these

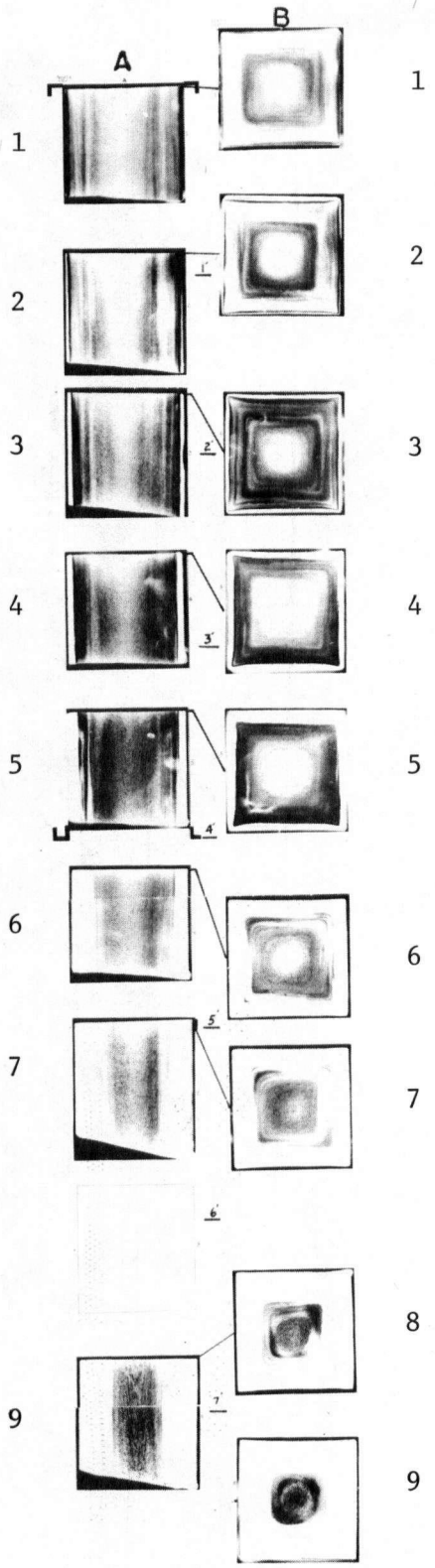

Figure 27. Composite of autoradiographs of billet, Test U1, showing the pool profile down the strand (A) and perpendicular to the strand axis (B).

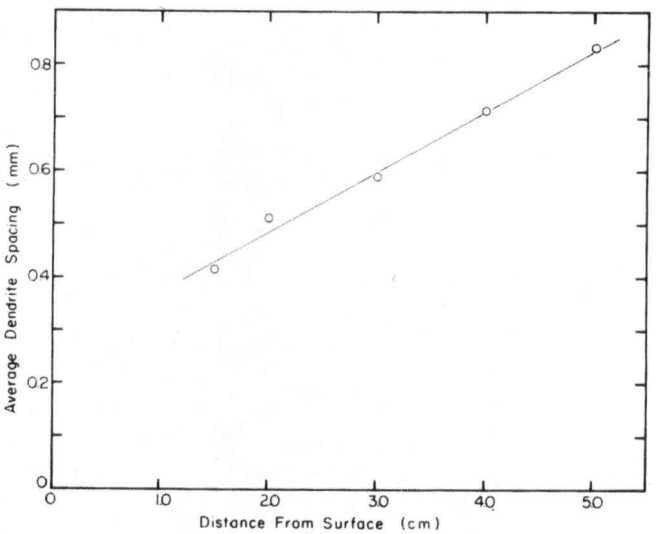

Figure 29. Measured average dendrite spacing as a function of distance from the billet surface for Test U1.

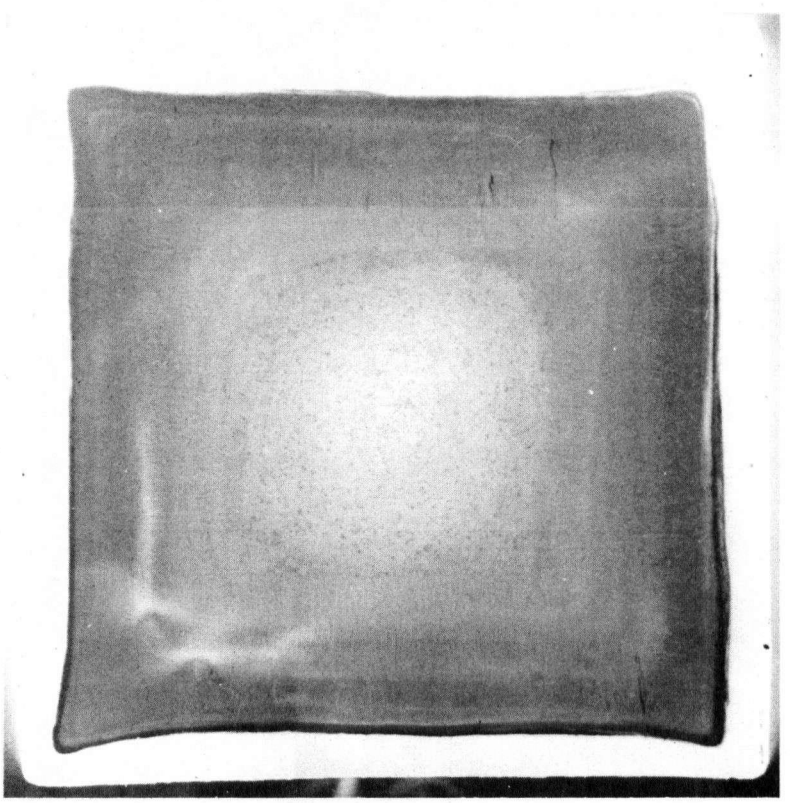

Figure 30. Section B5 of Figure 27, showing radial cracking in transverse section.

measurements are given in Figure 29. In the equiaxed zone, solute rich pipes can be observed (section A9) forming a V pattern.

Radial cracking occurred in most of the sections examined. Areas where radial cracks were found are: 1. near the Southwest and Southeast corners, 1.5 to 2.5 cm. from the outside surface parallel to the North face; 2. 3.0 to 3.5 cm. from the East face and 2.5 to 4.0 cm. from the West face parallel to the North face. These cracks can be observed in section B5, Figure 30.

Some evidence of centreline porosity was observed in the billets. In section A10, the dark regions in the upper part of the section correspond to holes.

4.2. Calculated and Measured Pool Profiles and Pool Depths

4.2.1. General Comments

In Table V the values of the casting parameters measured during the tests, the measured mold heat fluxes and the measured and calculated pool depths are listed. The lengths and heat transfer coefficients of the successive spray zones are given in Table III. In Table I the thermophysical properties of steel used in the models and in the calculation of the mold heat transfer coefficient, $\bar{h}_M$ (Table II), are presented. Using these values in the finite difference and integral profile models, the pool profiles in the mold and submold regions and strand surface temperatures were calculated. The results are plotted in Figures 31 to 40.

4.2.2. Calculated and Measured Pool Profiles in the Mold

In the figures showing the pool profile in the mold region, (Figures 31 to 35), curves A and B were calculated using the one-dimensional finite difference model with equations (7) and (6) respectively to describe the surface heat flux. For comparison, in Figures 31 and 32(b), the integral profile model was used to calculate the pool profile giving curves C and D with equations (7) and (6) respectively to define q_o.

The shell thickness of the casting as a function of distance below the meniscus was measured from the autoradiographs. These measurements were made on the longitudinal sections, i.e., at the mid-point of the outside and inside radius faces. Figures 31 and 33 show the variation in shell thickness between the outside and inside radius for the stainless steel slab and a 10.1 cm. billet (Test M3). In all other figures, the average of the shell thickness from the two sides is plotted along with the calculated shell thickness.

4.2.3. Calculated and Measured Pool Depths

The pool depths for the stainless steel slab (Figure 36) and for the web and flange areas (shaded areas in Figure 38) of the beam blanks (Tests Aℓ1 and Aℓ2, Figures 39(a) and (b)) were calculated with the one-dimensional finite difference model. In Figure 36, Test At1, the pool profiles have been calculated with both the finite difference model (curves A and B) and the integral profile model (curve C). For the beam blanks, curves A and B, for the web and flange areas respectively, were

calculated with the finite difference model and curve C with the integral profile model.

For the tests on the blooms and billets (Table V) the pool depths were calculated with the two-dimensional finite difference model. The position of tungsten pellet with respect to the calculated shell thickness is shown for Tests At1 (Figure 36), M2 (Figure 37(a)), M3 and M4 (Figure 37(b)), Aℓ1 and Aℓ3 (Figure 39(a) and (c)) and W2a and W2c (Figure 40).

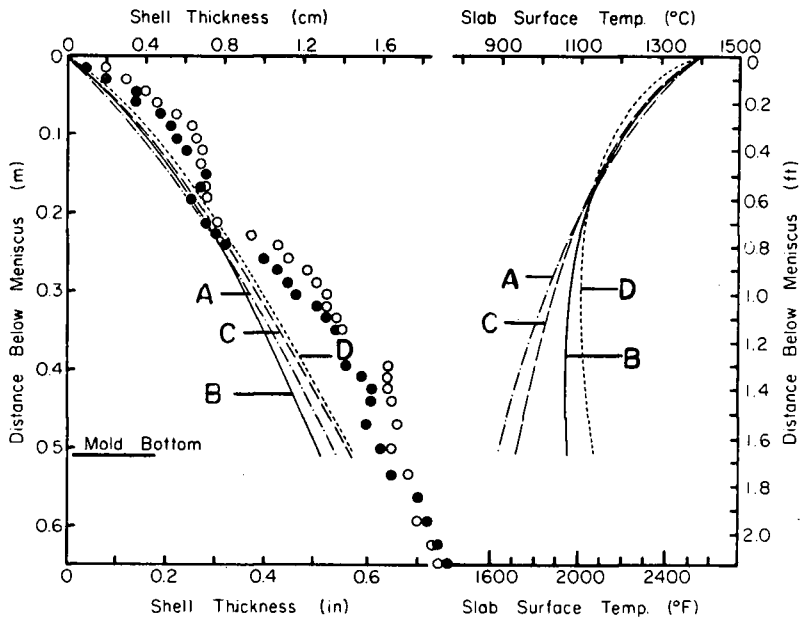

Figure 31. Liquid pool and surface temperature profiles in the mold region for the stainless steel slab O, measured inside radius; ●, measured outside radius. A, calculated finite difference with equation (7). B, calculated finite difference with equation (6). C, calculated integral profile with equation (7). D, calculated integral profile with equation (6).

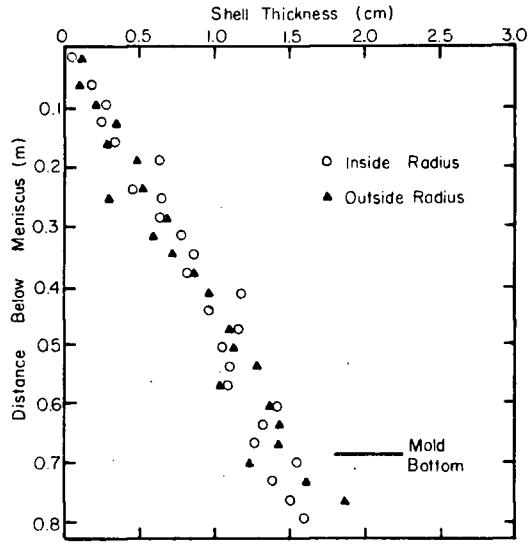

Figure 33. Shell thickness for inside and outside radius faces from Test M3.

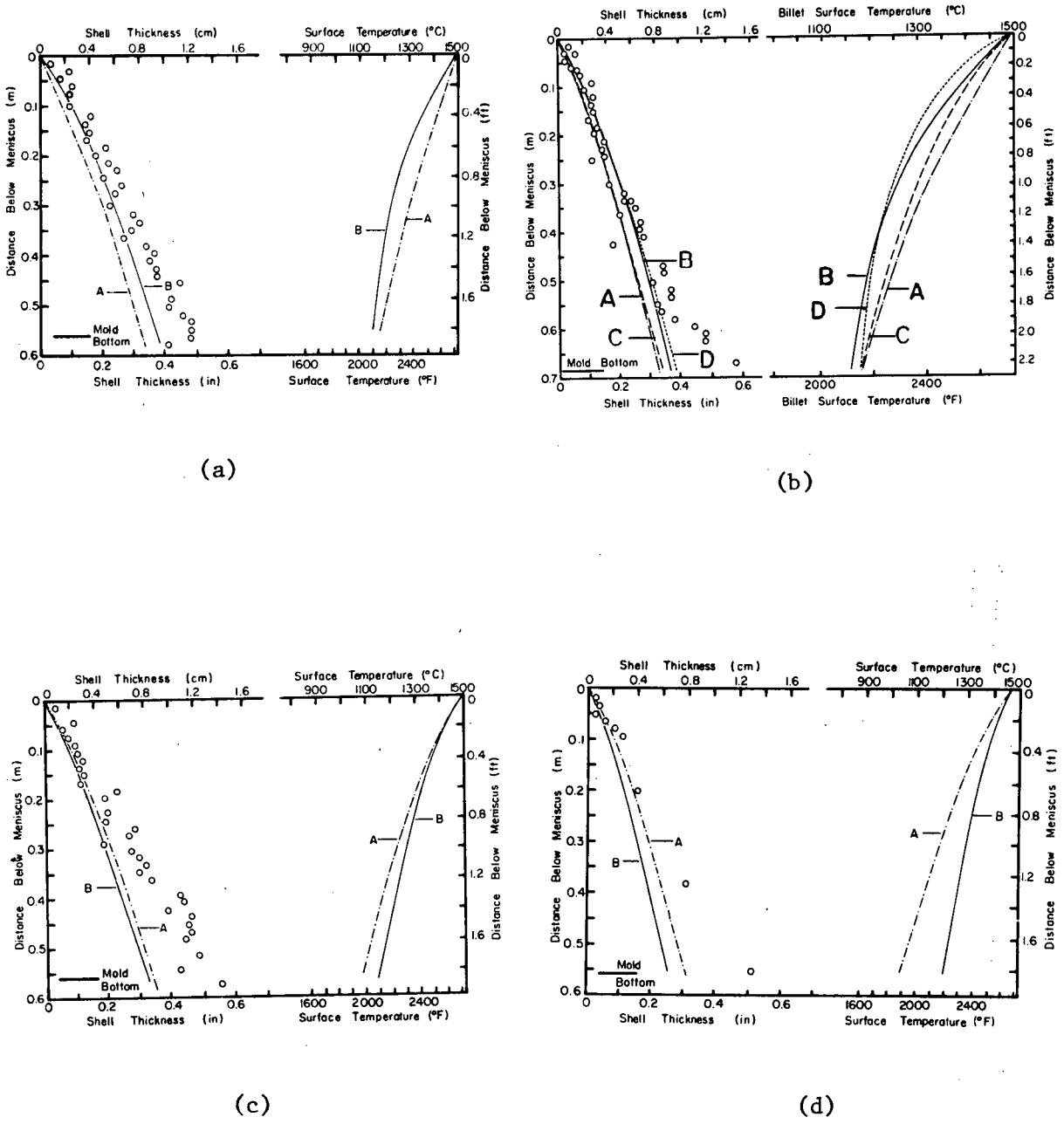

Figure 32. Liquid pool and surface temperature profile in the mold region for (a) Test M1, (b) Test M2, (c) Test M3, (d) Test M4. O measured, average shell thickness of inside and outside radius surface. Caption as for Figure 31.

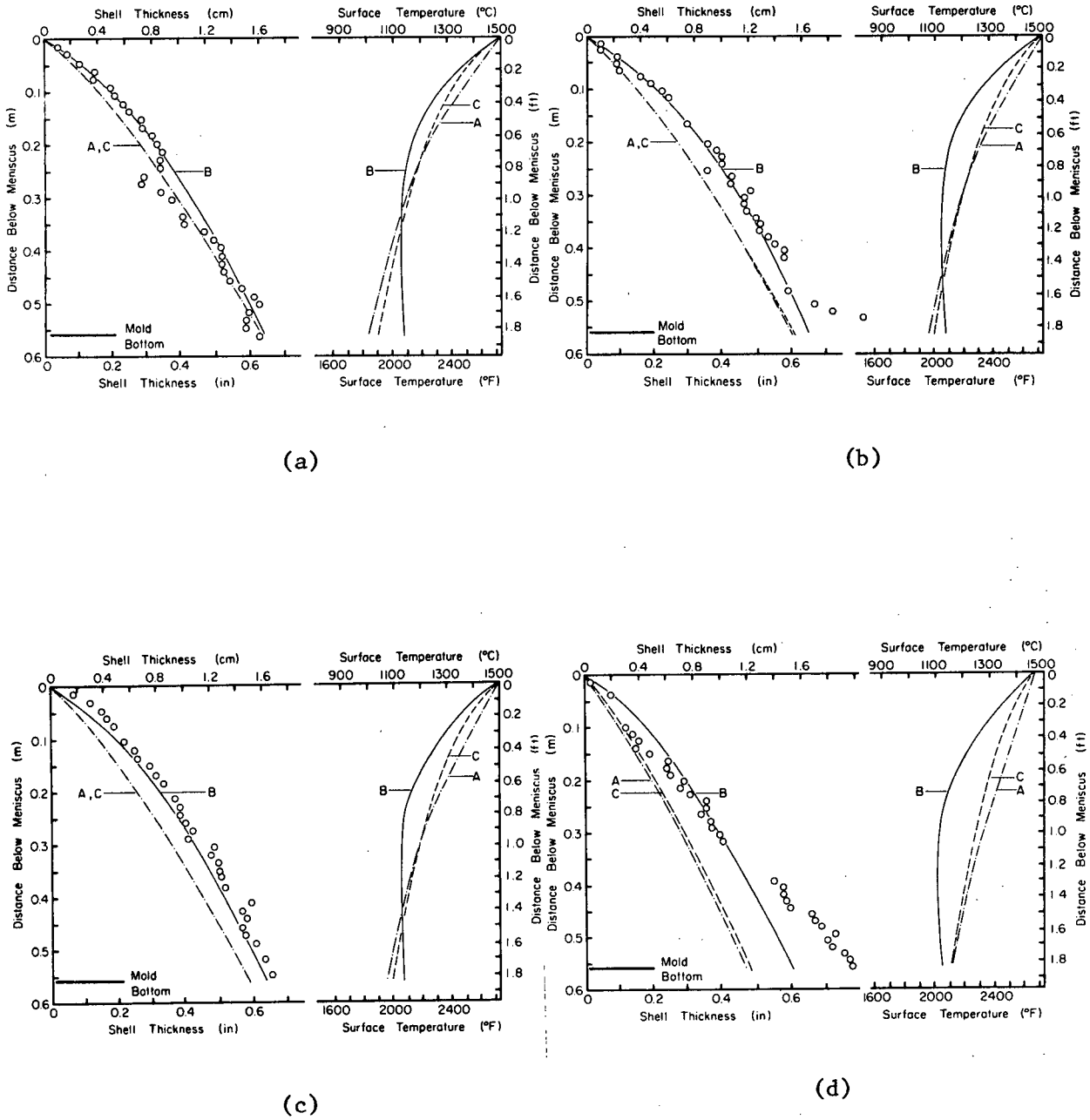

Figure 34. Liquid pool and surface temperature profiles in the mold region for (a) Test Aℓ1, (b) Test Aℓ2, (c) Test Aℓ3, (d) Test Aℓ4. Caption as for Figure 32.

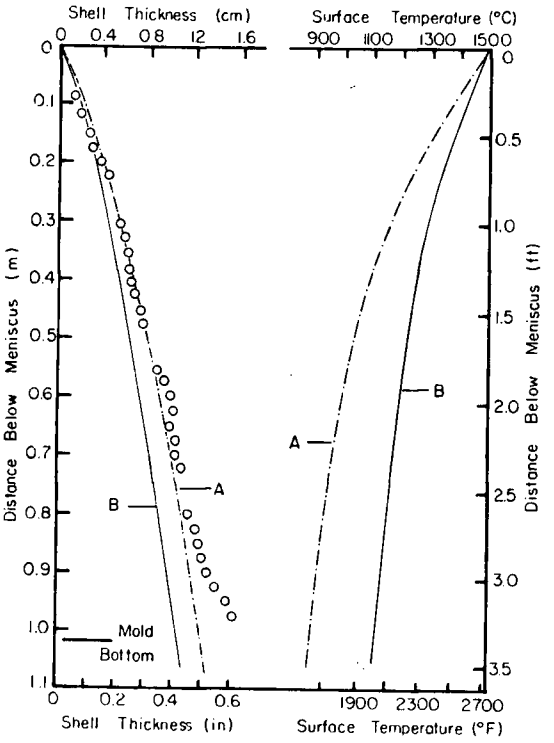

Figure 35. Liquid pool and surface temperature profiles in the mold region for Test U1. Caption as for Figure 32.

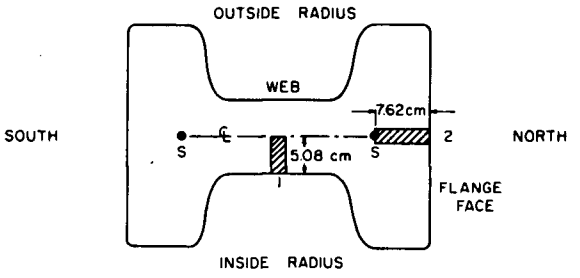

Figure 38. Position of horizontal slices in web area, 1, and in flange area, 2, of A and E beam blanks used in calculating pool profiles with the one-dimensional models. S, positions of input streams.

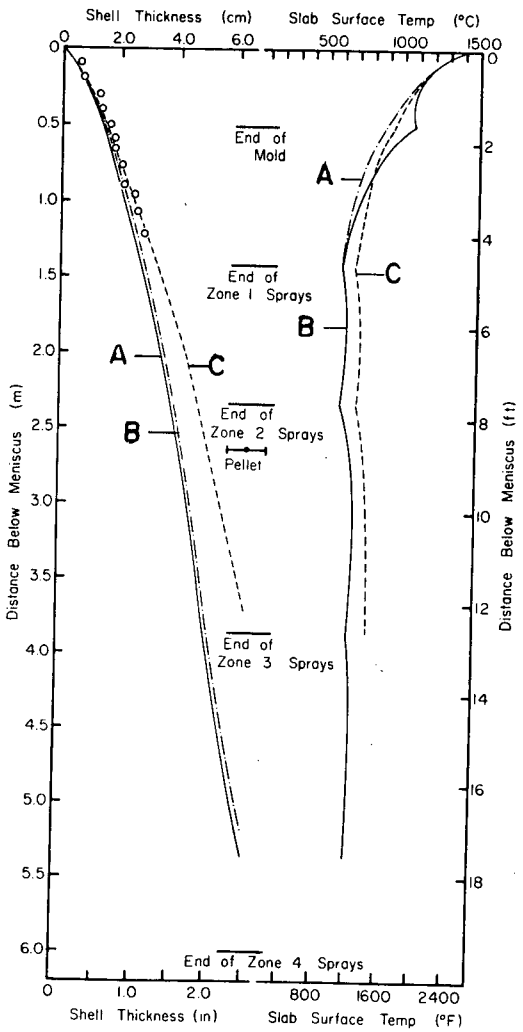

Figure 36. Liquid pool and surface temperature profiles for the stainless steel slab. Caption as for Figure 32.

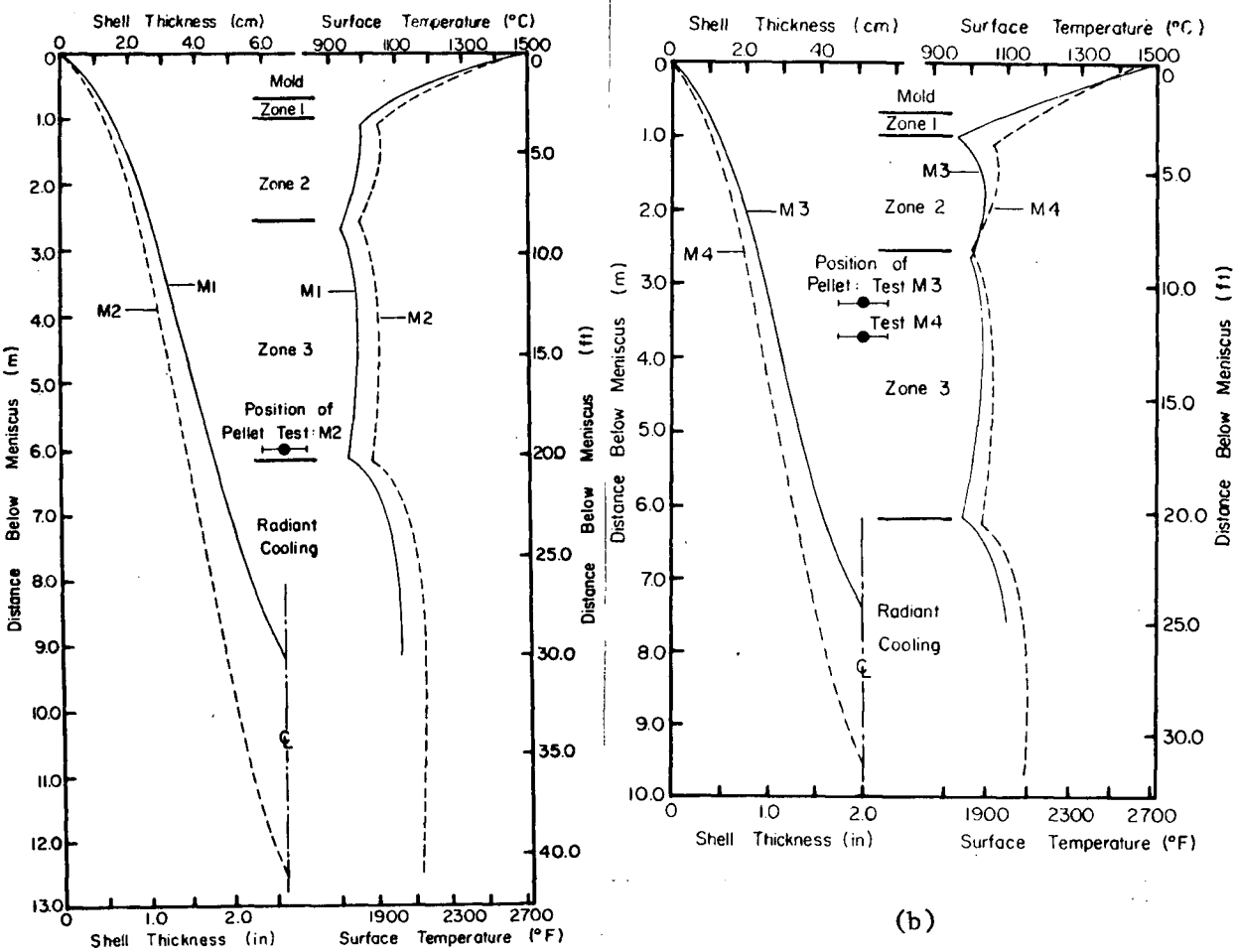

Figure 37. Liquid pool and surface temperature profiles for (a) Tests M1, M2, (b) Tests M3, M4. Caption as for Figure 32.

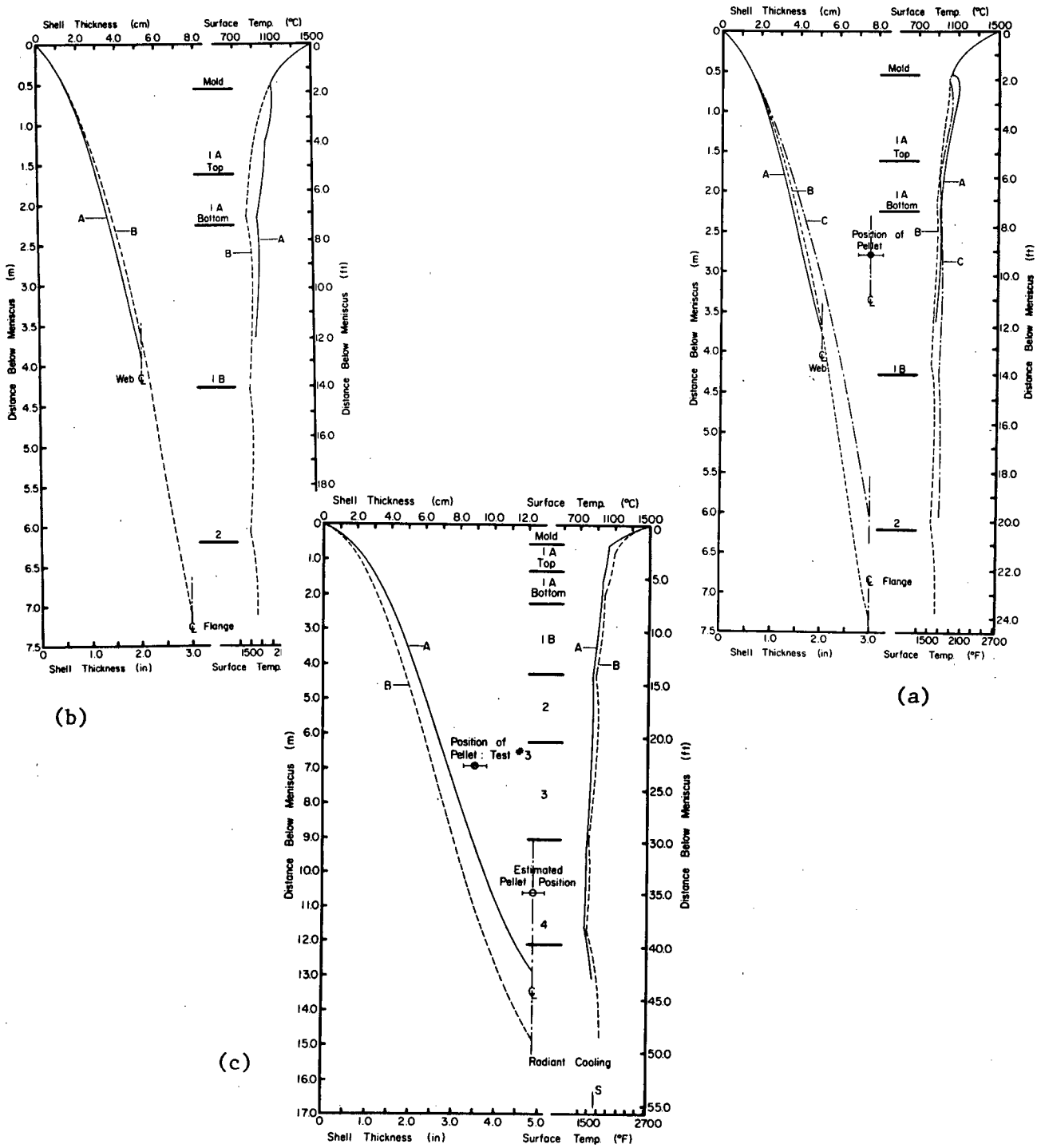

Figure 39. Liquid pool and surface temperature profiles for (a) web (A) and flange (B) areas of A beam blank, Test A&1. Curves A and B calculated with finite difference using equation (7), curve C with integral profile using equation (7). (b) web (A) and flange (B) areas of E beam blank Test A&2. Caption as for Figure 39(a). (c) A, Test A&3. B, Test A&4. Curves calculated with finite difference model using equation (7). S, temperature of blooms at straightener, 900°C.

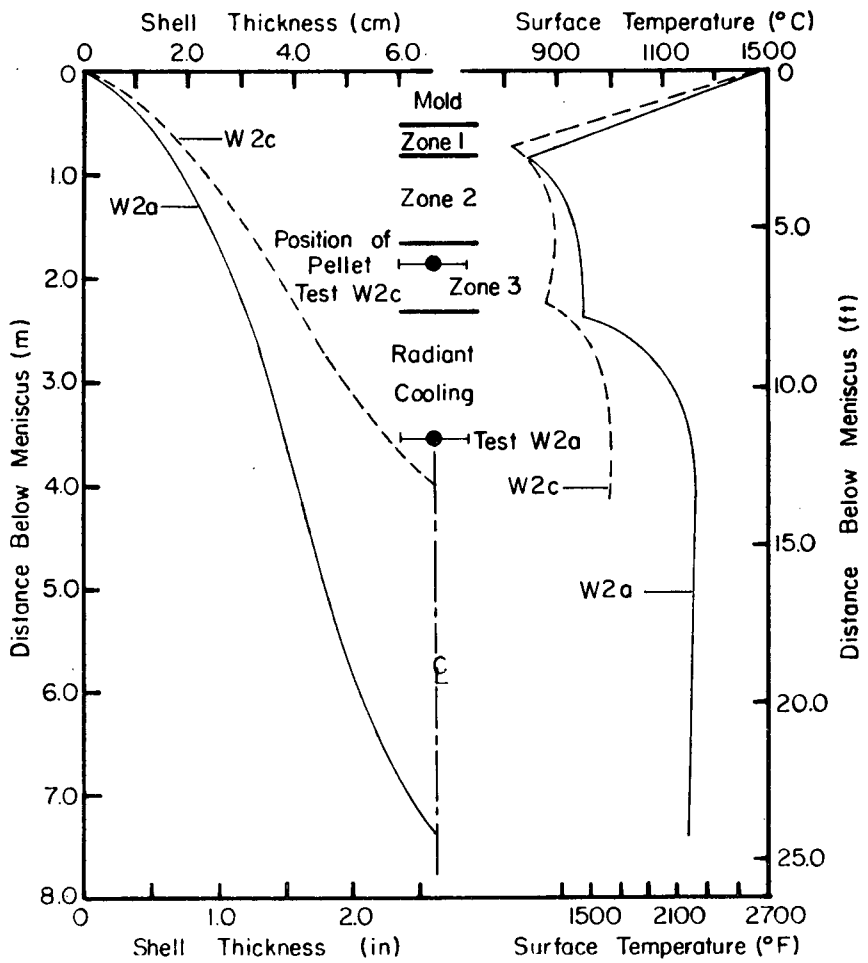

Figure 40. Liquid pool and surface temperature profiles for Test W2a and Test W2c.

5. DISCUSSION

5.1. Liquid Mixing, Solid Shell and Cast Structures

5.1.1. Liquid Mixing

5.1.1.1. General Comments

The present results indicate that the fluid flow pattern in the liquid pool is complex. The distribution of radioactive gold in the pool depends to a great degree on the method of tundish teeming, i.e. open pour or submerged shroud, and the method of tracer addition to the pool. Since the method of tracer addition was the same in all tests, variations in mixing characteristics are mainly a result of tundish teeming practice.

5.1.1.2. Open Pour

When open pouring between the tundish and mold is used (all tests except At1 and Aℓ4) extensive mixing occurs in the mold and upper sub-mold regions. Most of the gold mixes below the meniscus sharply outlining the solid-liquid interface in the mold. In the sub-mold region, the interface becomes less distinct due to incomplete mixing. The gold

never mixes to the pool depth measured with the tungsten pellet. This indicates that the gold rich region in the lower pool is surrounded by liquid metal with no discernable mixing between the two liquid zones. In some tests the gold penetrated to near the pellet position (see Test M3, Figure 7). The penetration may be associated with the manner in which the gold entered the liquid pool, the high density gold falling further before being mixed in the pool, outlining the outside radius solid-liquid interface.

In the autoradiographs alternate light and dark bands in the transverse sections and light and dark cones in the longitudinal sections were observed. Similar bands have been observed in other tracer work on both continuous and static castings[35,36]. According to the literature[36] the bands can also be seen in sulphur prints, although this was not observed in any of the tests. The presence of the bands cannot be accounted for at present. They may result from fluid flow due to solidification shrinkage and thermal contraction as the strand solidifies. The temperature gradients in the liquid pool in this region must be very small, making any estimate of the buoyancy forces due to density variations in the liquid difficult.

In the E profile beam blank (Test Aℓ2, Figure 16) there was less mixing of the gold than in any other open pour test. It is not clear why this occurred. From Figure 17, it is apparent that as much or slightly more gold mixed in the liquid pool above the meniscus than below it. Similar high activity distributions above the meniscus were observed in Test Aℓ4 and At1 where submerged shrouds were used. However, in tests involving open teeming, the activity usually dropped off sharply above the meniscus. The activity distribution in Test Aℓ2 may be tentatively

explained by assuming that a part of the gold addition was picked up directly by the input stream and, despite mixing, was maintained as a region of high gold concentration, while it moved rapidly down through the pool into the lower region of the mold where the stream momentum is small. This gold rich region would then produce the peak in activity seen 13 to 25 cm. below the meniscus. At the same time, the rest of the gold added to the pool would have been distributed quickly throughout most of the mold region to delineate the solid shell observed in the autoradiographs.

Near the bottom of the mold, a portion of the gold rich liquid could be caught by a recirculating stream flowing up the side walls or up the centre of the web. The rise velocity, from model measurements of Szekely and Yadoya [3], appears to be low, probably less than 5 cm. $sec.^{-1}$. The return of the gold rich steel to the surface of the liquid pool would then take roughly 12 sec. or more. In the meantime the strand, with the meniscus initially outlined by the gold, would have descended a distance of 18 cm. Thus, the gold rich liquid would move above the original meniscus and eventually come into contact again with the input stream near the top of the pool. The reappearence of gold in the region above the original meniscus would give rise to the second peak in activity 18 to 32 cm. above the meniscus line in Figure 17. The dip in activity between the peaks would be due to the successive dilution of gold in the pool by the input stream after the gold addition.

5.1.1.3. Submerged Shroud

Use of a submerged entry shroud markedly changes the flow pattern and distribution of gold in the liquid pool. The exit ports from

the shrouds used in Tests Aℓ4 and At1 were angled 20 and 15° above the horizontal. From the autoradiographs and the activity distributions (Figures 12 and 17) it was observed that the flow patterns and mixing characteristics in the two tests were similar.

The results in Test Aℓ4 indicate that flow from the radial input stream divides essentially into two parts, possibly equally. One part mixes into the small liquid region above the input stream, and subsequently mixes upward and becomes diluted as the slab is withdrawn and the initial point of introduction moves downward. The other part flows across the pool, down the end wall to about 100 cm. below the meniscus, and then back to the centre of the slab. Flow also occurs down the side wall, adjacent to the end, more extensively on the outer radius side of the slab. Much of the gold is therefore distributed around the periphery of the slab by the momentum of the input stream. Subsequently flow occurs at a much lower rate into the lower part of the liquid pool, due to volume shrinkage, and solute and thermal gradients, from the central regions of the upper part of the pool. This results in a relatively dark region in the central lower part of the pool and a gold depleted region in the central part of the upper region of the pool, as is observed. These results differ markedly from those predicted by Szekely and Yadoya[3] on the basis of a water model study of fluid flow associated with radial input streams. They concluded that penetration with radial nozzles is small and is much less than with straight nozzles. The present results indicate appreciable penetration of the liquid pool by the input stream with radial inputs.

The difference between these results and the results

presented by Szekely and Yadoya may be due to the difference in the head of liquid metal feeding the mold. Since the tundish nozzle feeding the shroud is smaller than the shroud exit ports, the shroud will not be entirely full of liquid metal. Thus, the head of liquid metal feeding the mold will be the height of the liquid surface in the shroud above the meniscus. If the head of liquid in the shroud decreases, the input stream momentum would drastically decrease resulting in a reduction in mixing in the liquid pool. This effect is observed in Tests Aℓ4 and At1. In the Atlas case a bifurcated shroud is used with extensive mixing occurring, whereas at Algoma, a four-holed shroud is used giving less mixing in the pool since the head of metal in the shroud is lower due to the increased cross sectional area of the shroud exit ports.

In the test at Algoma, Figure 23, the flow pattern can be inferred to result from the input stream splitting into two parts similar to the Atlas case. The lower portion of the stream formed a cell flowing down the outside of the casting, across to the centre and then up the central axis.

5.1.2. Solid Shell

5.1.2.1. Near the Meniscus

A possible mechanism leading to the fluctuations of shell thickness observed in the longitudinal sections in some experiments is that a small segment of the shell, attached to the mold at the meniscus, is torn from the continuous solid shell and moves above the liquid surface on the upward stroke of the mold. On the downward stroke, the lower end

of the segment is pushed away from the mold by the thin solid shell it encounters. This results in poor local thermal contact with the mold and therefore, a locally thin shell. This mechanism accounts for ripple marks being present on the strand surface wherever there is a localized thinning of the solid shell and the presence of shell segments above the meniscus. It appears that the shell thickness variations are dependent in a complex fashion on the lubrication and mold configuration. Tearing of the shell might occur at the corners of the mold and then propogate across the faces. In this case, the detailed mold finish at corners as well as the lubrication practices might be critically related to the fluctuations.

When casting at low speeds, the ripple marks and shell fluctuations can be directly related to the mold oscillation. At Algoma Steel, in Test Aℓ1, Aℓ2 and Aℓ4, the shell fluctuations and ripple marks occur at 3.2, 3.1 and 3.5 cm. intervals respectively. Assuming the shell tears uniformly on every upstroke of the mold, the distance between fluctuations is calculated to be 3.4 cm., based on an average casting rate of 1.5 cm./sec. and a mold oscillation stroke length of 1.9 cm.

When casting at high speeds, Tests M1 to M4 and U1, no apparent periodicity in shell fluctuations is observed. This is reasonable since at these high casting speeds, shell tearing at the meniscus is probably irregular and intermittent. Thus no direct relationship between mold oscillation and shell tearing can be made. The irregular tearing of the shell at the meniscus is a possible explanation for the difference in the position of the meniscus on either side of the billet in Test U1, Sections A2 and B2 (Figure 27).

5.1.2.2. Mold Region

The solid shell progressively thickens with distance down from the meniscus. In all of the tests the shells formed were relatively uniform around the periphery of the mold.

In Tests Aℓ1 and Aℓ2 (Figures 13 and 16) it is evident that the second generation mold (E profile) is as satisfactory as the first generation mold (A profile) in producing a uniform shell around the entire mold. Also A and E beam blank have the same shell thickness on leaving the mold indicating that the heat flux from both molds is identical. The flange corners of the E beam blank (Figure 16) are more uniform than the corners in the A beam blank (Figure 13, compare F3 to B6), which suggests that less distortion of the E beam blank occurs during solidification in the mold. It is not apparent why less distortion occurs, nor whether this difference is consistent since only one test was carried out for each mold.

The reasons for the large fluctuations in shell thickness observed in the web area of A beam blank (Figure 16, sections C1 to C3) are not clear. Since the first large fluctuation occurs at about the centre of the mold, the event causing the fluctuation likely occurs in the mold.

In tests conducted on both curved and straight molds re-entrant corners have been observed (see Table VII). It is speculated that the formation of these corners is due to the strand shrinking during solidification and losing contact with the mold wall. The ferrostatic pressure on the solid shell increases with distance below the meniscus eventually causing the strand to bulge. This results in the centre of the

face of the strand making good contact with the mold and the corners losing contact. Consequently, the solidification rate decreases in the corners and the solid shell is thin locally.

Ushijima[12] has shown that re-entrant corners observed in pour out tests at corners of steel sections can be associated with corner cracking. The cracking in the shell results from high tensile stresses at the corner due to the bulging of the shell near the corners. He associated corner cracking with the corner curvature of the mold, and defined a range of corner radii in which corner cracking would not occur. Unfortunately, the radii he proposed are usually too large for commercial castings since with increase in corner radius, mold dressing becomes a problem.

A corner crack in a re-entrant corner is shown in Figure 24(a) and (b). The crack occurred in the mold, close to the meniscus, presumably as a result of local strains. From the sulphur print and autoradiograph it can be seen that the crack was filled by solute rich liquid which was immediately ahead of the solid-liquid interface. The crack healed in the mold, since there was no breakout, but would be a point of weakness below the mold. This could lead to the longitudinal corner-cracking, observed on the outside surface of the bloom.

5.1.2.3. Submold Region

Generally the shell thickness below the mold is not clearly outlined indicating little mixing occurring in this region.

In Test A&1 deformation of the solid shell by support rolls in the spray region is seen in Figure 14(a). One or more of the web rollers were misaligned on one side causing distortion of the shell in the web fillet area. Also the wavy contour of the solid-liquid interface along the wide flange face in Figure 14(a) may be due to deformation by the support rollers. As described by Lucenti[33] rollers are used against the web, flange face and flange tips in the spray zones to maintain the mold contour of the beam blank. Without the constraining rolls on the flange, the flange deformed to the shape shown in Figure 41(a). The wide face of the flange bulged out, resulting in a distortion of the inside radius flange edge, as shown, which could lead to longitudinal flange tip cracks. The presence of the rollers reshapes the beam blank by deforming the solid shell. The deformation does not shift the solid-liquid interface in the flange edge, accounting for the divergence of the plane of the interface in the autoradiographs from the flange edge surface.

5.1.3. Cast Structure

5.1.3.1. Stainless Steel

In the test involving the casting of stainless steel, the cast structure consisted of a large columnar zone and a relatively narrow equiaxed zone. The small gold free spots observed in some sections (L8 to L10, Figure 10) are probably small dendrites which have formed in a gold free part of the liquid pool, and fallen down the pool to the positions observed in the autoradiographs. It is not clear to what the dark structureless spots (also observed in the autoradiographs) can be ascribed.

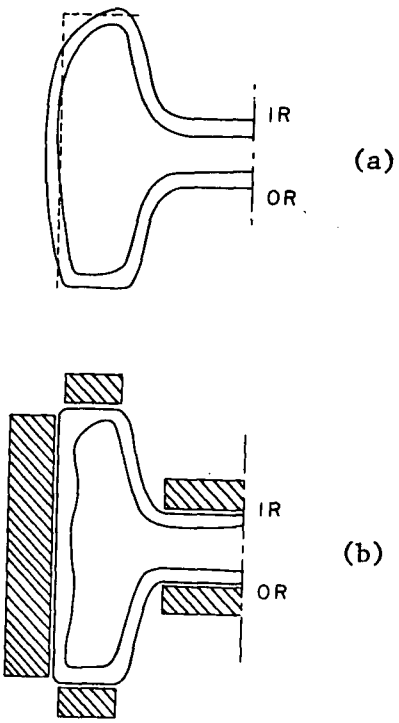

Figure 41. (a) Schematic drawing of distorted shell without flange rollers. (b) Shell contour after deformation by flange rollers.

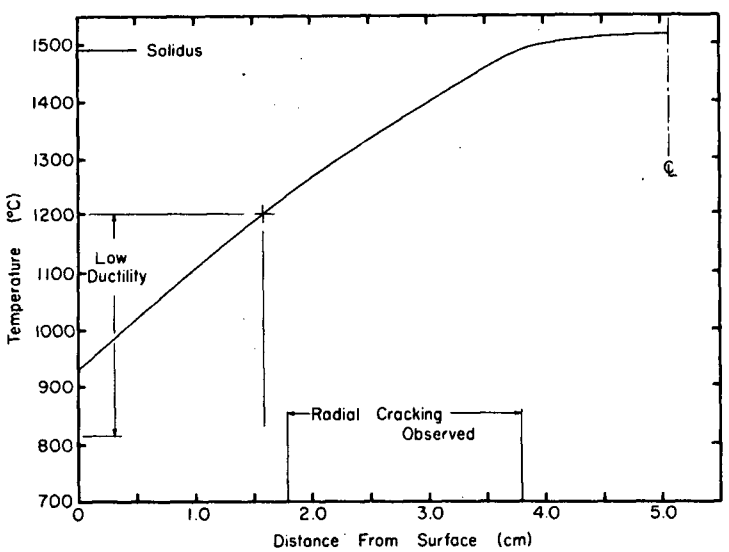

Figure 42. Temperature distribution in A beam blank web, Test Aℓ1, 2.5 m. below meniscus. Estimated region of low ductility[14] is indicated as well as the observed region of radial cracking.

In some sections (C3, C6, and L12) the solid-liquid interface delineated by the gold had a series of small regular bumps. These appeared to be associated with dendrite tips at the advancing interface. Since only the dendrite tips are outlined, it would appear that little liquid has penetrated into the solid-liquid zone. Tip spacings of about 1.9 mm. were measured at a shell thickness of 1.6 cm. in section C3.

The dendritic structure in the centreline of the slab may be due to both dendritic debris falling from the upper part of the pool and, since the casting is mainly columnar, dendritic bridging of the centre by columnar grains. The difference in the dendritic structure along the centreline of the transverse sections suggests more debris drops from the middle of the slab, closer to the point of introduction of the input stream, than at the slab ends.

In using electron probe microanalysis of the concentration of nickel and chromium in a 304 slab, cast at Atlas Steels in a similar manner to the present test, R. Dickens[37] has shown that no significant macrosegregation occurs at the slab centreline. The results also indicated that microsegregation between the primary dendrites did occur, as was anticipated.

5.1.3.2. Effect of Tundish Teeming

In most of the tests where open teeming from the tundish was used, the cast structure consisted of a columnar region around the periphery of the casting and a central equiaxed region. Where a submerged shroud was used (Test Aℓ4, Figure 23) the cast structure consisted of cored, dendritic, equiaxed grains with no resolvable columnar region. The larger volume of equiaxed grains in this casting may result from the radial input streams

directly impinging on the solid-liquid interface. This could cause extensive local remelting of fine dendrites to occur, appreciable increasing the number of nuclei in the liquid pool. The number of nuclei in this test may have been further increased by the addition of aluminum to the melt in the ladle.

Only in Tests M3 and M4 did the cast structure, when using open pouring, differ from the normal. In these tests the bulk of the cast structure consisted of small dendritic grains with no apparent columnar region. The structure indicates that copious nucleation occurs in the upper part of the liquid pool. The nuclei fall and fill the relatively short pool preventing columnar growth. Because of the small size of the billet (10.1 cm.) and high casting speeds (5 cm./sec.), the relatively large input stream causes a high degree of turbulence in the mold. This could result in extensive local dendrite remelting, thus increasing the number of nuclei in a similar manner as in Test Aℓ4.

5.1.3.3. Columnar Structure

The columnar grains were sufficiently clearly resolved in the autoradiographs in some of the tests that the primary dendrite spacing could be measured as a function of distance from the outside surface. The results of these measurements are shown in Figure 29 (for Test U1) and in Table VIII. Also in Table VIII, the range of primary dendrite spacings with distance from the surface in AISI 4340 steel cast unidirectionally against a water cooled copper block is given[38]. These results indicate that the heat transfer between the strand and the mold in the present experiments is less efficient than in the case of steel cast statically

Table VIII. Measurements of Dendrite Spacing

Test No.	Dist. from Surface (cm)	Meas. Primary Dendrite Spacing (mm)
Aℓ1	3.0	1.0
Aℓ3	4.5	1.0
U1	1.5 to 5.0	0.4 to 0.8
At1	1.6	1.9
Weinberg & Buhr	1.6 to 5.0	0.2 to 0.4

against a cold block, and therefore, the freezing conditions and resulting structure are not comparable. It is also interesting to note that the dendrite spacing in the stainless steel slab is much larger than in low carbon steel castings, probably due to the greater freezing range in stainless steel.

5.1.3.4. Equiaxed Structure

The equiaxed grains in the centre of the strands are likely formed near the lower limit of penetration of the input stream, where significant temperature fluctuations can be expected, and where larger dendrites have had a chance to develop at the solid-liquid interface. The nuclei are secondary dendrite branches separated from the primary branches by local remelting. The nuclei fall in the pool, due to their slightly higher density, and grow, in the absence of significant temperature gradients in the liquid, in areas of progressive solute enrichment due to

constitutional supercooling. This suggests that the number, size and distribution of the equiaxed grains is related to the penetration of the input stream, the flow pattern in the liquid and the alloy composition. The effect of different flow patterns on the equiaxed zone was discussed in an earlier section.

When the strand is cast using a curved mold, because of the curvature of the casting, the grains will tend to fall and form a loosely packed agglomerate on the outside radius solid-liquid interface. As a result columnar growth on the outside radius is halted and columnar growth on the inside radius is allowed to proceed to near the casting centreline. This accounts for the observed displacement of the casting centreline and the presence of an equiaxed structure in the outside radius half of the strand. When a straight mold is used, there is no observable shift in the equiaxed zone from the casting centreline (see Test U1, B6, Figure 27).

In Test U1, section B6, it can be seen that the columnar structure terminates abruptly at the columnar-equiaxed transition line. At this transition there is no significant concentration of gold ahead of the columnar structure. This indicates that there is no significant macro-segregation ahead of the advancing columnar grains. At this level, the liquid adjacent to the interface in Figure 27 is not mixed with the centre liquid, indicating that there is little fluid flow to reduce concentrations of gold ahead of the interface, if such concentrations existed.

In Tests M1 and M2 (Figure 7) the centreline porosity is a result of inadequate feeding of liquid at the bottom of the pool, due to periodic bridging across the pool by dendritic debris or radial dendrites. Along the centreline of the castings a band of gold rich material is

observed. This band may be caused by the last liquid to solidify, rich in solute material, flowing into the shrinkage cavities created as a result of bridging at the bottom of the pool and freezing rapidly without significant segregation. It is not clear why bridging across the pool occurs periodically. This effect is also observed to a lesser degree in Tests Aℓ3 and At1.

5.1.3.5. Solute Rich Pipes in Equiaxed Zone

In Test Aℓ4 (sections L1 and M5, Figure 23 and sulphur print of L1 in Figure 25) and in Test U1 (section A9 and B series, Figure 27) gold and sulphur rich pipes forming a V pattern were observed. In the longitudinal sections (A9 and L1) the pipes appear as long dark lines. The lines are not as steeply inclined as the solid-liquid interface, tending to form a larger angle with the vertical axis toward the centre of the strand. In the transverse sections (B series) the pipes tend to be small and round, becoming larger and more irregular near the centre of the strand. The presence of these pipes is probably due to liquid flowing down through the solid-liquid mass to feed volume shrinkage associated with solidification. The pipes are likely a reflection of the packing of dendritic debris as it falls down the liquid pool. Some debris will attach itself to the solid-liquid interface with greater frequency towards the bottom of the pool as the debris becomes larger in size. As a result, the effective solid-liquid interface will become more inclined away from the vertical lower in the pool. The solute rich liquid will search for pipes of poor packing and flow down these pipes, melting small barriers, if they exist, to form the observed V segregate pattern.

5.1.3.6. Radial Cracking

The ductility of continuously cast mild steel at high temperatures has been related by Lankford[14] to the Mn/S ratio in the steel. At low ratios, 20, the steel has poor ductility while at high ratios, 60, it has good ductility. Table VII gives the tests in which radial or centreline cracking was observed and the corresponding Mn/S ratio. Generally, radial cracking was observed in tests having a low to intermediate Mn/S ratio. All cracking is interdendritic in agreement with the Lankford model since unfavourable Mn/S ratios would occur in interdendritic areas, due to sulphur segregation during freezing, leading to poor ductility.

Radial cracking caused by deformation of the partially solidified strand can be observed in Test Aℓ1, Figures 14 and 15. Deformation of the shell by the corner of a roller would cause high tensile stresses in the interior of the shell. This leads to interdendritic cracking which would extend to the interface, the crack then being filled with solute rich liquid. Most of the radial cracks terminate about 3.6 cm. from the outside surface of the beam blank. If this is assumed to be the position of the interface when the cracks formed, then from the heat analysis described earlier, this shell thickness would occur at about 2.5 m. below the meniscus. The temperature profile across the shell at this depth can be calculated, and is shown in Figure 42. Using the temperature range over which the steel is brittle, from Lankford[14], the probable range of radial cracking is indicated as a function of distance from the beam blank surface. The observed range of radial cracking is shown to be a little further from the beam blank surface than that estimated. However, considering the assumptions made, the estimated and

observed range of radial cracking are not too divergent. Radial cracks on the inside radius flange tip can also be attributed to tensile stresses introduced in the interior of the shell, when the shell is being deformed, by the flange and flange tip rollers. These cracks extend over a similar range as those described previously, 1.9 to 3.6 cm. from the outside surface. This suggests that the flange tip cracks occur at approximately the same distance below the meniscus as the web radial cracks, and are due to deformation.

It is difficult to determine the cause of radial cracking in the other tests. Cracking may be related to thermal stresses set up in the strand in the water sprays, deformation by misaligned support rollers and local tensile stresses resulting from compression of the strand by the withdrawal or straightening rollers. The intergranular centreline cracking observed in some tests is probably a result of thermal stresses set up in the strand in the spray and radiant cooling regions. These stresses cause cracking at the solute enriched grain boundaries at a time when some residual liquid was still present to fill the crack.

5.1.3.7. Sulphide Inclusions

In Tests Aℓ1, Aℓ3, M1 and M2, clumps of sulphide inclusions were found in the inside radius of half the strands. Since the clumps are enriched in gold and sulphur, they must have formed in the solid-liquid region of the solidifying front, at a point different than their final position (see Figures 14 and 15). The fluid flow results suggest that little flow occurs in the lower part of the pool. Accordingly, the evidence indicates that the clumps of inclusions, after their formation,

floated up in the liquid pool due to their low density, until they met the solidifying front advancing from the inside radius surface. Thus, they can be seen to form a band parallel to the inside radius surface (see Figures 14(a) and (b)). The inclusions present near the outer surface of the strand(see Figures 15(a) and (b)) are also consistent with the hypothesis that clumps of inclusions float up in the liquid from the solidifying front in the lower pool regions since little segregation between the fine columnar dendrites would occur. The rising velocity for a 500μ inclusion is 14 cm./sec., from Stokes Law[39]. Therefore, there is ample time for the inclusion to float up through large distances in the pool.

The distribution of inclusions seems to be dependent on the Mn/S ratio in the steel. With a low ratio, clumps of MnS inclusions are found in a band near the inside radius surface. With a high Mn/S ratio, the clumps of inclusions are uniformly dispersed throughout the casting (compare Figures 14, 15, and 22 to Figures 18, 19, and 26).

5.2. Calculated and Measured Pool Profiles and Pool Depths

5.2.1. Validity of Assumptions in Mathematical Models

The assumptions in the models regarding the release of latent heat and the use of an effective thermal conductivity should be examined before comparing the predicted and measured pool profiles for the tests. For the stainless steel slab (Test At1) the effect of changing the method of latent heat removal on the solidification rate was evaluated by altering γ_S (see Figure 2). This in effect changes the quantity of latent

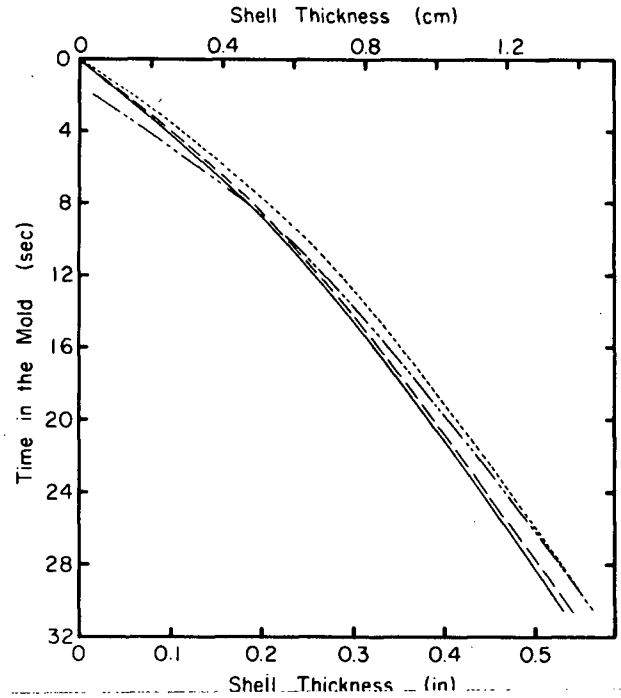

Figure 43. Effects of method of latent heat evolution and use of k_{eff} on calculated shell thickness for the stainless steel slab. k_{eff} used for T > 1460°C, % latent heat released at solidus: 25, 50, 75%, ═══ ; 100%,– – –. k_{eff} used for T > 1399°C, 100% latent heat released at solidus —·—·— . Integral profile model,--------- .

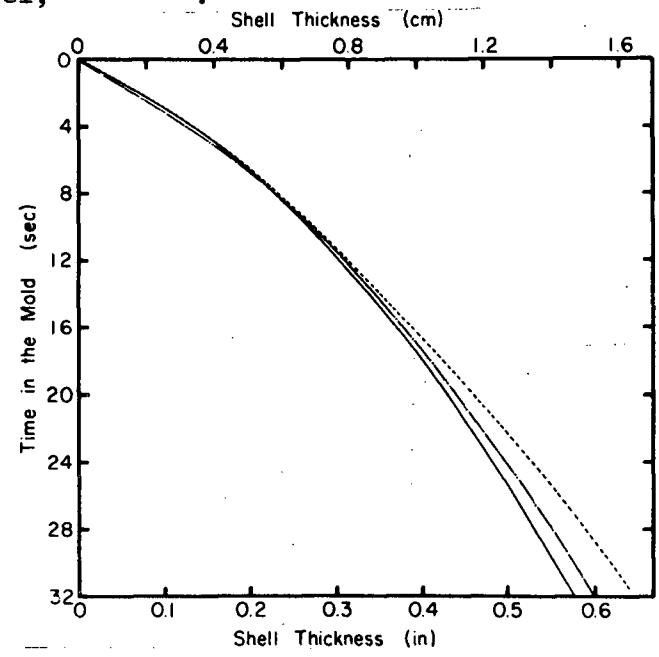

Figure 44. Effects of method of latent heat evolution and use of k_{eff} on calculated shell thickness for low carbon steel. k_{eff} used for T > 1525°C, 5-100% latent heat released at solidus, ═══; k_{eff} used for T > 1492°C, 100% latent heat released at soludus, —·—·—·—. Integral Profile model,– – – – – .

heat released per unit mass of steel at the solidus temperature. The results of varying the amounts of latent heat released at the solidus (γ_S) on the calculated pool profile in the mold is shown in Figure 43. From these calculations it was found that there was no difference in shell thickness if from 25 to 75% of the latent heat was released at the solidus. If all the latent heat was released at the solidus ($\gamma_S = 0$) a 1 to 2% increase in shell thickness was observed. This resulted in a decrease in the calculated pool depth of approximately 5%. Equation (7) has been used for the surface heat flux in calculating these profiles.

For the case of low carbon steels, as shown in Figure 44 there is no difference between the pool profile which has been calculated using the phase diagram to determine γ_S and that for which $\gamma_S = 0$. This is as expected since the freezing range in low carbon steels (.1%C) is small. For high carbon steels there should be an increase in the calculated shell thickness similar to that observed for the stainless steel. In Figure 44 the curves were calculated using equation (6) as the surface boundary condition in the mold.

Pool profiles have been calculated using the effective thermal conductivity (equation (5)) for both regions of the liquid pool where the temperature was greater than the liquidus temperature and for regions where the temperature was greater than the solidus temperature. These profiles are shown in Figures 43 and 44. When using k_{eff} through the solid-liquid region, the pool profiles are slightly thicker, approximately 6% for the stainless steel and 3% for the low carbon steel, then the previously calculated profiles. This procedure brings the pool profiles closer to those calculated using the integral profile model (also shown in

Figures 43 and 44). In the integral profile model conduction in the liquid is ignored and superheat is released at the same time as the latent heat, i.e., at the solidus. Thus, with the finite difference model the use of k_{eff} results in considerably more superheat being removed from the liquid in the mold region. This may explain why the finite difference shells are marginally thinner than the integral profile shells.

5.2.2. Calculated and Measured Pool Profiles in the Mold

5.2.2.1. Low Carbon Steel

In Tests M1, M2 (Figures 32(a) and (b)) and Aℓ1 to Aℓ3 (Figures 34(a) to (c)) there is excellent agreement between the measured profiles and the calculated profiles (curve B) using the finite difference model with equation (6) for the surface boundary condition. Using the finite difference model and equation (6), the shell thickness of low carbon steel in the mold can be expressed as a function of time giving

$$y_t = 0.118t^{0.75} \quad \text{(cm.,sec.)} \tag{13}$$

In Test Aℓ4 (Figure 34(d)) the agreement is good down to 0.32 m. below the meniscus beyond which the measured shell is appreciable thicker than B. However, the measured shell in the lower regions of the mold may be thicker than the actual shell, since the autoradiographs show the solid-liquid interface to be less distinct there than further up the mold. This is likely a consequence of inadequate mixing of the gold nearer the mold bottom.

It can be seen from the graphs that curves A (finite difference) and C (integral profile) calculated using equation (7) for the surface boundary condition agree closely for the mold; the same is true of curves B and D computed with equation (6).

From Table IX and Figure 3, it is apparent that the measured mold heat fluxes for Tests M1, M2 and Aℓ1 to Aℓ3 differ by less than 20% from the respective values predicted by equation (10). It is this difference that causes curve A, calculated using the measured heat flux, to differ to the extent observed from curve B, computed with the Savage and Pritchard heat flux. The largest difference between the measured and calculated heat fluxes is seen for Test Aℓ4. That the measured heat flux was low in this test may be due to inaccurate measurement of the mold water temperature rise.

In Tests M3, M4 (Figures 32)c) and (d)) and U1 (Figure 35) there is better agreement between the measured shell thickness and the shell thickness calculated using equation (7) (curve A) than equation (6) (curve B). This is as expected since in these tests the measured heat fluxes are greater than the predicted heat fluxes (Table IX). There is excellent agreement between the measured and predicted profiles in Test U1, but in Test M3 the difference between the two profiles is approximately 30%. From Figure 3 the measured heat flux for the 10.1 cm. billet (Test M3) appears to be reasonable reducing the possibility that the heat flux measurements were grossly incorrect. An

Table IX. Measured and Predicted Average Mold Heat Flux

Test No.	Average Mold Heat Flux (kcal $m.^{-2}$ $sec.^{-1}$)	
	Measured	Predicted
M1	358	405
M2	380	430
M3	510	437
M4	572	452
Aℓ1	335	320
Aℓ2	297	315
Aℓ3	308	323
Aℓ4	262	335
U1	575	415
At1	324	345

assumption that has been made in the model that may not apply in this case is that the shell thickness is uniform around the periphery of the mold. An examination of the autoradiograph of a transverse section from Test M4 (Figure 9(b), 10.1 cm. billet) reveals that in the mold, the centres of the faces of the billet are considerably thicker than the corners. If this is also true in Test M3, the measured shell thickness taken from the centre of the faces would be greater than the calculated value.

There is a possibility that errors have been made in the

measurement of the heat flow data, e.g. the mold water temperature rise of 4 to 8°C. However it does not seem that such errors are large since from Figure 3 the calculated heat fluxes for all of the tests can be seen to be within the average range of heat fluxes.

5.2.2.2. Stainless Steel Slab

In Figure 31 the measured and predicted pool profiles for the stainless steel slab are presented. From the graph it can be seen that the profiles calculated with the finite difference model for the two different surface boundary conditions are similar. This is understandable since the measured mold heat flux, used to calculate $\bar{h}_M$ in equation (7), is very similar to the time averaged, Savage and Pritchard heat flux relation, equation (10) (see Table IX and Figure 3). However, near the mold bottom, the calculated profile is 20 to 30% thinner than the measured profile. This difference is probably a result of the gold not outlining the true solid shell. In Figure 11, a longitudinal section from the slab, the shell can be seen to thicken in a discontinuous fashion at 15.7 cm. below the meniscus. A thin dark line indicating the presence of radioactive gold is observed apparently inside the solid shell for a short distance below the discontinuity. This suggests that there is little mixing in this area of the liquid pool. Similar observations of discontinuous thickening of the shell in the wide face of a slab when using radioactive tracers and immersed bifurcated shrouds have been reported by Zeder and Hedstrom[10].

For the stainless steel slab, the difference between the pool profiles calculated with the integral profile model and with the

finite difference model was less than 10%.

5.2.3. Calculated and Measured Pool Depths

5.2.3.1. Calculated Pool Depths using One-Dimensional Model

Figures 39(a) and (b) show the pool profiles calculated using the one-dimensional finite difference model in the web and flange areas of the beam blanks. The pool depths for Tests Aℓ1 and Aℓ2 are, in the web, 3.75 and 3.9 m., while in the flange, 7.3 and 7.1 m. respectively. The slight difference in pool depths between the two tests is mainly due to variations in spray heat transfer coefficients used in the model (Table III). In Test Aℓ1, the integral profile model was also used to predict the pool depth in the flange area, giving a depth about 30% less than the finite difference value. The difference in the calculated pool depths between the two models is a result of the constant thermal conductivity, used in the integral profile model (0.0071 kcal $m.^{-1}$ $sec.^{-1}$ $°C^{-1}$), being greater than the temperature dependent conductivity, used in the finite difference model, for temperatures under 1200°C. Thus, in the integral profile model the calculated surface temperature is higher (as seen in Figure 39(a)), resulting in a greater predicted rate of heat extraction from the steel according to equation (8) than in the finite difference model.

For the stainless steel slab (Figure 36), the one-dimensional finite difference model predicts a pool depth of 5.2 to 5.36 m., depending on the surface boundary condition employed in the mold. The horizontal bar in Figure 36 gives the position as well as the width of the tungsten pellet. A pool depth of 3.72 m. was calculated using the

integral profile model, also shown in Figure 36.

5.2.3.2. Calculated Pool Depths using Two-Dimensional Model.

The two-dimensional finite difference model was used to calculate pool profiles for the tests on billets and blooms. The pool profiles and the pellet positions for the four tests conducted at Manitoba Rolling Mills are presented in Figures 37(a) and (b). These profiles show how changing casting speed and billet size (10.1 cm. and 13.3 cm.) affects the calculated and measured pool depths.

The effect of changing casting speed on pool depth was also tested at Western Canada Steel (Test W1 and W2, Figure 40 and Table V). In tests conducted during the same cast, it was found that the calculated pool depth increased in Test W1 from 3.7 to 8.2 m. as the casting speed increased from 1.48 to 2.54 cm./sec., and in Test W2 from 4.0 to 7.4 m. with casting speed increase from 1.56 to 2.37 cm./sec. In Figure 40, the pool profile and pellet positions for Test W2a and W2c are presented.

Pool depths calculated for Tests Aℓ3 and Aℓ4 (Figure 39(c)) are 12.9 and 14.9 m. respectively. The larger pool depth for Test Aℓ4 is a result of the higher withdrawal rate and lower spray coefficients.

In Test U1, the pool depth of the 19 cm. billet, cast at 5.5 cm./sec., was calculated to be 32.3 m. Although the calculated depth seems exceptionally long, it is thought to be reasonable since at the plant bulging of the strand has been reported 30. m. below the mold.

5.2.3.3. Comparison of Calculated and Measured Pool Depths

From Figures 36 to 40 and Table V it can be seen that in all tests except Test Aℓ3, the calculated pool depths are much greater than the pool depths obtained using the pellet. There are several possible reasons for the discrepancy between the pool depths. In strands cast using low-head curved mold machines, it is likely that the pellet did not fall freely through the liquid steel, but intercepted the outside radius interface shortly after entry into the pool. Then the pellet could roll down the interface until it became lodged against the shell or contacted solid debris in the pool. For example, in Test Aℓ3, the tungsten pellet was found displaced toward the outside radius surface of the casting, as shown in Figure 39(c). The final pellet position was in fairly good agreement with the calculated shell thickness at this point. From the position of the pellet the pool depth was estimated (Figure 39(c)) to be 1060 cm., using a linear extrapolation of the pellet position and correcting for falling time. Since a linear extrapolation of the pellet position would give a minimum pool depth, it is highly probable that the actual pool depth is below this point and the pool depth calculated by the model is reasonable.

For Tests W1 and W2 where a straight mold, vertical type casting machine was used, the pellet should fall freely through the liquid pool (estimated falling velocity of the pellet is 70 cm./sec.), stopping only when it contacted solid debris at the pool bottom. From the results shown in Table V and Figure 40 the calculated pool depth is about twice the pool depth measured with the pellet. Therefore, for vertical castings the final pellet position must indicate the point in the casting where loosely packed dendritic debris or bridging has stopped the descent

of the pellet. Recently, evidence supporting this statement has been obtained from tests on a vertical casting (17.5 cm. billet) at Laclede Steel[40]. In these tests, radioactive gold contained in the tungsten pellet was released after the pellet had fallen to the "pool bottom". The gold was drawn down in the casting by fluid flow due to solidification shrinkage. The pellet was found near the centreline of the casting and the effective width of the liquid pool, outlined by the gold, at the pellet position can be seen in a transverse section autoradiograph, Figure 45, taken after the test. This shows that the effective pool width is greater than the width of the pellet and liquid metal is present far below the final pellet position. Therefore, the calculated pool depth which indicates the point at which the last liquid metal has solidified may be reasonable.

5.2.4. Calculated and Measured Surface Temperatures

From Figures 31 to 35 it is obvious that the choice of either equation (6) or (7) to describe the surface heat flux has a significant effect on the surface temperature in the mold region. For the case of a constant heat transfer coefficient (equation (7) curve A) the temperature decreases uniformly while use of the assumed heat flux (equation (6) curve B) results in a slight reheating of the surface. Despite the difference between the two temperature profiles at the bottom of the mold, the temperatures are identical by the end of the zone 1 sprays. Similar findings have been reported by Kung and Pollock[21].

The surface temperatures predicted by the finite difference and integral profile models (Figures 31 and 32(b)) when using the same

Figure 45. Autoradiograph of transverse section near tungsten pellet position taken after tests on a 17.5 cm. billet at Laclede Steel.

surface boundary condition in the mold agree to within 4%.

The surface temperatures at the mold bottom, calculated using the Savage and Pritchard surface boundary condition (equation (6)), are thought to be reasonable. This is based on a comparison of calculated surface temperatures to values measured by Gautier et al.[6] at the mold exit. These workers measured the surface temperature of steel billets at the mold bottom by using light pipes positioned at the billet face to channel light to a two color pyrometer. They found through laboratory trials that the accuracy of this system was about ± 30°C. The measured and predicted surface temperatures (using equation (6)) are presented in Table X.

The surface temperature calculated with the finite difference model are within 2 to 5% of the measured values, with one exception. With the integral profile model the calculated temperatures are within 2 to 8% of the measured values.

The calculated surface temperatures in the sub-mold regions (shown in Figures 36 to 40) are only approximate because of the lack of adequate data to properly calculate the spray heat transfer coefficients. However these temperatures also appear to be reasonable since, for example, with Test At1 (Figure 36) the calculated surface temperature of 600 to 700°C was very low; in agreement with this, the surface of the slab emerging from the casting machine was observed to be too cool to radiate noticeable light. In Table V surface temperature measurements taken at the straightener with an optical pyrometer for Tests M1 to M3 and Aℓ2 to Aℓ4 are listed. For Tests Aℓ3 and Aℓ4, as seen in Figure 39(c),

Table X. Predicted and Measured[6] Surface Temperatures (°C)

Cast No.	Dwell Time (sec.)	Measured	Calculated Finite Difference	Calculated Integral Profile
8.5 x 8.5 cm				
42771	13.3	1237	1170	1188
13440	12.8	1234	1174	1190
13401	11.0	1228	1193	1200
13402	12.8	1210	1174	1190
10.5 x 10.5 cm				
13855	19.7	1084	1136	1176
13756	15.5	1099	1154	1180
13757	18.6	1091	1140	1176
13761	18.6	1093	1140	1176
13762	19.7	1089	1136	1176
13763	19.7	1089	1136	1176
12.0 x 12.0 cm				
42803	21.7	1100	1132	1178
13427	24.1	1106	1129	1184
13428	20.2	1054	1135	1177

the calculated surface temperatures at the straightener are reasonable. For Tests M1 to M3 the calculated surface temperatures at the straightener was usually higher than the measured. In Figure 40, Tests W2a and W2c, it is interesting to note the decrease in surface temperature that occurs when the casting speed is lowered and the spray pressures are not adjusted accordingly. The increased cooling of the strand may result in internal cracking.

SUMMARY

1. In the liquid pool, the fluid flow pattern is complex. Extensive mixing occurs in the mold region, due to the momentum of the input stream; little mixing occurs in the lower regions of the liquid pool. The depth of penetration of the input stream is greater for open pouring than for pouring through an immersed shroud, and correspondingly mixing in the pool extends to a much lower level for open pouring. The input stream mixes equally above and below the point of entry with immersed shrouds. Some solute banding can occur in the liquid pool.

2. In the present tests the solid-liquid interface was clearly delineated in the upper mold region, and in some tests in the lower mold and sub-mold regions as well. In general, the shell is uniform in thickness around the mold. No major difference in shell uniformity was noted using either oil lubricant or slag powder lubricant. Tearing of the shell at the meniscus, surface ripple marks, and small fluctuations in shell thickness were observed, which are related to mold oscillation, lubricating practise and condition of mold surface.

3. The flanges of the beam blanks (Tests Aℓ1 and Aℓ2) were reshaped by the support rollers when partially solidified, resulting in distortion of the solidifying front. Distortion of the shell was also observed due to misaligned web support rollers.

4. Misalignment of the submerged shroud in Test Aℓ4 had no observable effect on the thickness of the solid shell in the mold.

5. Thinning of the solid shell at the corners of the strand was observed in some cases. In Test Aℓ4, a corner crack, filled with material enriched in gold and sulphur, was observed in the bloom corner. The re-entrant corners are associated with poor thermal contact between the strand and the mold as a result of solidification shrinkage and subsequent bowing out of the central part of the strand face due to the ferrostatic pressure.

6. The cast structure of the open poured strands was columnar adjacent to the outside surface and coarse equiaxed dendritic in the centre. For strands cast using a curved mold the as-cast centreline of the strand was displaced toward the outer radius surface. The equiaxed grains are considered to result from the remelting of dendrite arms due to the input stream near the bottom of the mold, the dendrite segments falling to the lower regions of the liquid pool. The collection of dendritic debris at the pool bottom may result in the periodic bridging and centreline porosity observed in some tests.

The cast structure of the bloom using an immersed nozzle (Test Aℓ4) consisted primarily of cored, dendritic, equiaxed grains with little evidence of a columnar structure. In this bloom and in the equiaxed zone in Test U1, marked solute rich pipes, aligned in V formation, were observed. The pipes are attributed to downward flow of residual solute rich liquid resulting from solidification shrinkage, along "fault paths" in the dendritic debris.

7. The primary dendrite spacing in continuously cast steel was larger than that observed in high strength steel cast directionally against a copper chill.

8. No macrosegregation was observed to be present in the stainless steel slab at the centreline, where columnar grains from each of the large slab faces met.

9. Radial interdendritic cracking was observed in strands with a low to intermediate Mn/S ratio. All the cracks were filled with solute rich material.

10. Intergranular centreline cracking occurred extensively down the centre of the web in the E beam blank, and to a lesser extent in the centre of one bloom (Test A&4). The cracks are mostly filled with solute rich material. They are attributed to overcooling of the strand in the sprays.

11. In strands cast using a curved mold the distribution of sulphide inclusions appears to be related to the Mn/S ratio of the steel. With a low ratio, clumps of sulphide inclusions are found in a band near the inside radius surface of the strand. The clumps of inclusions clearly form in the solid-liquid region and float up to the advancing inner radius solidifying front where they are trapped. With a high Mn/S ratio, the clumps of inclusions are more uniformly dispersed throughout the casting.

12. There is excellent agreement between the observed pool profiles in the mold and the profiles calculated, using the Savage and Pritchard equation for the heat flux between the strand and the mold.

13. The calculated surface temperature of low carbon billets at the bottom of the mold agreed to within 2 to 5% of measured values reported in the literature.

14. The pool and surface temperature profiles in the mold, calculated using the finite difference model, have been found to agree closely with profiles calculated with an integral profile model.

15. The calculated values of the pool depth based on a heat transfer analysis of the strand along the entire liquid pool are thought to be reasonable. This is supported by the good agreement between the estimated pool depth in Test Aℓ3, determined with the tungsten pellet, and the calculated value.

16. Recent evidence indicates that in most of the tests the tungsten pellet, used to estimate the pool depth, was obstructed from reaching the pool bottom by solid debris. This accounts for the difference between the measured and calculated pool depths.

CONCLUSIONS

The results of the present investigation clearly demonstrate that important information can be obtained concerning the operating characteristics of continuously cast billets, blooms, beam blanks and slabs, using radioactive tracer techniques. Observations of the thickness and uniformity of the solid shell in the casting (a) can be related to the lubricating practice by the incidence of tearing at the meniscus, and fluctuations in shell thickness, (b) can indicate a tendency for corner cracking associated with thin corners, (c) demonstrate distortions of the casting due to non-uniform cooling, normally not observable due to reshaping of the steel in the spray cages or withdrawal rolls, (d) relate radial cracking to shell distortions and determine when the cracking occurs.

The cast structure of the steel is normally resolved in the autoradiographs and can be examined to determine (a) the size and distribution of equiaxed grains, (b) the presence of corner, radial and centreline cracks filled with residual liquid during final solidification, (c) the distribution of clumps of inclusions in the steel, distinguishing those which formed in situ from those which moved through the liquid pool to their final positions, (d) the relationship of solute rich pipes and the cast structure. The extent of fluid flow in the liquid pool can be established, particularly as it relates to pouring with an open stream or using immersed nozzles.

The heat flow analysis, by coupling calculations with direct observations and measurements, establishes that the boundary conditions

adopted in the calculations do apply to the real continuous casting situation. Pool depths and surface temperatures can be realistically calculated and the effect of changing casting conditions or mold design can be predicted with reasonable confidence.

SUGGESTED FUTURE WORK

1. It is recommended that further tracer experiments be conducted to:

   a) establish the fluid flow pattern in the liquid pool by varying the position and time of tracer addition.

   b) determine the relationship between mold corner radius and corner cracking by examining the effect of radius on local shell thickness.

   c) investigate the effects of tundish teeming practice and pouring temperature on the cast structure.

2. Temperature measurements in the mold should be made to determine directly the heat flux from the casting to the mold cooling water as a function of distance both below the meniscus and around the mold perimeter.

3. The relationship between internal cracking and stress concentrations in the billet due to improper cooling conditions should be investigated using a simple stress analysis and the temperature distribution in the solid shell determined from the heat flow analysis.

4. Measurements of the surface temperature of the strand in the sub-mold regions should be made to check the temperatures predicted by the mathematical models.

5. The spray heat transfer coefficients should be determined as a function of spray water droplet size, momentum, impingement angle and flux. Also the effect of rollers in the spray chamber on the heat transfer coefficient should be evaluated.

APPENDIX

Derivation of Formulae for the Finite Difference Models

In the finite difference formulation of equation (3), a thin horizontal slice of the section being cast was subdivided into a number of equally spaced elements with nodal points being located at their centres (Figure 46). The node corresponding to the centre line of the casting was designated as 1 and successive nodes as 2, 3, 4, etc., with the surface node being designated as n. Each nodal point for nodes 1 through (n-1) represents a volume of metal of unit area and width, Δy, the width of the n th node being $\Delta y/2$.

In order to solve the unsteady one dimensional conduction equation (3) an explicit method of finite differences was used. This method involves calculation of the total enthalpy of a node at time $t + \Delta t$, (H') from the known node enthalpies calculated at time t, (H).

The total enthalpy of a node for nodes 2 through (n-1) was calculated by substituting into equation (3) first-order forward and central difference approximations for the time and distance partial derivatives. Then, solving for H_i', equation (14) was obtained.

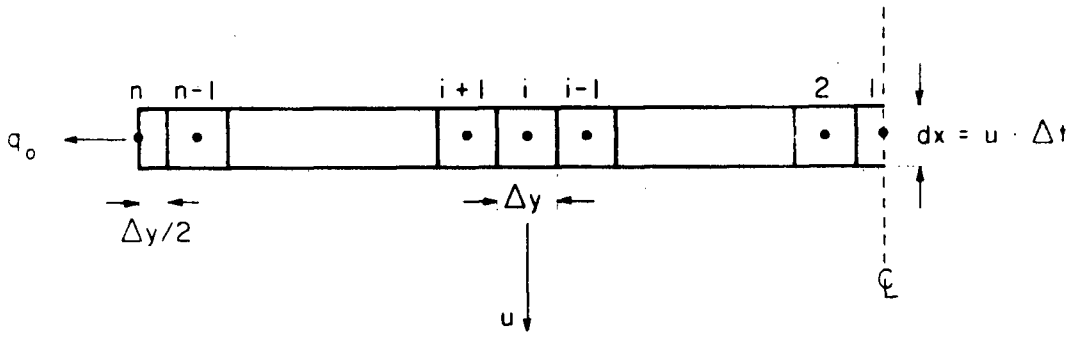

Figure 46. Arrangement of nodes in horizontal slice for one-dimensional finite difference model.

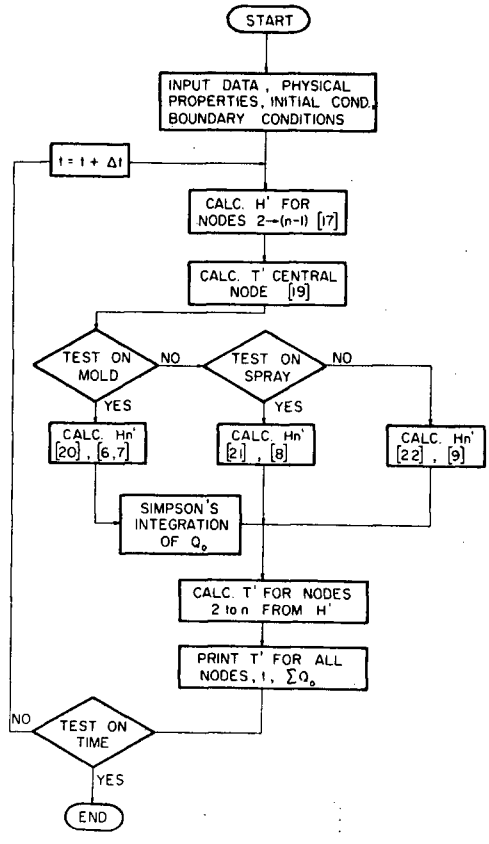

Figure 47. Flow chart of computer program for finite difference model.

$$H_i' = H_i + \frac{\Delta t}{\rho(\Delta y)^2}\left[(a + bT_i)(T_{i+1} - 2T_i + T_{i-1}) + \right.$$

$$\left.\frac{b}{4}\left(T_{i+1}^2 - 2T_{i+1} \cdot T_{i-1} + T_{i-1}^2\right)\right] \qquad (14)$$

The temperature of the center node was calculated by writing a second-order forward difference approximation for the centreline boundary condition.

$$t \geq 0 \quad y = 0 \quad -k\frac{\partial T}{\partial y} = 0 \qquad (15)$$

Solving for T_1' then gives

$$T_1' = \frac{4}{3} T_2' - \frac{1}{3} T_3' \qquad (16)$$

The surface temperature was computed from a heat balance on node n

$$-k\frac{\partial T}{\partial y} - q_o = \frac{\Delta y}{2} \rho \frac{\partial H}{\partial t} \qquad (17)$$

Using a first-order forward and backward finite difference expansion for the time and distance partial derivatives, equation (17) can be rewritten as

$$H_n' = H_n + \frac{2\Delta t}{\rho(\Delta y)^2}\left[(a + b\,T_n)(T_{n-1} - T_n) - \Delta y \cdot q_o\right] \qquad (18)$$

Having calculated the enthalpy of a given node at time $t + \Delta t$, the

temperature was then computed using the enthalpy-temperature relationships presented in Figure 2.

The distance between nodes, Δy, was first taken to be 1/20 of the half width of the casting. Using this value of Δy, the time interval between iterations, Δt, was determined from the stability criterion (equation (19)).

$$\frac{k}{\rho C} \frac{\Delta t}{(\Delta y)^2} < 1/6 \qquad (19)$$

The values of both Δy and Δt were varied in subsequent computer runs and it was found that the temperature field was not appreciably affected.

A flowchart of the computer program is given in Figure 47.

In the finite difference formulation of equation (2), the nodal arrangement used in the transverse quarter section of the casting is shown in Figure 48. In order to simplify the computation, it was assumed that the blooms and billets were square so that nodes in the y and z directions are equal in size.

This assumption was true in all cases except on the blooms at Algoma Steel (22.9 x 26.7 $cm.^2$). In this case the dimensions of the blooms were taken to be 24.8 x 24.8 $cm.^2$.

The method of solution of the two-dimensional conduction equation is similar to the one-dimensional case. By solving equation (2) to determine the total enthalpy at time $t + \Delta t$ for the central nodes, H'_{ij}, equation (20) was obtained.

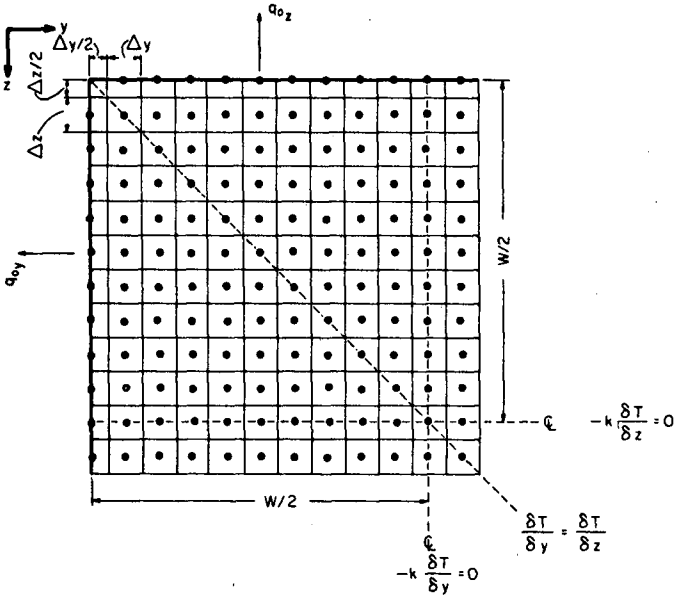

Figure 48. Arrangement of nodes in horizontal section of billet for two-dimensional finite difference model.

$$H'_{i,j} = H_{i,j} + \frac{\Delta t}{\rho(\Delta y)^2}\left[(a + bT_{i,j})(T_{i,j+1} - 2T_{i,j} + T_{i,j-1}) + \frac{B}{4}\left(T_{i,j+1}^2 - 2T_{i,j+1} \cdot T_{i,j-1} + T_{i,j-1}^2\right)\right] + \frac{\Delta t}{\rho(\Delta z)^2}\left[(a + bT_{i,j})(T_{i+1,j} - 2T_{i,j} + T_{i-1,j}) + \frac{B}{4}\left(T_{i+1,j}^2 - 2T_{i+1,j} \cdot T_{i-1,j} + T_{i-1,j}^2\right)\right] \quad (20)$$

Determining the enthalpy at time t + Δt for the surface nodes, (i,n) at y = 0, from the heat balance on the node, gives

$$H'_{i,n} = H_{i,n} + \frac{2\Delta t}{\rho(\Delta y)^2}\left[(a + bT_{i,n})(T_{i,n-1} - T_{i,n}) - \Delta y \cdot q_{o_y}\right] \quad (21)$$

and for the surface nodes, (n,j) at z = 0, gives

$$H'_{n,j} = H_{n,j} + \frac{2\Delta t}{\rho(\Delta z)^2}\left[(a + bT_{n,j})(T_{n-1,j} - T_{n,j}) - \Delta z \cdot q_{o_z}\right] \quad (22)$$

Since it is assumed that Δy = Δz, the temperature distribution in the cross section should be symmetric about the diagonal. Therefore, the heat flux from only one face need be considered.

The same stability criterion was used in this solution as in the one-dimensional case.

REFERENCES

1. Szekely, J. and Stanek, V., Met. Trans., Vol.1, 1970, pp.119-126.

2. Mills, N.T. and Barnhardt, L.F., J. Metals, Vol.23, 1971, pp.37-43.

3. Szekely, J. and Yadoya, R.T., Met. Trans., Vol.3, 1972, pp.2673-2680.

4. Varga, C. and Fodor, J., Proceedings of the Second International Conference on the Peaceful Uses of Atomic Energy, United Nations, 1959, pp.235-236.

5. Arnoult, J., Kohn, A. and Plumensi, J.P., Revue de Metallurgie, Vol.66, pp.585.

6. Gautier, J.J., Morillon, V. and Dumont-Fillon, J., J. Iron Steel Inst., Vol.208, pp.1053-1059.

7. Morton, S.K. and Weinberg, F., J. Iron Steel Inst., Vol.211, 1973.

8. Gomer, C.R. and Andrews, K.W., J. Iron Steel Inst., Vol.207, 1969, pp.26-35.

9. Nagaoka, N., Inamoto, K. and Nemoto, H., Trans. ISIJ, Vol.12, 1972, pp.317-319.

10. Zeder, V.H. and Hedstrom, J., Radex-Rundschau, Vol.2, 1971, pp.407-417.

11. Mori, H., Tanaka, N., Sato, N. and Hirai, M., Trans. ISIJ, Vol.12, 1972, pp.102-111.

12. Ushijima, K., Continuous Casting of Steel, Iron and Steel Inst. Special Report 89, 1965, pp.59-71.

13. Adams, C.J., Proc. Nat. Open Hearth Basic Oxygen Steel Conf., Vol.54, pp.290-302.

14. Lankford, W.T. Jr., Met. Trans., Vol.3, 1972, pp.1331-1357.

15. Pehlke, R.D., ASM Met. Eng. Quart., Vol.4, 1964, pp.42-47.

16. Hills, A.W.D., J. Iron Steel Inst., Vol.203, 1965, pp.18-26.

17. Donaldson, J.W. and Hess, M., in Continuous Processing and Process Control, ed., T.R. Ingraham, Met. Soc. AIME Conf., Vol.49, 1966, pp.299-319.

18. Mizikar, E.A., Trans. Met. Soc. AIME, Vol.239, 1967, pp.1747-1753.

19. Hills, A.W.D., Trans. Met. Soc. AIME, Vol.245, 1969, pp.1471-1479.

20. Fahidy, T.Z., J. Iron Steel Inst., Vol.207, 1969, pp.1373-1376.

21. Kung, E.Y. and Pollock, J.C., in Instrumentation for the Iron and Steel Industry, ISA Proceedings, Vol.17, 1967, pp.8-1 - 8-2.

22. Savage, J., J. Iron Steel Inst., Vol.200, 1962, pp.41-47.

23. Savage, J. and Pritchard, W.H., J. Iron Steel Inst., Vol.178, 1954, pp.267-277.

24. Krainer, H. and Tarmann, B., Stahl Eisen, Vol.69, 1949, pp.813-819.

25. Brimacombe, J.K. and Weinberg, F., J. Iron Steel Inst., Vol.211, 1973.

26. Mizikar, E.A., Iron Steel Eng., Vol.47, No.6, 1970, pp.53-60.

27. BISRA, Physical Constants of Some Commercial Steels at Elevated Temperatures, 1952, Butterworths, London.

28. Brimacombe, J.K., Lait, J.E. and Weinberg, F., Proceedings - Mathematical Process Models in Iron and Steelmaking, Amsterdam, February, 1973.

29. Andrew, D.J., Open Hearth Proceedings, 1969, pp.143-148.

30. Hester, K.D., Mulligan, E.H., Rohatynski, E. and Woodhouse, G.H., Can. Met. Quart., Vol.7(2), 1968, pp.97-107.

31. Wagstaff, R.S., Stock, G.E. and Layne, G.N., Iron Steel Eng., Vol.43, 1966, pp.71-76.

32. Muttitt, F.C., Iron Steel Eng., Vol.46, No.1, 1969, pp.83-91.

33. Lucenti, G.S., Iron Steel Eng., Vol.46, No.7, 1969, pp.83-100.

34. Vandrunen, G., The Univ. of Brit, Col., private communication (1973).

35. Gomer, C.R. and Andrews, K.W., The Solidification of Metals ISI, P.110, 1968, pp.363-369.

36. Kohn, A., Discussion Four, The Solidification of Metals ISI, P.110, 1968, p.416.

37. Dickens, R., The Univ. of Brit. Col., private communication (1972).

38. Weinberg, F. and Buhr, R.K., The Solidification of Metals ISI, P.110, 1968, pp.295-304.

39. Sims, C.E. and Forgeng, W.D., Electric Furnace Steelmaking, Vol.2, Sims, C.E., ed., pp.373, Interscience Publishers, New York, 1967.

40. Weinberg, F. and Vandrunen, G., The Univ. of Brit. Col., private communication (1973).

PUBLICATIONS

J.K. Brimacombe, J.E. Lait and F. Weinberg, The Application of Mathematical Models to Predict Pool Profiles in Continuously Cast Steel, Paper presented to the Second ISI Conference on Mathematical Process Models Applied in Iron and Steelmaking, Amsterdam, Netherlands, 19-21, February, 1973, to be published by the ISI.

J.E. Lait, J.K. Brimacombe, and F. Weinberg, Pool Profile, Liquid Mixing and Cast Structure in Steel, Continuously Cast in Curved Molds, Paper to be presented and published at the Conference on Continuous Casting, February, 1973, AIME Annual Meeting, Chicago, Illinois.

J.K. Brimacombe, J.E. Lait, and F. Weinberg, A Comparison of Calculated and Observed Liquid Pool Profiles and Pool Depths in Continuous Casting of Steel, Paper to be presented and published at the Conference on Continuous Casting, February, 1973, AIME Annual Meeting, Chicago, Illinois.

J.E. Lait, J.K. Brimacombe, F. Weinberg, and F.C. Muttitt, The Liquid Pool Geometry and Cast Structure in Continuously Cast Blooms and Beam Blanks at the Algoma Steel Corporation, Paper to be presented at the National Open Hearth and Basic Oxygen Steel Conference, AIME, April, 1973, Cleveland, Ohio.